

Nanomaterials for Biomedical Applications and Environmental Monitoring

Guest Editors: Anh-Tuan Le, Tran Quang Huy, Manh-Huong Phan,
Nguyen Van Hieu, and Tran Trong An





Nanomaterials for Biomedical Applications and Environmental Monitoring

Journal of Nanomaterials

Nanomaterials for Biomedical Applications and Environmental Monitoring

Guest Editors: Anh-Tuan Le, Tran Quang Huy,
Manh-Huong Phan, Nguyen Van Hieu, and Tran Trong An



Copyright © 2015 Hindawi Publishing Corporation. All rights reserved.

This is a special issue published in "Journal of Nanomaterials." All articles are open access articles distributed under the Creative Commons Attribution License, which permits unrestricted use, distribution, and reproduction in any medium, provided the original work is properly cited.

Editorial Board

Domenico Acierno, Italy
Katerina Aifantis, USA
Sheikh Akbar, USA
Nageh K. Allam, USA
Margarida Amaral, Portugal
Martin Andersson, Sweden
Raul Arenal, Spain
Ilaria Armentano, Italy
Vincenzo Baglio, Italy
Lavinia Balan, France
Thierry Baron, France
Andrew R. Barron, USA
Reza Bayati, USA
Hongbin Bei, USA
Daniel Bellet, France
Stefano Bellucci, Italy
Enrico Bergamaschi, Italy
Samuel Bernard, France
D. Bhattacharyya, New Zealand
Sergio Bietti, Italy
Giovanni Bongiovanni, Italy
Theodorian Borca-Tasciuc, USA
Mohamed Bououdina, Bahrain
Torsten Brezesinski, Germany
C. Jeffrey Brinker, USA
Christian Brosseau, France
Philippe Caroff, Australia
Victor M. Castaño, Mexico
Albano Cavaleiro, Portugal
Bhanu P. S. Chauhan, USA
Shafiq Chowdhury, USA
Jin-Ho Choy, Korea
K.-Leong Choy, United Kingdom
Yu-Lun Chueh, Taiwan
Elisabetta Comini, Italy
Giuseppe Compagnini, Italy
David Cornu, France
Miguel A. Correa-Duarte, Spain
P. Davide Cozzoli, Italy
Shadi A. Dayeh, USA
Luca Deseri, USA
Yong Ding, USA
Philippe Dubois, Belgium
Alain Dufresne, France
Zehra Durmus, Turkey

Joydeep Dutta, Oman
Ali Eftekhari, USA
Jeffrey Elam, USA
Samy El-Shall, USA
Ovidiu Ersen, France
Claude Estournès, France
Andrea Falqui, KSA
Matteo Ferroni, Italy
E. Johan Foster, USA
Ilaria Fratoddi, Italy
Wolfgang Fritzsche, Germany
Alan Fuchs, USA
Miguel A. Garcia, Spain
Siddhartha Ghosh, Singapore
P. K. Giri, India
Russell E. Gorga, USA
Jihua Gou, USA
Jean M. Greneche, France
Smrati Gupta, Germany
Kimberly Hamad-Schifferli, USA
Simo-Pekka Hannula, Finland
Michael Harris, USA
Yasuhiko Hayashi, Japan
F. Hernandez-Ramirez, Spain
Michael Z. Hu, USA
Nay Ming Huang, Malaysia
Shaoming Huang, China
David Hui, USA
Zafar Iqbal, USA
Balachandran Jeyadevan, Japan
Xin Jiang, Germany
Rakesh Joshi, Australia
Jeong-won Kang, Korea
Hassan Karimi-Maleh, Iran
A. Kelarakis, United Kingdom
Alireza Khataee, Iran
Ali Khorsand Zak, Iran
Philippe Knauth, France
Ralph Krupke, Germany
Christian Kübel, Germany
Prashant Kumar, United Kingdom
Michele Laus, Italy
Eric Le Bourhis, France
Burtrand Lee, USA
Jun Li, Singapore

Meiyong Liao, Japan
Shijun Liao, China
Silvia Licocchia, Italy
Wei Lin, USA
Jun Liu, USA
Zainovia Lockman, Malaysia
Nico Lovergine, Italy
Jim Low, Australia
Jue Lu, USA
Songwei Lu, USA
Ed Ma, USA
Laura M. Maestro, Spain
Gaurav Mago, USA
Muhamamd A. Malik, United Kingdom
Devanesan Mangalaraj, India
Sanjay R. Mathur, Germany
Tony McNally, United Kingdom
Yogendra Mishra, Germany
Paulo Cesar Morais, Brazil
Paul Munroe, Australia
Jae-Min Myoung, Korea
Rajesh R. Naik, USA
Albert Nasibulin, Russia
Toshiaki Natsuki, Japan
Koichi Niihara, Japan
Natalia Noginova, USA
Sherine Obare, USA
Won-Chun Oh, Republic of Korea
Atsuto Okamoto, Japan
Abdelwahab Omri, Canada
Ungyu Paik, Republic of Korea
Piersandro Pallavicini, Italy
Edward A. Payzant, USA
Alessandro Pegoretti, Italy
Ton Peijs, United Kingdom
Oscar Perales-Pérez, Puerto Rico
Jorge Pérez-Juste, Spain
Alexey P. Popov, Finland
Philip D. Rack, USA
Peter Reiss, France
Orlando Rojas, USA
Marco Rossi, Italy
Ilker S. Bayer, Italy
Cengiz S. Ozkan, USA
Sudipta Seal, USA

Shu Seki, Japan
Vladimir Šepelák, Germany
Huaiyu Shao, Japan
Prashant Sharma, USA
Donglu Shi, USA
Bhanu P. Singh, India
Surinder Singh, USA
Vladimir Sivakov, Germany
Ashok Sood, USA
Adolfo Speghini, Italy
Marinella Striccoli, Italy
Xuping Sun, KSA
Ashok K. Sundramoorthy, USA
Angelo Taglietti, Italy

Bo Tan, Canada
Leander Tapfer, Italy
Valeri P. Tolstoy, Russia
Muhammet S. Toprak, Sweden
Ramon Torrecillas, Spain
Takuya Tsuzuki, Australia
Tamer Uyar, Turkey
B. Vaidhyanathan, United Kingdom
Luca Valentini, Italy
Rajender S. Varma, USA
Ester Vazquez, Spain
Antonio Villaverde, Spain
Ajayan Vinu, Australia
Ruibing Wang, Macau

Shiren Wang, USA
Yong Wang, USA
Magnus Willander, Sweden
Ping Xiao, United Kingdom
Zhi Li Xiao, USA
Yangchuan Xing, USA
Doron Yadlovker, Israel
Yoke K. Yap, USA
Kui Yu, Canada
William W. Yu, USA
Michele Zappalorto, Italy
Renyun Zhang, Sweden

Contents

Nanomaterials for Biomedical Applications and Environmental Monitoring, Anh-Tuan Le, Tran Quang Huy, Manh-Huong Phan, Nguyen Van Hieu, and Tran Trong An
Volume 2015, Article ID 283286, 2 pages

TLC-SERS Plates with a Built-In SERS Layer Consisting of Cap-Shaped Noble Metal Nanoparticles Intended for Environmental Monitoring and Food Safety Assurance, H. Takei, J. Saito, K. Kato, H. Vieker, A. Beyer, and A. Götzhäuser
Volume 2015, Article ID 316189, 9 pages

Controlled Synthesis of Hierarchically Assembled Porous ZnO Microspheres with Enhanced Gas-Sensing Properties, Shengsheng You, Haojie Song, Jing Qian, Ya-li Sun, and Xiao-hua Jia
Volume 2015, Article ID 680306, 9 pages

Rapid and Sensitive Detection of Lung Cancer Biomarker Using Nanoporous Biosensor Based on Localized Surface Plasmon Resonance Coupled with Interferometry, Jae-Sung Lee, Sae-Wan Kim, Eun-Yoon Jang, Byoung-Ho Kang, Sang-Won Lee, Gopalan Sai-Anand, Seung-Ha Lee, Dae-Hyuk Kwon, and Shin-Won Kang
Volume 2015, Article ID 183438, 11 pages

Preparation of Mixed Semiconductors for Methyl Orange Degradation, Sangeeta Adhikari and Debasish Sarkar
Volume 2015, Article ID 269019, 8 pages

Preparation and Evaluation of Pralidoxime-Loaded PLGA Nanoparticles as Potential Carriers of the Drug across the Blood Brain Barrier, Washington Chigumira, Prosper Maposa, Louis L. Gadaga, Admire Dube, Dexter Tagwireyi, and Charles C. Maponga
Volume 2015, Article ID 692672, 5 pages

Gold Nanoparticles Increase PLK1-Specific Small Interfering RNA Transfection and Induce Apoptosis of Drug Resistance Breast Cancer Cells, Ying Tian, Yunlei Zhang, Jing Pan, Nan Lu, Shouju Wang, and Guangming Lu
Volume 2015, Article ID 720198, 9 pages

Remineralizing Efficacy of Fluorohydroxyapatite Gel on Artificial Dentinal Caries Lesion, Qianqian Wang, Shize Liu, Xuejun Gao, Yan Wei, Xuliang Deng, Haifeng Chen, and Xuehui Zhang
Volume 2015, Article ID 380326, 9 pages

The Application of Carbon Nanotubes in Magnetic Fluid Hyperthermia, Grzegorz Raniszewski, Arkadiusz Miaskowski, and Slawomir Wiak
Volume 2015, Article ID 527652, 8 pages

Editorial

Nanomaterials for Biomedical Applications and Environmental Monitoring

**Anh-Tuan Le,¹ Tran Quang Huy,² Manh-Huong Phan,³
Nguyen Van Hieu,⁴ and Tran Trong An⁵**

¹Department of Nanoscience and Nanotechnology, Hanoi University of Science and Technology, Hanoi 10000, Vietnam

²National Institute of Hygiene and Epidemiology (NIHE), Hanoi 10000, Vietnam

³Department of Physics, University of South Florida, Tampa, FL 33620, USA

⁴International Training Institute for Materials Science, Hanoi University of Science and Technology, Hanoi 10000, Vietnam

⁵Delft Institute of Microsystems and Nanoelectronics (DIMES), Delft University of Technology, 2600 AA Delft, Netherlands

Correspondence should be addressed to Anh-Tuan Le; tuan.leanh1@hust.edu.vn

Received 3 September 2015; Accepted 6 September 2015

Copyright © 2015 Anh-Tuan Le et al. This is an open access article distributed under the Creative Commons Attribution License, which permits unrestricted use, distribution, and reproduction in any medium, provided the original work is properly cited.

In recent years, outbreak of emerging diseases and environmental pollution has been a significant threat on global economies and public health. Nanomaterials have high potential to address these challenges due to their advantages such as large surface area, outstanding properties, and high flexibility. In this special issue, several excellent research results on advanced nanomaterials for biomedical applications and environmental monitoring were reported.

As first challenge for biomedical applications, J.-S. Lee et al. developed a nanobiosensor to detect a lung cancer-specific biomarker. The nanobiosensor is based on an anodic aluminum oxide (AAO) chip and functions on the principles of localized surface plasmon resonance (LSPR) and interferometry. The sensor chip is sensitive to the refractive index (RI) changes of the surrounding medium and also provides simple and label-free detection when specific antibodies are immobilized on the gold-deposited surface of the AAO chip. The limit of detection (LOD) was found to be 100 ag/mL and the biosensor had high sensitivity over a wide concentration range. Q. Wang et al. evaluated the remineralizing efficacy of fluorohydroxyapatite (FHA) gel on artificial dentinal caries lesion *in vitro*. It was found that the FHA gel could rapidly construct apatite on the artificial dentinal caries surface and significantly increase the mineral density, which suggested that FHA gel might be a proper IPT material with remineralizing function. G. Ransiszewski et al. reported the

results of the investigation into the applications of carbon nanotubes with ferromagnetic nanoparticles as nanoheaters for targeted thermal ablation of cancer cells. Application of carbon nanotubes with ferromagnetic properties can be used in a radio frequency thermal ablation. RF ablation therapy brings the lowest risk compared to the other techniques (e.g., surgery and chemotherapy) of tumor therapy. This method offers faster and more targeted treatment for liver cancer with fewer side effects. W. Chigumira et al. presented preparation and evaluation of pralidoxime-loaded PLGA nanoparticles as potential carriers of the drug across the blood brain barrier. Y. Tian et al. reported the use of gold nanoparticles to increase PLK1-specific small interfering RNA transfection and induce apoptosis of drug-resistant breast cancer cells. The transfection of PLK1-specific siRNA into cells not only silenced its targeting genes but also induced apoptosis of the drug-resistant breast cancer cells. It was worth noting that exclusive gold nanoparticles (GNPs) had no toxic effect on normal/cancer cells. Importantly, the GNPs could be visualized by X-ray imaging in a concentration dependent manner because of the excellent properties of gold. Overall, this work disclosed the great potential of GNPs as the excellent delivery system in gene therapy for drug-resistant cancers and the further application of X-ray imaging.

As second challenge for environmental monitoring, S. Adhikari and D. Sarkar synthesized a mixed semiconductor

of ZnO combined with WO_3 . An optimum amount of 10 wt.% nanocuboid WO_3 addition to quasi-fibrous ZnO is an effective choice for methyl orange dye degradation compared to commercial ZnO nanoparticles. The prepared mixed oxide nanocomposite of WO_3 and ZnO is found as an effective photocatalyst for degradation of organic pollutants in water. Takei et al. reported on a thin layer chromatograph (TLC) with a built-in surface enhanced Raman scattering (SERS) layer for in situ identification of chemical species separated by TLC. The TLC-SERS plates with a built-in SERS layer consisting of cap-shaped noble metal nanoparticles could be used for environmental monitoring and food safety assurance. The authors prepared their TLC-SERS plate with the following procedure: (1) adsorption of 100 nm in diameter SiO_2 nanospheres as a dense monolayer on a glass slide, (2) evaporation of gold or silver with thicknesses up to 100 nm, and (3) spreading of chromatography silica gels. Interestingly, they demonstrate that the TLC-SERS can separate mixture samples and provide in situ SERS spectra. We prepared two types of samples. One was a mixture consisting of equal portions of Raman-active chemical species, rhodamine 6G (R6G), crystal violet (CV), and 1,2-Di-(4-pyridyl)ethylene (BPE). The other was skim milk with a trace amount of melamine. The three-component mixture could be separated into three components and their SERS spectra could be obtained individually and that melamine added to skim milk could be detected only after separation. Additionally, the use of hierarchically assembled porous ZnO microspheres with enhanced gas-sensing properties was reported by S. You et al. The sensitivity of porous ZnO to ethanol gases increased with the increasing of ethanol concentration.

By combining these excellent results, the special issue provides advanced progress in the development of functional nanomaterials for biomedical applications and environmental monitoring.

Acknowledgment

On this chance, we would like to thank all of the authors for their contributions to the special issue. Thanks are also due to this journal for giving us a chance to edit this special issue. We do hope that you can find useful information from this special issue for your future research works.

*Anh-Tuan Le
Tran Quang Huy
Manh-Huong Phan
Nguyen Van Hieu
Tran Trong An*

Research Article

TLC-SERS Plates with a Built-In SERS Layer Consisting of Cap-Shaped Noble Metal Nanoparticles Intended for Environmental Monitoring and Food Safety Assurance

H. Takei,^{1,2} J. Saito,¹ K. Kato,¹ H. Vieker,^{3,4} A. Beyer,³ and A. Götzhäuser³

¹Department of Life Sciences, Toyo University, 1-1-1 Izumino, Itakura, Gunma 374-0193, Japan

²Bio-Nano Electronics Research Centre, Toyo University, 2100 Kujirai, Kawagoe, Saitama 350-8585, Japan

³Physics of Supramolecular Systems and Surfaces, Bielefeld University, 33615 Bielefeld, Germany

⁴CNM Technologies GmbH, 33609 Bielefeld, Germany

Correspondence should be addressed to H. Takei; h.takei@toyo.jp

Received 22 May 2015; Accepted 27 July 2015

Academic Editor: Anh-Tuan Le

Copyright © 2015 H. Takei et al. This is an open access article distributed under the Creative Commons Attribution License, which permits unrestricted use, distribution, and reproduction in any medium, provided the original work is properly cited.

We report on a thin layer chromatograph (TLC) with a built-in surface enhanced Raman scattering (SERS) layer for in-situ identification of chemical species separated by TLC. Our goal is to monitor mixture samples or diluted target molecules suspended in a host material, as happens often in environmental monitoring or detection of food additives. We demonstrate that the TLC-SERS can separate mixture samples and provide in-situ SERS spectra. One sample investigated was a mixture consisting of equal portions of Raman-active chemical species, rhodamine 6 G (R6G), crystal violet (CV), and 1,2-di(4-pyridyl)ethylene (BPE). The three components could be separated and their SERS spectra were obtained from different locations. Another sample was skim milk with a trace amount of melamine. Without development, no characteristic peaks were observed, but after development, a peak was observed at 694 cm^{-1} . Unlike previous TLC-SERS whereby noble metal nanoparticles are added after development of a sample, having a built-in SERS layer greatly facilitates analysis as well as maintaining high uniformity of noble metal nanoparticles.

1. Introduction

It is only recently that SERS is emerging as a practical analytical technique in food science and environmental monitoring [1, 2]. SERS is a powerful tool [3–5], but, for it to become a useful tool, it needs to overcome at least two problems: one has to do with reproducibility and uniformity of signals [6] and the other has to do with the fact that target molecules are almost always found in a mixture or a complex medium [7] so that the interference from the host matrix must be eliminated. The first problem is being addressed by various nanotechnological approaches for preparing requisite nanostructures. While there is any number of good reviews [8–10], broadly speaking, these techniques can be categorized into two groups depending on whether they are based on vacuum processing or wet chemistry. One popular method makes use of surface adsorbed nanospheres as a template. For example, a regular array of monodisperse nanosphere can

be used as a mask, known as nanosphere lithography (NSL) [11] or a platform onto which a metal can be evaporated to form cap-shaped nanoparticles, metal film on nanosphere (MFON) [12–14]. Antenna-like nanostructures have also been prepared by a number of groups [15, 16]. Electron-beam lithography is a powerful tool for forming nanostructures of arbitrary shape, particularly useful for controlling interparticle coupling [17]. As for methods based on wet chemistry, one can adsorb colloids of various shapes as a dense layer [18]. One can use galvanic displacement reaction for forming dendritic structures [19, 20]. It is even possible to hollow triangular nanoparticles [21]. All these structures have proven to be effective SERS plates.

As for the issue of detecting target molecules in complex media, workers have been attempting to combine SERS with a separation technique such as TLC [22]. This popular method is used for separating low molecular weight molecules. A mixture sample is spotted onto a thin layer of silica gels

functioning as a stationary phase. A solvent added to the TLC plates migrates through the gel layer via capillary action. Molecules carried by the flow of the solvent can be separated if their affinities toward the stationary and mobile phases are different. The idea of combining SERS with a TLC plate dates back to 1980s and it is often referred to as TLC-SERS [2, 22]. These two techniques are compatible because both TLC and SERS usually employ a flat substrate. Typically, a mixture sample is developed on a commercial TLC plate, and after separation of the mixture into components, silver or gold colloids are added to obtain SERS spectra. A large variety of samples have been measured with such a scheme which include artist dye stuff in fiber [23], apomorphine in human plasma [24], organophosphates pesticide methidathion in tea leaves [25], Syrian rue (*Peganum harmala*) and its alkaloid constituents [26], adulterants in botanical dietary supplements [27], mauve [28], ephedrine and its analogues in slimming dietary supplements [29], and anticancer drug irinotecan in presence of human serum albumin [30]. More recently, spraying of colloids, rather than simply placing a drop of colloids, was reported as an effective way to improve the data quality [31]. Nonetheless, two problems are foreseen with such approaches. For one, colloids are not likely to adsorb uniformly onto the gel layer. They are likely to disperse throughout the entire thickness of the gel layer so that only a small proportion of dispensed nanoparticles are expected to be found in the focal plane of the excitation laser and are thus able to contribute to the overall signal. Another potential problem is that the act of dispensing colloids is likely to disturb separated target molecules. To overcome these problems, some have attempted to transfer separated molecules onto a separate preprepared SERS plate by blotting for the same purpose [32]. In order to increase the utility of TLC-SERS, however, it would be natural to attempt preparation of a TLC structure which has a built-in SERS structure. This would eliminate the need to apply noble metal colloids after development. Chen et al. have reported the use of silver nanorods prepared from oblique angle deposition [33]. By using a silver nanorod layer both for separation and detection, they have demonstrated that various components within a mixture could be separated and individually identified. Specifically, they separated R6G from melamine at various molecules concentrations. Kim et al. have reported forming gold nanofingers in a pentamer configuration and detected melamine in milk [34].

Here we report a simple method for making a structure consisting of a separation gel layer and a SERS layer as an integrated structure. A thin but dense SERS layer is formed over a glass substrate, covered by a separation gel layer. Having the SERS layer on the glass substrate allows us to detect SERS signals by irradiating from below, thus avoiding interference from the gel layer. The SERS layer is less than 150 nm thick, so that the entire layer can be effectively utilized upon irradiation.

While the separation gel layer consists of thinly spread commercially available gel, the SERS layer consists of a modified metal film on nanosphere (MFON) structure. The traditional MFON structure is prepared by formation of a regular array of highly monodisperse nanospheres, followed

by deposition of a metal layer. This has been shown to serve as an effective SERS substrate [35–37]. In contrast, our method, random MFON, makes use of a randomly adsorbed layer of quasi-monodisperse nanospheres [38]. Such structures have been successfully used for localized surface plasmon resonance (LSPR) sensing and surface-enhanced fluorescence measurements [39–41]. We show that the random MFON is an ideal structure for integration into a TLC-SERS, due to simplicity of preparation and significant SERS effect.

We first show that the SERS layer within a TLC-SERS can effectively enhance Raman signals. This is done by immersing a TLC-SERS plate and a TLC structure without SERS layer into a BPE solution and taking Raman spectra from them. Then, we demonstrate that the TLC-SERS can actually separate mixture samples and provide in situ SERS spectra. For demonstration, we prepared two types of samples. One is a mixture of equal portions of Raman-active chemical species. We show that the three-component mixture consisting of R6G, CV, and BPE could be separated and SERS spectra of all three components could be obtained individually. A series of spectra along the direction of the development were obtained with a 2 mm interval in the range from 2 mm to 28 mm from the origin; a more detailed investigation was carried out in the range from 15.5 mm to 20.5 mm with a 0.5 mm interval. It revealed distinct SERS spectra from different locations from the origin. With skim milk doped with a trace amount of melamine, the presence of 10 mg of melamine added to 1 g of skim milk could be detected only after separation with the TLC-SERS whereas before separation, skim milk prevented detection of melamine.

We will also show that both gold and silver nanoparticles can be used. Silver nanoparticles have the advantage of being applicable to a greater variety of excitation lasers spanning the entire visible spectrum while their disadvantage lies with their chemical instability. In the past, PVP has been reported effective for stabilizing silver nanocolloids [42, 43]. We will show that PVP can indeed improve the stability without reduction in SERS peak height.

2. Experimental

2.1. TLC-SERS Preparation. Preparation of a SERS layer starts with surface modification of a glass slide with 3-aminopropyltrimethoxysilane, APTMS. After a slide (Matsunami Glass Inc., Ltd., Fine Frost, FF-002, Osaka, Japan) was immersed in an APTMS (1 wt.%) solution (Wako Pure Chemical Industries, Ltd., Cat. number 323-74352, Osaka, Japan) for one minute, it was dried in a home-made dryer at 60-degree Celsius for a few minutes. A SiO₂ nanosphere suspension (Polysciences Inc., Uniform Silica Microspheres 0.1 microns, Cat. number 24041, Warrington, PA), diluted twofold by an equal portion of 7.5 mM MgCl₂ solution, was added to the surface-modified glass slide, to cover a 5 mm by 60 mm rectangular area defined by hydrophobic adhesive tape. SiO₂ nanospheres would become rapidly attached to the surface, with the saturation limit reached in less than a few minutes; it is assumed that unreacted siloxane groups present on the glass slide bind the nanospheres. The purpose of adding MgCl₂ is to increase the adsorption density. Excess

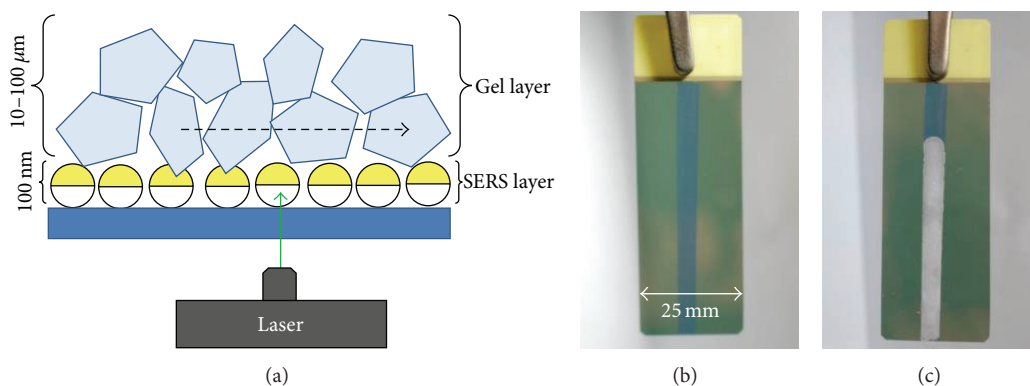


FIGURE 1: TLC-SERS plate with a built-in SERS layer. (a) Its cross-sectional schematic and photographs during preparation, after formation of a SERS layer (b) and a separation gel layer (c).

nanospheres were washed off with a copious amount of water, leaving a dense monolayer of SiO_2 nanospheres. Finally, a 40 nm thick Au layer was deposited by vacuum evaporation by using the VFR-200 M/ERH vacuum evaporator (ULVAC KIKO, Inc., Miyazaki, Japan), with a typical vacuum of 5×10^{-3} Pa at a deposition rate of 1 nm/sec.

The SERS layer was then covered by a separation gel layer. Silica gel (GF60254, Merck Inc.) was suspended in deionized water at the concentration of 0.1 g/mL. 200 μL of the mixture was added to the glass slide and spread over the SERS layer. It was then dried at 60-degree Celsius.

2.2. Measurement of SERS Spectra. The fundamental performance of the TLC-SERS as a SERS substrate was evaluated using the Nicolet Almega XR (Thermo Fisher Scientific Inc.) with the excitation wavelength of 633 nm.

2.3. Preparation of Detection Target Molecules. BPE and R6G were purchased from Sigma-Aldrich Inc. (Cat. number B52808-5G and R4127-5G St. Louis, MO). CV was purchased from Wako (Cat. number 038-04862). R6G, CV, and BPE were prepared as 1 mM solutions; R6G and CV were directly dissolved into water whereas BPE was first dissolved in methanol at the concentration of 10 mM, followed by tenfold dilution with water for the final concentration of 1 mM.

Melamine was purchased from Kanto Chemical Co., Inc. (Cat. number 25093-02 Tokyo, Japan) and used as received. 10 mg of melamine was thoroughly mixed with 10 g of skim milk by shaking for several minutes (Morinaga Skim Milk; <http://www.morinagamilk.co.jp/skim>). One gram of the powder mixture was dissolved into 10 mL of deionized water.

Malachite green used to evaluate PVP coating was obtained from Waldeck GmbH & Co. KG. (Cat. number IB-249 Münster, Germany).

2.4. Protection by Polyvinylpyrrolidone. PVP was purchased from Wako (PVP K30 Cat. number 165-17035), with the molecular weight of 30,000. One gram of PVP powder was dissolved into 99 mL of deionized water. A plate with Ag nanoparticles was immersed into the PVP solution for 30 min and subsequently dried at 60-degree Celsius. We chose a

1 wt.% 30,000 PVP solution, but PVP with other molecular weights such as 15,000 and 90,000 were found to work as well.

2.5. Chromatography. For the mobile phase, we used a methanol: water (80:20) mixture for the three-component experiment and 100% methanol for the skim milk experiment. 0.2 μL of the target molecule solution was added to the plate, at a point 1 cm away from the edge with four separate application rounds, with an interval of a few minutes for drying. The plate was placed in a 50 mL bottle filled with 2 mL of the mobile phase. A screw-on top was used to seal the bottle. Development was allowed to run until components were visibly separated from each other.

2.6. Morphology Observation. For characterization of morphology, we employed a helium ion microscope, HIM, rather than a scanning electron microscope, SEM. With the gel layer on the TLC-SERS, it was exceedingly difficult to prevent electrical charging under SEM observation even when the structure was coated with Pt. HIM images obtained with a Carl Zeiss Orion Plus were clear. The helium ion beam was operated at 35 kV acceleration voltage at a current of 0.5 pA and scanned over the sample with a dwell time of 0.5 μs at 32 lines averaging. We used the in-built electron flood gun at about 680 eV in line mode to compensate for charging. The sample was under a tilt angle of 43° . Brightness and contrast of all images were optimized for best visibility. For structures without the TLC layer, images were obtained with an SEM, Hitachi SU8000 at the acceleration voltage of 5.0 kV.

3. Results and Discussion

Figure 1 shows our TLC-SERS plate, (a) a schematic diagram of the cross section and its photographs during preparation, after formation of a SERS layer (b), and a separation gel layer (c). The SERS layer is 5 mm wide and 60 mm long, and the separation gel layer, white in appearance, has the same width. The width of 5 mm was chosen from our observation that the sample tended to drift toward an edge during development when narrower strips were used. Figure 2 shows HIM images of the TLC-SERS plate. The separation gel layer was locally removed to reveal the underlying SERS layer. Images (a) and

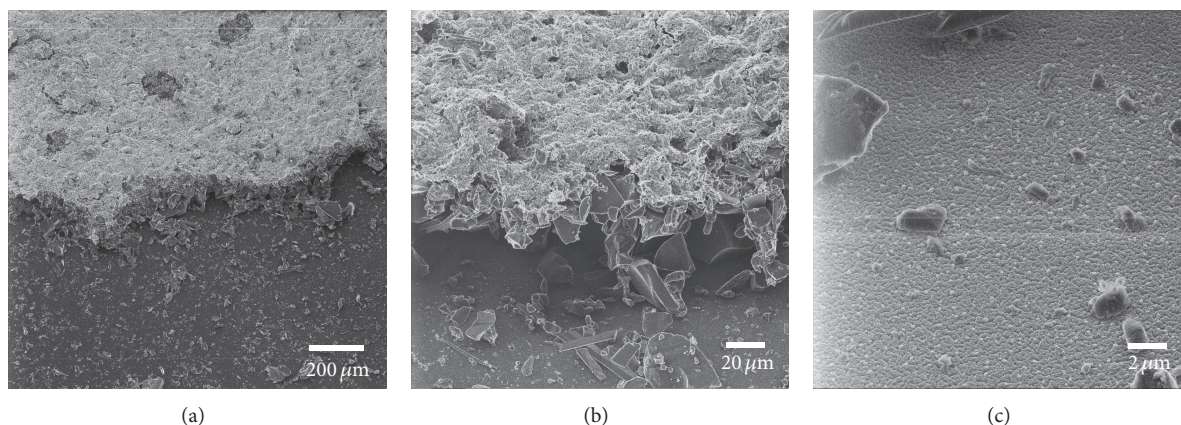


FIGURE 2: HIM images of the TLC-SERS plate with a locally removed separation gel layer. The scale bars correspond, respectively, to 200, 20, and 2 μm in (a), (b), and (c).

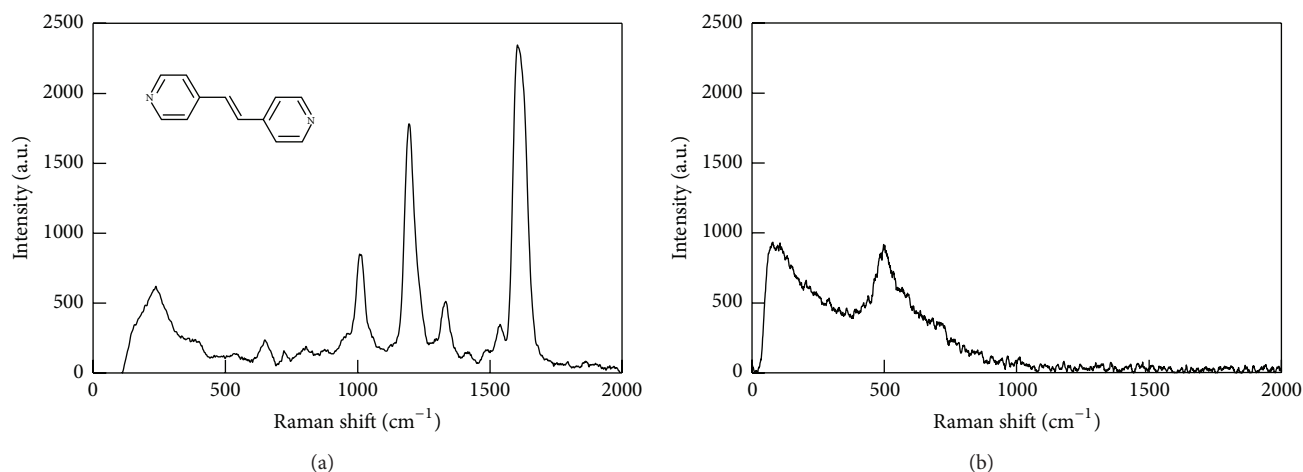


FIGURE 3: Raman spectra of 0.1 mM BPE from a TLC-SERS plate (a) and a TLC plate without SERS layer (b).

(b) reveal the cross section of the separation gel layer whereby the bottom half is the SERS layer. In image (c) details of the SERS layer are shown. Structures some 100 nm in size are responsible for SERS and debris larger than 1 μm is fragments from the separation gel layer. The scale bar corresponds to 200, 20, and 2 μm in (a), (b), and (c), respectively. The separation gel layer is some 100 μm thick. Nanoparticles in the SERS layer remained adsorbed to the glass surface and they did not undergo noticeable morphological changes in the process of forming the separation gel layer on top.

Next we show that the SERS layer in the TLC-SERS plate is effective for enhancing Raman signals. Figure 3 shows spectra obtained from a TLC-SERS plate and a regular TLC plate without SERS layer after both were exposed to 0.1 mM BPE. Here BPE was not developed because our interest was to see if the SERS layer would function after incorporation into a TLC-SERS plate. Peaks seen at 1010, 1195, 1333, and 1604 cm^{-1} in Figure 3(a) are characteristic of BPE. They have been assigned to ring in-plane deformation (ring breathing) (1009 cm^{-1}), $\nu(\text{ring-C}_\nu)$, $\delta(\text{C-H})_p$ (1219 cm^{-1}), $\delta(\text{C-H})$, $\delta(\text{C}_\nu\text{-C})$ (1350 cm^{-1}), and $\nu(\text{C-C})_p$, $\delta(\text{C-H})$ (1631 cm^{-1}) by

Zhuang et al. [44]. These peaks cannot be observed in the absence of the SERS layer (Figure 3(b)).

Next we investigated whether the presence of the SERS layer interfered with the separation process. Figure 4(a) shows an image of a TLC-SERS plate after development of a BPE/R6G/CV mixture sample. The origin is at 0 mm and the orange spot corresponding to R6G is found 17 mm from the origin whereas CV is found in a region expanding up to 15 mm from the origin; BPE is not visible to the naked eye. A series of spectra obtained along the length of the plate at a 2 mm interval are shown in Figure 4(b). Spectra obtained at a 0.5 mm interval in the range from 15.5 and 20.5 mm are shown in (c). Spectra characteristic of CV and R6G were obtained from locations corresponding to two colored spots of Figure 4(a). Spectra characteristic of BPE were obtained from locations further away than R6G, as far away as 20 mm from the origin. It can be seen, thus, that BPE, R6G, and CV could be separated and their SERS spectra could be obtained in situ. It should be mentioned, however, that even though Figure 4(a) does not show any obvious colored spot at the origin, a SERS spectrum which is

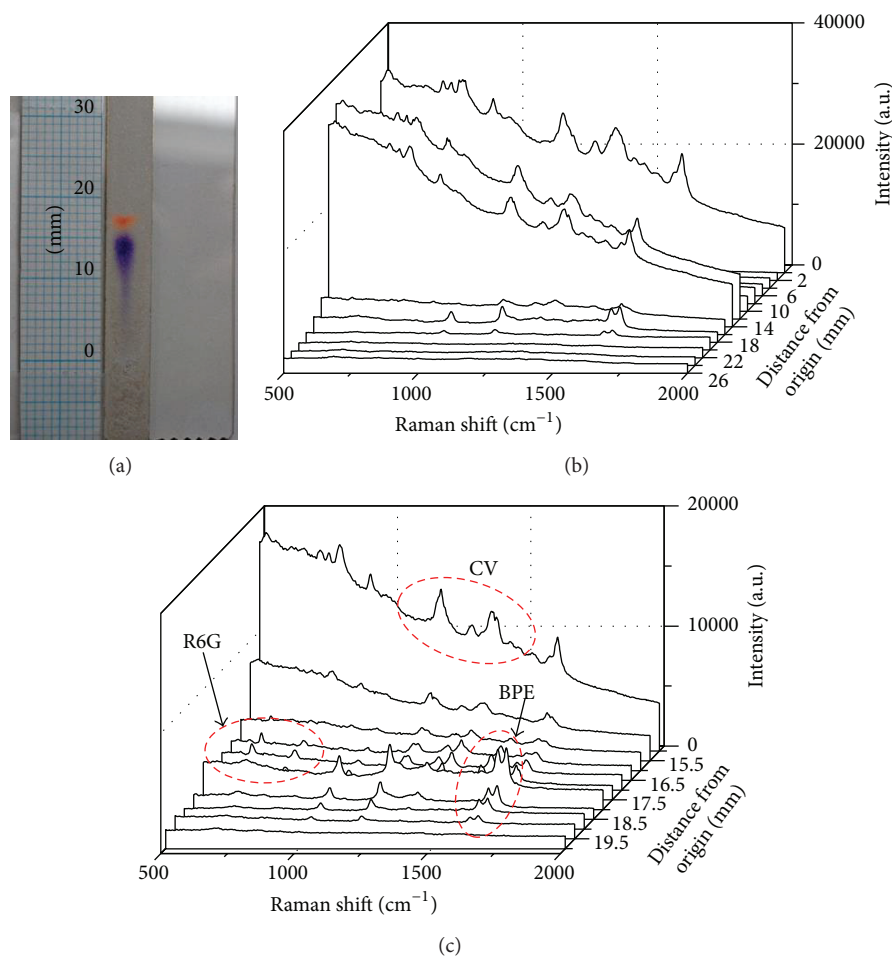


FIGURE 4: Image of a TLC-SERS after the BPE/R6G/CV mixture sample has been run (a). SERS spectra obtained along the direction of plate with a 2 mm interval from the origin are shown in (b). Those taken with a 0.5 mm interval in the range from 15.5 and 20.5 mm are shown in (c).

largely that of CV is obtained from the origin. Some possible explanations for this are that (1) those CV molecules present at the origin get adsorbed to gold nanoparticles particularly tightly so as to give exceptionally strong SERS signals, (2) as the rest of the CV molecules migrate, only a small portion manages to come into contact with nanoparticles in the SERS layer, and (3) the nanoparticles at the origin undergo morphological change during the spotting process in such a way to improve the enhancement ratio and so forth. For now, we can only hypothesize about the mechanism, but the fundamental principle of separation and subsequent *in situ* SERS detection has been shown.

Results of running a melamine/skim milk mixture are shown in Figure 5. The spectrum in (a) was obtained from the origin immediately after the mixture was added, before development. No peak characteristic of melamine was observed. After development, spectra were obtained at the origin and three spots 5, 10, and 15 mm from the origin, shown in Figures 5(b), 5(c), and 5(d), respectively. In Figure 5(c), there is a peak at 694 cm^{-1} which should correspond to the ring breathing mode for melamine in solution [45]. The same peak

of reduced height is also observed in Figures 5(b) and 5(d) so that melamine might not be optimally isolated, but separation is sufficient to reveal the 694 cm^{-1} peak, previously blocked by the skim milk. There are a number of reports on detection of melamine added to milk or skim milk [34, 46–48]. While it may be possible to detect melamine without separation under certain conditions, the present result suggests that the presence of milk or skim milk does affect the SERS peak height so that a separation step is necessary for quantitative measurements.

The protection effect of the PVP coating on Ag nanoparticles, 100 nm nanospheres covered by 100 nm Ag, is illustrated in Figure 6. The plate shown in (a) is protected only on the side left of the broken line in the middle. Colors of the SERS layer are different on the left and right of the line. Two SEM images reveal the effect of forming a TLC layer over Ag nanoparticles. First a TCL layer was formed and then removed to reveal the underlying SERS layer. In Figure 6(b), Ag nanoparticles had been protected by PVP whereas those in (c) had not been. Protected silver nanoparticles retained their original shape as can be seen in Figure 6(b), but those

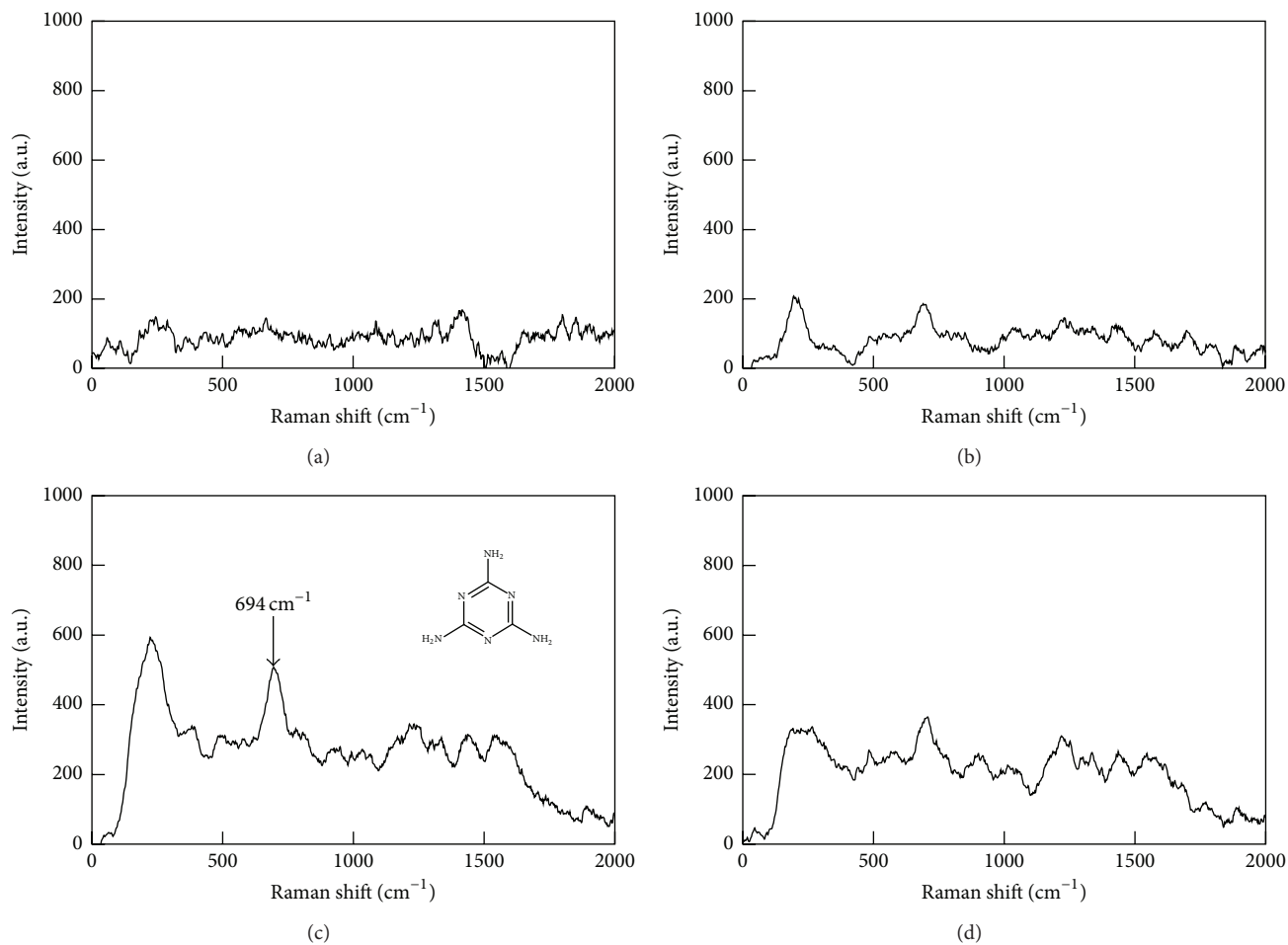


FIGURE 5: Spectra obtained before (a) and after development of a melamine/skim milk mixture from various locations along the length of the TLC-SERS plate, (b), (c), and (d). They correspond to locations 5, 10, and 15 mm from the origin.

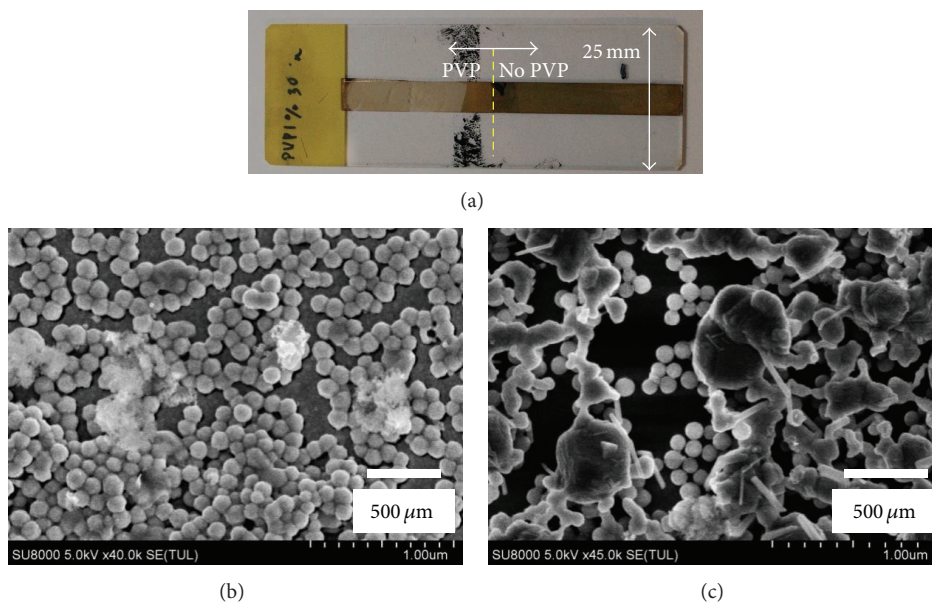


FIGURE 6: A photo of a TLC-SERS (a); only the left side of the central broken line was protected. Of the SEM images in (b) and (c), (b) shows the protected area.

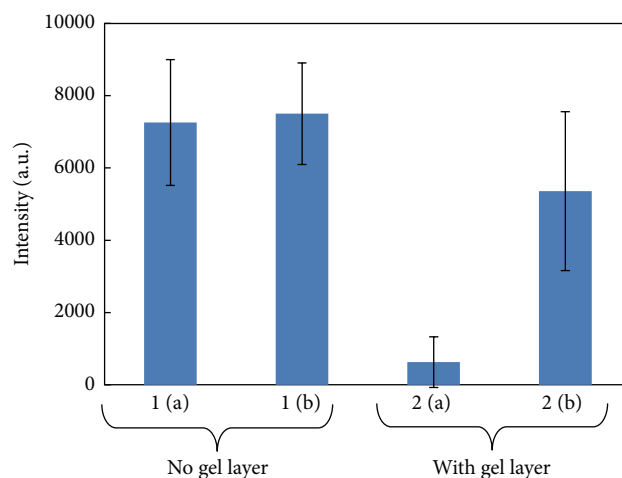


FIGURE 7: The effect of PVP protection of silver nanoparticles on 912 cm^{-1} peak intensities from malachite green. 1 (a) and 2 (a) are without PVP protection, before and after application of the separation gel layer, respectively. 1 (b) and 2 (b) show signals from PVP-protected silver nanoparticles.

in Figure 6(c) turned into globules. The effect of PVP coating was also evaluated through SERS spectra. The height of the 912 cm^{-1} peak in malachite green SERS spectra was used as the standard. In Figure 7, those on the left, 1 (a) and 1 (b), are signal intensities from SERS plates not covered by a TLC layer. Whether protected by PVP (1 (a)) or not (1 (b)), the signal intensities were comparable. This shows that having PVP coating did not interfere with SERS measurements. Two on the right, 2 (a) and 2 (b), are both of TLC-SERS plates; 2 (b) is the signal from a TLC-SERS with PVP protection. 2 (a) is without PVP protection prior to formation of the TLC layer. While there is reduction in the signal intensity for both cases, the PVP coating was effective in minimizing the loss in performance. PVP might prevent Raman-active target molecules from directly adsorbing onto noble metal nanoparticles, but the reduction in the signal intensity was minimal. Silver is a material of choice because it can be used in combination with a larger variety of excitation lasers with different wavelengths. Thus, the ability to incorporate silver nanoparticles into a TLC-SERS is encouraging.

We showed in this paper that a TLC-SERS can be prepared with a built-in SERS layer. The predominant advantage is simplicity in operation, important particularly in the field, where no facility is available for careful application of noble metal colloids or transfer of separated chemical species from a TLC plate onto a separate SERS plate after development. With a built-in SERS layer, one can be more certain of uniformity of noble metal colloids. Additionally, use of randomly adsorbed noble metal nanoparticles has the following advantages: (1) it is easier to prepare than orderly arrays and (2) there have been reports of enhanced SERS performance with randomly adsorbed nanoparticles [36].

4. Conclusion

We showed that a TLC-SERS plate can be prepared with a built-in SERS layer. The SERS layer is formed by adsorption of quasi-monodisperse SiO_2 nanoparticles followed by vacuum

deposition of a noble metal. This simple method allows formation of a SERS layer measuring an area 60 mm by 5 mm on a slide glass. The TLC-SERS plate is completed by formation of a separation gel layer on top of the SERS layer. This structure was used to detect R6G, CV, and BPE from their mixture sample. After development of the sample, SERS spectra of these chemical species were obtained from distinct spots on the TLC-SERS plate. The plate was also used to detect the presence of a trace amount of melamine dispersed within skim milk. Before development, no peak characteristic of melamine was obtained, but after development, the 694 cm^{-1} peak was detected. It shows that the TLC-SERS plate is capable of reducing the interference from the skim milk.

A built-in SERS layer has the advantage of uniformity over a system whereby colloids are added to a TLC plate after development. The fact that the SERS layer is located directly on the flat glass substrate gives an additional advantage that the nanoparticles can be easily irradiated from the bottom, not blocked by the gel layer. It is hoped that the reported system will prove itself useful, particularly when measurements are to be made outside a laboratory where cumbersome preparatory procedures need to be minimized.

Conflict of Interests

The authors declare that there is no conflict of interests regarding the publication of this paper.

References

- [1] J. Zheng and L. He, "Surface-enhanced Raman spectroscopy for the chemical analysis of food," *Comprehensive Reviews in Food Science and Food Safety*, vol. 13, no. 3, pp. 317–328, 2014.
- [2] D. Li, L. Qu, W. Zhai, J. Xue, J. S. Fossey, and Y. Long, "Facile on-site detection of substituted aromatic pollutants in water using thin layer chromatography combined with surface-enhanced Raman spectroscopy," *Environmental Science and Technology*, vol. 45, no. 9, pp. 4046–4052, 2011.

- [3] M. Moskovits, "Surface-enhanced Raman spectroscopy: a brief retrospective," *Journal of Raman Spectroscopy*, vol. 36, no. 6-7, pp. 485-496, 2005.
- [4] B. Sharma, M. F. Cardinal, S. L. Kleinman et al., "High-performance SERS substrates: advances and challenges," *MRS Bulletin*, vol. 38, no. 8, pp. 615-624, 2013.
- [5] L. Tong, H. Xu, and M. Käll, "Nanogaps for SERS applications," *MRS Bulletin*, vol. 39, no. 2, pp. 163-168, 2014.
- [6] I. A. Larmour and D. Graham, "Surface enhanced optical spectroscopies for bioanalysis," *Analyst*, vol. 136, no. 19, pp. 3831-3853, 2011.
- [7] R. H. Farahi, A. Passian, L. Tetard, and T. Thundat, "Critical issues in sensor science to aid food and water safety," *ACS Nano*, vol. 6, no. 6, pp. 4548-4556, 2012.
- [8] M. Rycenga, C. M. Cobley, J. Zeng et al., "Controlling the synthesis and assembly of silver nanostructures for plasmonic applications," *Chemical Reviews*, vol. 111, no. 6, pp. 3669-3712, 2011.
- [9] M. A. Garcia, "Surface plasmons in metallic nanoparticles: fundamentals and applications," *Journal of Physics D: Applied Physics*, vol. 44, Article ID 283001, 20 pages, 2011.
- [10] S. Hayashi and T. Okamoto, "Plasmonics: visit the past to know the future," *Journal of Physics D: Applied Physics*, vol. 45, no. 43, Article ID 433001, 2012.
- [11] A. D. Ormonde, E. C. M. Hicks, J. Castillo, and R. P. Van Duyne, "Nanosphere lithography: fabrication of large-area Ag nanoparticle arrays by convective self-assembly and their characterization by scanning UV-visible extinction spectroscopy," *Langmuir*, vol. 20, no. 16, pp. 6927-6931, 2004.
- [12] N. G. Greeneltch, M. G. Blaber, A.-I. Henry, G. C. Schatz, and R. P. Van Duyne, "Immobilized nanorod assemblies: fabrication and understanding of large area surface-enhanced Raman spectroscopy substrates," *Analytical Chemistry*, vol. 85, no. 4, pp. 2297-2303, 2013.
- [13] C. Farcau and S. Astilean, "Mapping the SERS efficiency and hot-spots localization on gold film over nanospheres substrates," *Journal of Physical Chemistry C*, vol. 114, no. 27, pp. 11717-11722, 2010.
- [14] Y. Fang, N.-H. Seong, and D. D. Dlott, "Measurement of the distribution of site enhancements in surface-enhanced Raman scattering," *Science*, vol. 321, no. 5887, pp. 388-392, 2008.
- [15] R. A. Tripp, R. A. Dluhy, and Y. Zhao, "Novel nanostructures for SERS biosensing," *Nano Today*, vol. 3, no. 3-4, pp. 31-37, 2008.
- [16] P. Dawson, J. A. Duenas, M. G. Boyle et al., "Combined antenna and localized plasmon resonance in Raman scattering from random arrays of silver-coated, vertically aligned multiwalled carbon nanotubes," *Nano Letters*, vol. 11, no. 2, pp. 365-371, 2011.
- [17] L. Gunnarsson, E. J. Bjerneld, H. Xu, S. Petronis, B. Kasemo, and M. Käll, "Interparticle coupling effects in nanofabricated substrates for surface-enhanced Raman scattering," *Applied Physics Letters*, vol. 78, no. 6, pp. 802-804, 2001.
- [18] B. Peng, G. Li, D. Li et al., "Vertically aligned gold nanorod monolayer on arbitrary substrates: self-assembly and femtomolar detection of food contaminants," *ACS Nano*, vol. 7, no. 7, pp. 5993-6000, 2013.
- [19] L. He, M. Lin, H. Li, and N.-J. Kim, "Surface-enhanced Raman spectroscopy coupled with dendritic silver nanosubstrate for detection of restricted antibiotics," *Journal of Raman Spectroscopy*, vol. 41, no. 7, pp. 739-744, 2010.
- [20] A. Gutiérrez, C. Carraro, and R. Maboudian, "Silver dendrites from galvanic displacement on commercial aluminum foil as an effective SERS substrate," *Journal of the American Chemical Society*, vol. 132, no. 5, pp. 1476-1477, 2010.
- [21] G. S. Métraux, Y. C. Cao, R. Jin, and C. A. Mirkin, "Triangular nanoframes made of gold and silver," *Nano Letters*, vol. 3, no. 4, pp. 519-522, 2003.
- [22] L. Kocsis, E. Horváth, J. Kristóf, R. L. Frost, Á. Rédey, and J. Mink, "Effect of the preparation conditions on the surface-enhanced Raman-spectrometric identification of thin-layer-chromatographic spots," *Journal of Chromatography A*, vol. 845, no. 1-2, pp. 197-202, 1999.
- [23] C. L. Brosseau, A. Gambardella, F. Casadio, C. M. Grzywacz, J. Wouters, and R. P. Van Duyne, "Ad-hoc surface-enhanced Raman spectroscopy methodologies for the detection of artist dyestuffs: thin layer chromatography-surface enhanced Raman spectroscopy and in situ on the fiber analysis," *Analytical Chemistry*, vol. 81, no. 8, pp. 3056-3062, 2009.
- [24] A. Lucotti, M. Tommasini, M. Casella, A. Morganti, F. Gramatica, and G. Zerbi, "TLC-surface enhanced Raman scattering of apomorphine in human plasma," *Vibrational Spectroscopy*, vol. 62, pp. 286-291, 2012.
- [25] C. Yao, F. Cheng, C. Wang et al., "Separation, identification and fast determination of organophosphate pesticide methidathion in tea leaves by thin layer chromatography-surface-enhanced Raman scattering," *Analytical Methods*, vol. 5, no. 20, pp. 5560-5564, 2013.
- [26] F. Pozzi, N. Shibayama, M. Leona, and J. R. Lombardi, "TLC-SERS study of Syrian rue (*Peganum harmala*) and its main alkaloid constituents," *Journal of Raman Spectroscopy*, vol. 44, no. 1, pp. 102-107, 2013.
- [27] Q. Zhu, Y. Cao, Y. Cao, Y. Chai, and F. Lu, "Rapid on-site TLC-SERS detection of four antidiabetic drugs used as adulterants in botanical dietary supplements," *Analytical and Bioanalytical Chemistry*, vol. 406, no. 7, pp. 1877-1884, 2014.
- [28] M. V. Cañamares, D. A. Reagan, J. R. Lombardi, and M. Leona, "TLC-SERS of mauve, the first synthetic dye," *Journal of Raman Spectroscopy*, vol. 45, no. 11-12, pp. 1147-1152, 2014.
- [29] D. Lv, Y. Cao, Z. Lou et al., "Rapid on-site detection of ephedrine and its analogues used as adulterants in slimming dietary supplements by TLC-SERS," *Analytical and Bioanalytical Chemistry*, vol. 407, pp. 1313-1325, 2014.
- [30] A. Vicario, V. Sergio, G. Toffoli, and A. Bonifacio, "Surface-enhanced Raman spectroscopy of the anti-cancer drug irinotecan in presence of human serum albumin," *Colloids and Surfaces B: Biointerfaces*, vol. 127, pp. 41-46, 2015.
- [31] Z.-M. Zhang, J.-F. Liu, R. Liu, J.-F. Sun, and G.-H. Wei, "Thin layer chromatography coupled with surface-enhanced Raman scattering as a facile method for on-site quantitative monitoring of chemical reactions," *Analytical Chemistry*, vol. 86, no. 15, pp. 7286-7292, 2014.
- [32] C. E. Freye, N. A. Crane, T. B. Kirchner, and M. J. Sepaniak, "Surface enhanced Raman scattering imaging of developed thin-layer chromatography plates," *Analytical Chemistry*, vol. 85, no. 8, pp. 3991-3998, 2013.
- [33] J. Chen, J. Abell, Y.-W. Huang, and Y. Zhao, "On-chip ultrathin layer chromatography and surface enhanced Raman spectroscopy," *Lab on a Chip*, vol. 12, no. 17, pp. 3096-3102, 2012.
- [34] A. Kim, S. J. Barcelo, R. S. Williams, and Z. Li, "Melamine sensing in milk products by using surface enhanced Raman scattering," *Analytical Chemistry*, vol. 84, no. 21, pp. 9303-9309, 2012.
- [35] X. Zhang, J. Zhao, A. V. Whitney, J. W. Elam, and R. P. Van Duyne, "Ultrastable substrates for surface-enhanced Raman

- spectroscopy: Al₂O₃ overlayers fabricated by atomic layer deposition yield improved anthrax biomarker detection,” *Journal of the American Chemical Society*, vol. 128, no. 31, pp. 10304–10309, 2006.
- [36] M. Baia, L. Baia, and S. Astilean, “Gold nanostructured films deposited on polystyrene colloidal crystal templates for surface-enhanced Raman spectroscopy,” *Chemical Physics Letters*, vol. 404, no. 1–3, pp. 3–8, 2005.
- [37] Y. Zhang, W. Gao, S. Yang et al., “Nanogaps in 2D Ag-nanocap arrays for surface-enhanced Raman scattering,” *Journal of Raman Spectroscopy*, vol. 44, no. 12, pp. 1666–1670, 2013.
- [38] H. Takei, “Surface-adsorbed polystyrene spheres as a template for nanosized metal particle formation: optical properties of nanosized Au particle,” *Journal of Vacuum Science and Technology B: Microelectronics and Nanometer Structures*, vol. 17, no. 5, pp. 1906–1911, 1999.
- [39] M. Himmelhaus and H. Takei, “Cap-shaped gold nanoparticles for an optical biosensor,” *Sensors and Actuators, B: Chemical*, vol. 63, no. 1, pp. 24–30, 2000.
- [40] T. Yamaguchi, T. Kaya, M. Aoyama, and H. Takei, “Surface-adsorbed silver half-shells as a platform for surface-enhanced immunoassays; optimization through morphological control,” *Analyst*, vol. 134, no. 4, pp. 776–783, 2009.
- [41] H. Takei and T. Yamaguchi, “A combinatorial approach toward fabrication of surface-adsorbed metal nanoparticles for investigation of an enzyme reaction,” *Physical Chemistry Chemical Physics*, vol. 12, no. 17, pp. 4505–4514, 2010.
- [42] S. Kittler, C. Greulich, M. Köller, and M. Epple, “Synthesis of PVP-coated Silver nanoparticles and their biological activity towards human mesenchymal stem cells,” *Materialwissenschaft und Werkstofftechnik*, vol. 40, no. 4, pp. 258–264, 2009.
- [43] S. Zhu, C. Fan, J. Wang, J. He, and E. Liang, “Surface-enhanced Raman scattering of 4-mercaptobenzoic acid and hemoglobin adsorbed on self-assembled Ag monolayer films with different shapes,” *Applied Physics A*, vol. 117, no. 3, pp. 1075–1083, 2014.
- [44] Z. Zhuang, X. Shi, Y. Chen, and M. Zuo, “Surface-enhanced Raman scattering of trans-1,2-bis(4-pyridyl)-ethylene on silver by theory calculations,” *Spectrochimica Acta—Part A: Molecular and Biomolecular Spectroscopy*, vol. 79, no. 5, pp. 1593–1599, 2011.
- [45] L. He, Y. Liu, M. Lin et al., “A new approach to measure melamine, cyanuric acid, and melamine cyanurate using surface enhanced Raman spectroscopy coupled with gold nanosubstrates,” *Sensing & Instrumentation for Food Quality and Safety*, vol. 2, no. 1, pp. 66–71, 2008.
- [46] M. Lin, L. He, J. Awika et al., “Detection of melamine in gluten, chicken feed, and processed foods using surface enhanced Raman spectroscopy and HPLC,” *Journal of Food Science*, vol. 73, no. 8, pp. T129–T134, 2008.
- [47] S. Y. Lee, E.-O. Ganbold, J. Choo, and S.-W. Joo, “Detection of melamine in powdered milk using surface-enhanced Raman scattering with no pretreatment,” *Analytical Letters*, vol. 43, no. 14, pp. 2135–2141, 2010.
- [48] X.-F. Zhang, M.-Q. Zou, X.-H. Qi, F. Liu, X.-H. Zhu, and B.-H. Zhao, “Detection of melamine in liquid milk using surface-enhanced Raman scattering spectroscopy,” *Journal of Raman Spectroscopy*, vol. 41, no. 12, pp. 1655–1660, 2010.

Research Article

Controlled Synthesis of Hierarchically Assembled Porous ZnO Microspheres with Enhanced Gas-Sensing Properties

Shengsheng You,¹ Haojie Song,¹ Jing Qian,¹ Ya-li Sun,¹ and Xiao-hua Jia²

¹Institute of Polymer Materials, School of Materials Science & Engineering, Jiangsu University, Zhenjiang 212013, China

²School of Environment and Safety Engineering, Jiangsu University, Zhenjiang, Jiangsu 212013, China

Correspondence should be addressed to Xiao-hua Jia; xhjia2003@126.com

Received 7 April 2015; Revised 13 July 2015; Accepted 16 July 2015

Academic Editor: Nguyen V. Hieu

Copyright © 2015 Shengsheng You et al. This is an open access article distributed under the Creative Commons Attribution License, which permits unrestricted use, distribution, and reproduction in any medium, provided the original work is properly cited.

The ZnO microspheres constructed by porous nanosheets were successfully synthesized by calcinating zinc hydroxide carbonate (ZHC) microspheres obtained by a simple hydrothermal method. The samples were characterized in detail with scanning electron microscopy (SEM), transmission electron microscopy (TEM), X-ray diffraction (XRD), and thermogravimetric and differential scanning calorimetry (TG-DSC). The results indicated that the prepared ZnO microspheres were well crystalline with wurtzite hexagonal phase. The effects of reaction time, temperature, the amount of trisodium citrate, and urea on the morphology of ZnO microspheres were studied. The formation mechanism of porous ZnO microspheres was discussed. Furthermore, the gas-sensing properties for detection of organic gas of the prepared porous ZnO microspheres were investigated. The results indicated that the prepared porous ZnO microspheres exhibited high gas-sensing properties for detection of ethanol gas.

1. Introduction

Zinc oxide (ZnO) is one of the most important n-type semiconductor materials with a direct wide band gap (3.37 eV) and large excitation binding energy (60 meV) [1]. It has attracted great attention for a long time due to its luminous, piezoelectric, electroconductive, gas-sensing, and photocatalytic [2–6] properties that has broad applications in the field such as lighting emitting diode, ultraviolet detectors, gas sensors, varistors, solar cells, and photocatalysts [7–12]. In addition, ZnO has abundant raw materials, cheap price, no toxicity, and simple synthetic method [13], and therefore ZnO has been recognized as one of the most important promising semiconductor materials. More and more research groups have been concentrated on using ZnO as a gas sensor for a variety of gases such as NH₃, formaldehyde, CO, H₂S, ethanol, and NO₂ [14–19]. In recent years, many researchers have devoted themselves to synthesis of ZnO with different morphologies for special applications. To date, ZnO with various size and morphologies have been reported, such as one-dimensional ZnO nanostructures, including nanotubes, nanorods, and nanowires, and two-dimensional (2D) ZnO nanosheets, nanofilm [20–24]. However, compared with

those ZnO materials above, 3D ZnO structures exhibited superior gas-sensing properties [25], which may be attributed to their high specific surface area, good permeability, and high interfacial charge-transfer efficiency [26].

It is known that the morphology, microstructures, and gas-sensing activity of ZnO are significantly influenced by the preparative conditions and methods. Numerous chemical and physicochemical methods have been developed to synthesize the 3D ZnO nanostructures. For example, Gu et al. [27] synthesized 3D flower-like ZnO nanostructures by microwave-assisted method. Li et al. [28] fabricated ZnO 3D microstructures with nano-multipod by thermal evaporation methods using metal catalysts. Cai et al. [29] reported that awl-like ZnO nanostructures have been fabricated by sublimation process employing chemical vapor deposition (CVD) method. However, these synthesis methods typically involve complex controlling process and too much energy, which possibly result in the increased cost and limitation of the potential applications. Therefore, the development of a facile, effective, and economical approach to synthesize ZnO and control of their morphology are strongly desirable. The most promising one was thermal decomposition or calcination of zinc carbonate and zinc carbonate hydroxide precursors.

The raw materials for this process are easily available and have a low-cost, superfine ZnO product which can be easily prepared by using this technique [30].

In this work, the porous ZnO microspheres constructed by multilayered porous nanosheets were obtained through a hydrothermal preparation and a thermal decomposition. The synthesized porous ZnO microspheres are assembled by numerous porous nanosheets. We investigated the effect of ZnO microsphere synthesis parameters. On the basis of the experimental results and analysis, the formation mechanism of the porous ZnO microspheres was pointed out. The prepared samples exhibited excellent sensing performance to ethanol gas, and the porous ZnO microspheres were promising candidates for the applications of ethanol sensitive material.

2. Experimental Section

2.1. Synthesis of ZnO Porous Microspheres. All chemicals used were of analytical grade from Shanghai Chemical Reagent Corporation and without further purification. ZnO porous microspheres constructed by multilayered porous nanosheets have been fabricated via hydrothermal method and a thermal decomposition. In a typical synthesis process, 3 mmol zinc nitrate hexahydrate ($\text{Zn}(\text{NO}_3)_2 \cdot 6\text{H}_2\text{O}$), 6 mmol urea ($\text{CO}(\text{NH}_2)_2$), and 0.5 mmol trisodium citrate were dissolved in 100 mL deionized water by a magnetic stirrer to form a mixed solution; the mixed solution was transferred into a 100 mL teflon-lined stainless steel autoclave and heated at 120°C for 6 h. The precipitate was collected by centrifugation and washed thoroughly with deionized water several times to remove the impurities and dried in a vacuum oven at 60°C for 12 h to obtain the ZHC precursors.

For the synthesis of porous ZnO microspheres, the as-obtained precursors were placed in a crucible and heated from room temperature to 500°C at a rate of 10°C/min and then maintained at 500°C for 2 h in air. After cooling to room temperature, the final product was collected.

2.2. Characterization. The phase structure and compositions of the as-fabricated products were identified by X-ray diffraction (XRD, Philips X'pert X-ray diffractometer with $\text{Cu-K}\alpha$ radiation, $\lambda = 1.5406 \text{ \AA}$) at 40 kV, 30 mA over the 2θ range 10–80°. Thermogravimetric (TG) and differential scanning calorimetry (DSC) analysis was measured by a thermogravimetric analyzer (NETZSCH STA 409 PC) with a heating temperature rate of 5°C min^{-1} under atmosphere from 50°C to 1000°C. The morphology and microstructure of the products were further investigated by scanning electron microscopy (SEM) using a JEOL JSM 6700F and transmission electron microscopy (TEM) using a JEOL JEM 2010F microscope working at 200 kV. The Brunauer-Emmett-Teller (BET) surface areas of the products were analyzed using a Micromeritics ASAP 2020 nitrogen adsorption apparatus.

2.3. Gas-Sensing Properties Test. For gas sensor experiments, the ZnO product was mixed with deionized water to form a paste and then coated onto an alumina tube-like substrate, on

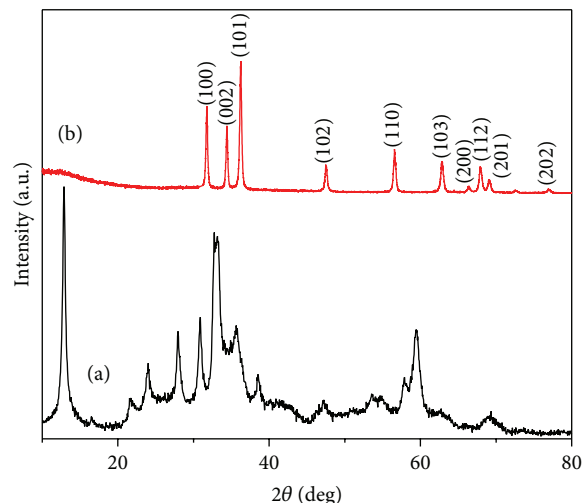


FIGURE 1: XRD pattern of (a) the ZnHC precursors and (b) ZnO obtained after being annealed at 500°C for 2 h.

which a pair of platinum wires had been installed. The ZnO coated substrate was dried under IR radiation in the air and then annealed at 500°C in air for 2 h. At last, a small Ni-Cr alloy coil was placed penetrating into the tube as a heater. The gas sensor was aged at 450°C in air for 10 days in order to improve the long-term stability and repeatability.

The gas-sensing properties of ZnO porous microspheres were tested using a WS-30A gas sensitivity system (Winsen Instruments Co., Zhengzhou, China). A certain concentration of target gas was injected into the evaporator in the sealed glass chamber separately and then mixed by starting the pair of air small-sized fans. The gas response value of testing gas was defined as the ratio of R_a to R_g , where R_a and R_g represent the resistance of the as-obtained ZnO measured in air and testing gas environment, respectively.

3. Results and Discussion

Figure 1 shows the XRD pattern of the ZHC precursors (Figure 1(a)). All the diffraction peaks in Figure 1(a) can be indexed as monoclinic zinc hydroxide carbonate $\text{Zn}_5(\text{OH})_6(\text{CO}_3)_2$ (JCPDS Card Number 11-0287). As shown in Figure 1(b), the diffraction peaks of ZnO porous microspheres correspond well with the (100), (002), (101), (102), (110), (103), (200), (112), (201), and (202) reflections of the hexagonal wurtzite structure of ZnO (space group P63mc, JCPDS Card Number 36-1451, $a = 3.25 \text{ \AA}$, $c = 5.207 \text{ \AA}$). No characteristic peaks of other impurities were detected in the XRD patterns, indicating that the porous ZnO microspheres had high purity and good crystallinity. That is to say, the ZHC precursors can be transformed utterly to a pure phase of hexagonal wurtzite type ZnO after being annealed at 500°C for 2 h.

The morphology and microstructure of the ZHC precursors and the ZnO microspheres were examined by SEM (Figure 2). Figure 2(a) shows the SEM image of an individual

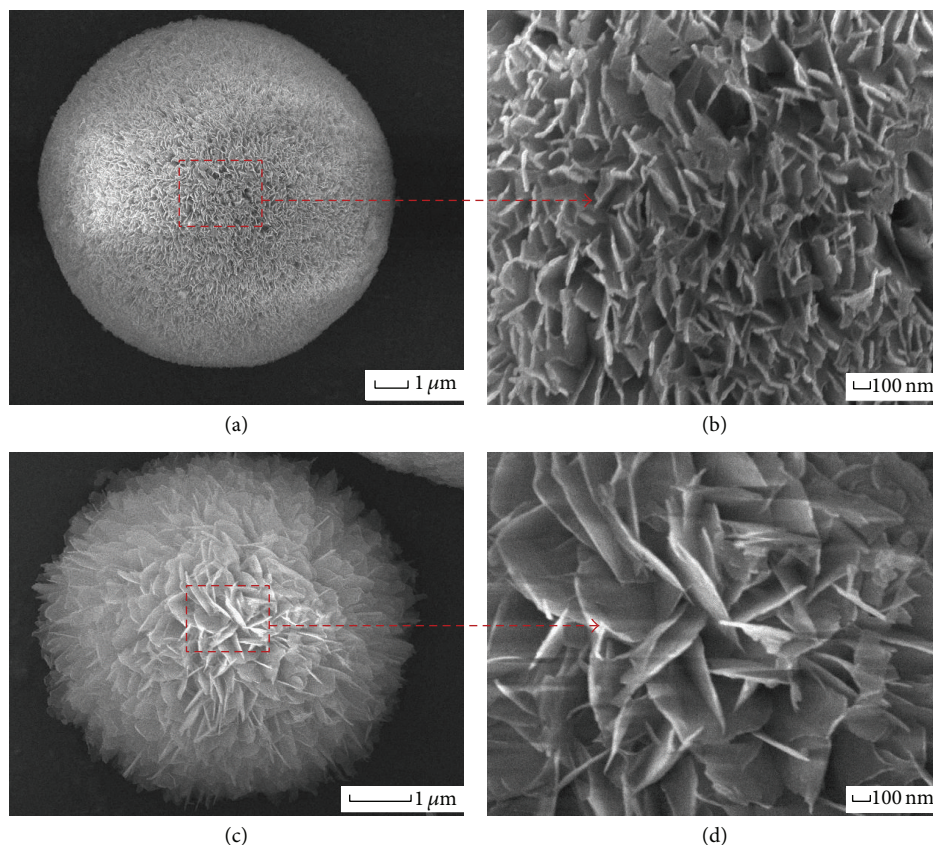


FIGURE 2: ((a) and (b)) SEM images of the ZHC precursors; ((c) and (d)) SEM images of ZnO porous microspheres obtained at 500°C for 2 h.

ZHC precursors microsphere. It demonstrates that the microsphere was assembled by many nanosheets, which are intercrossed with each other (Figure 2(b)). Figures 2(c) and 2(d) show the SEM images of ZnO microspheres, which calcined at 500°C in air for 2 h. Compared to the samples before calcination, the morphology and size of the calcined samples had no obvious change. It reveals that high-temperature calcining process did not destroy the 3D hierarchical structure, while the assembled structure becomes a little loose and the surface was rougher than uncalcined samples.

The porous ZnO nanosheets are further characterized by the TEM. Compared to the TEM images of ZHC precursors (Figure 3(a)), it can be seen that many pores of various sizes were observed on the surfaces of the nanosheets from the TEM images (Figures 3(b) and 3(c)) of ZnO nanosheets, due to the fact that the ZHC precursors were decomposed under the high temperature and then the water and carbon dioxide were volatilized. The porous ZnO microspheres, synthesized by hydrothermal method and a thermal decomposition, have large specific surface area and many active centers [31]. To obtain further information about the specific surface area and the pore sizes distribution of the as-prepared ZnO microspheres, nitrogen adsorption-desorption analysis was performed. As shown in Figure 3(d), the nitrogen adsorption-desorption isotherm belongs to type IV, indicating the existence of abundant mesopores in the ZnO microspheres. Using the BJH method and the desorption

branch of the nitrogen isotherm, the calculated pore-size distribution indicates that the material contains an average pore size of 25.288 nm. The specific surface area of the ZnO microspheres is calculated to be 29.87 m²/g by the BET equation. As-synthesized ZnO microspheres with a high special surface area may provide more surface active sites and pore-channels for gas sensing.

TG-DSC curves of the ZHC precursors were shown in Figure 4. It is obvious that TG curve of ZHC precursors contains two distinct weight loss steps. The weight loss in 50–200°C is 5.6 wt%, due to the endothermic loss of surface hydroxyls and water molecules in the precursors. The maximum weight loss occurring in the second step between 200 and 500°C is 22.1 wt% due to the volatilization of carbon dioxide. There is a strong endothermic peak at 257°C in the DSC curve, which corresponds with the second weight loss. There is no obvious weight loss on TG curve after 500°C, indicating the ZHC precursors were completely decomposed.

The SEM images of the ZnO samples at different reaction temperatures (120°C and 150°C) were shown in Figures 5(a) and 5(b). At 120°C, the samples had a spherical structure with diameter of about 3 μm (Figure 5(a)). When the reaction temperature increased to 150°C (Figure 5(b)), the samples had a spherical structure with diameter of approximately 6 μm. As raising the reaction temperature, the size of the ZnO microspheres increased. It was demonstrated that the decomposition rate of urea will be increased with increasing

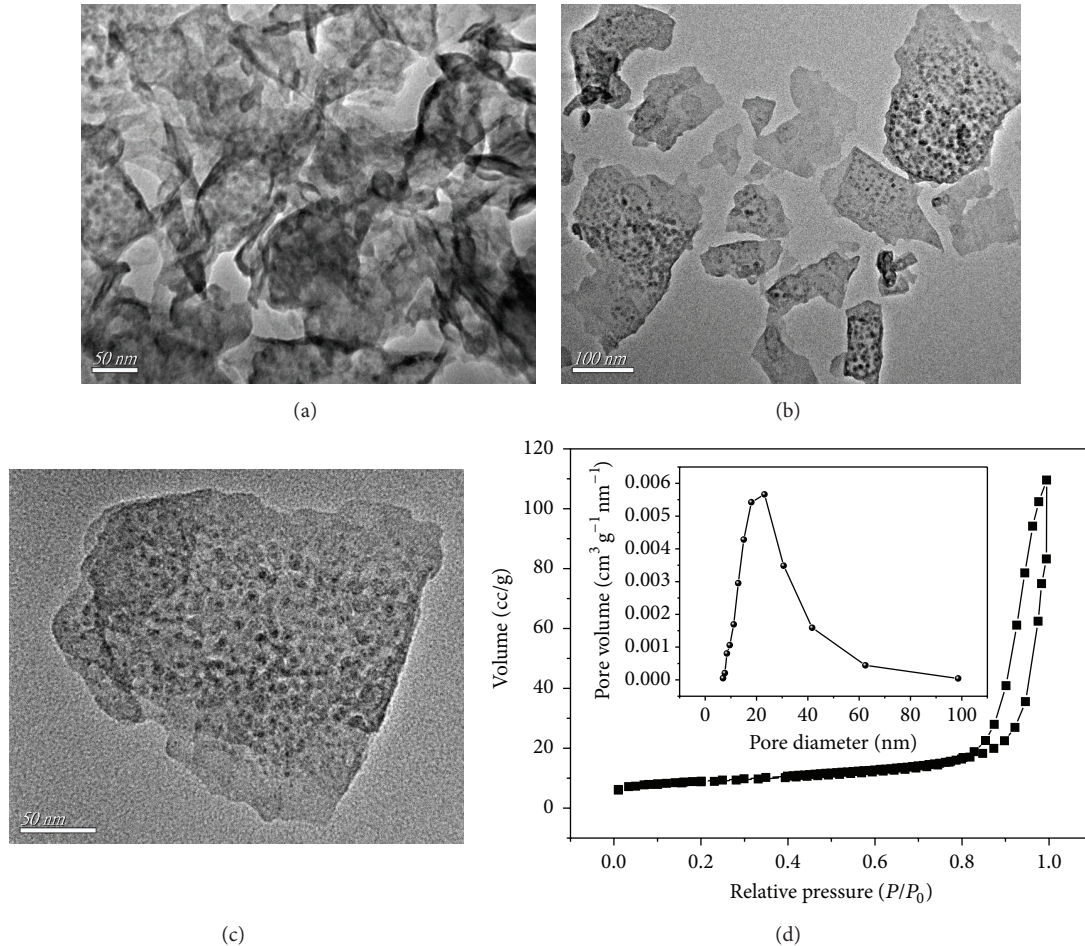


FIGURE 3: (a) TEM images of the ZHC precursors nanosheets; ((b) and (c)) TEM images of porous ZnO nanosheets; (d) N_2 adsorption-desorption isotherm and BJH pore size distribution plots (inset) of the porous ZnO product calcined ZHC precursors.

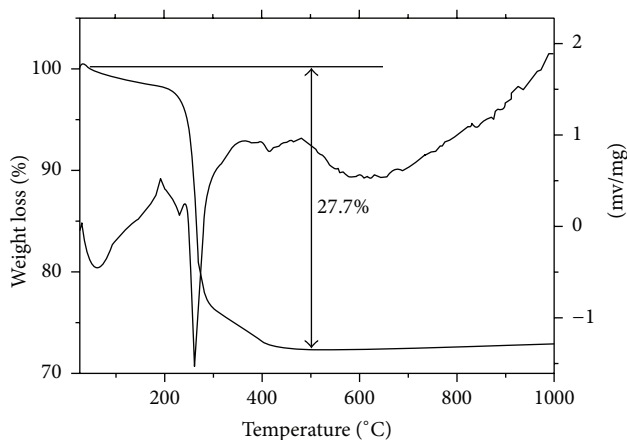


FIGURE 4: TG and DSC curves of the ZHC precursors.

reaction temperature. The amount of precipitation agent also increases in unit time promoting the nucleation and growth of grain. In order to understand the effects of reaction time on the sample structure, time-dependent experiments were

carried out at 120°C . Figures 5(c) and 5(d) show the SEM images of the samples synthesized at 120°C for different reaction time. As shown in Figure 5(c), the size of the ZnO microspheres is not homogeneous. While the reaction time is up to 3 h, it can be seen from Figure 5(d) that the ZnO microspheres are more regular and the size of sample is becoming more uniform. Thus, the ZnO microspheres tend to be uniform and regular when prolonging the reaction time.

The amount of trisodium citrate has an important influence on the sample structure. Different amounts of trisodium citrate (0, 0.5 mmol) were carried out in the experiments. The SEM images of the ZnO microspheres in the different conditions were shown in Figures 6(a) and 6(b). From Figure 6(a), it can be seen that the nanosheets aggregate irregularly and the size is bigger without trisodium citrate in the reaction. With increasing of trisodium citrate, the nanosheets become shorter and self-assemble into a spherical structure. It was demonstrated that trisodium citrate can inhibit the further growth of nanosheets and promote nanosheets assembly into a spherical structure.

Urea, as precipitant, plays an important role in the whole reaction. The SEM images of the ZnO microspheres were prepared by different amount of urea which were shown in

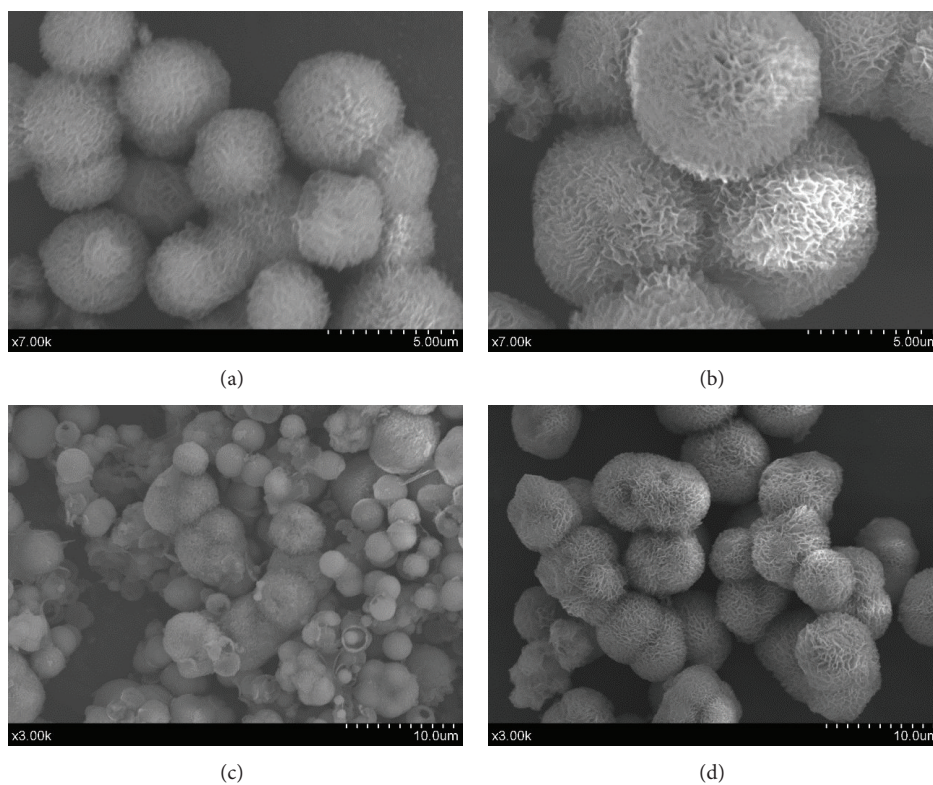


FIGURE 5: SEM images of the samples synthesized at different reaction times and temperatures: (a) 120°C; (b) 150°C; (c) 1 h; (d) 3 h.

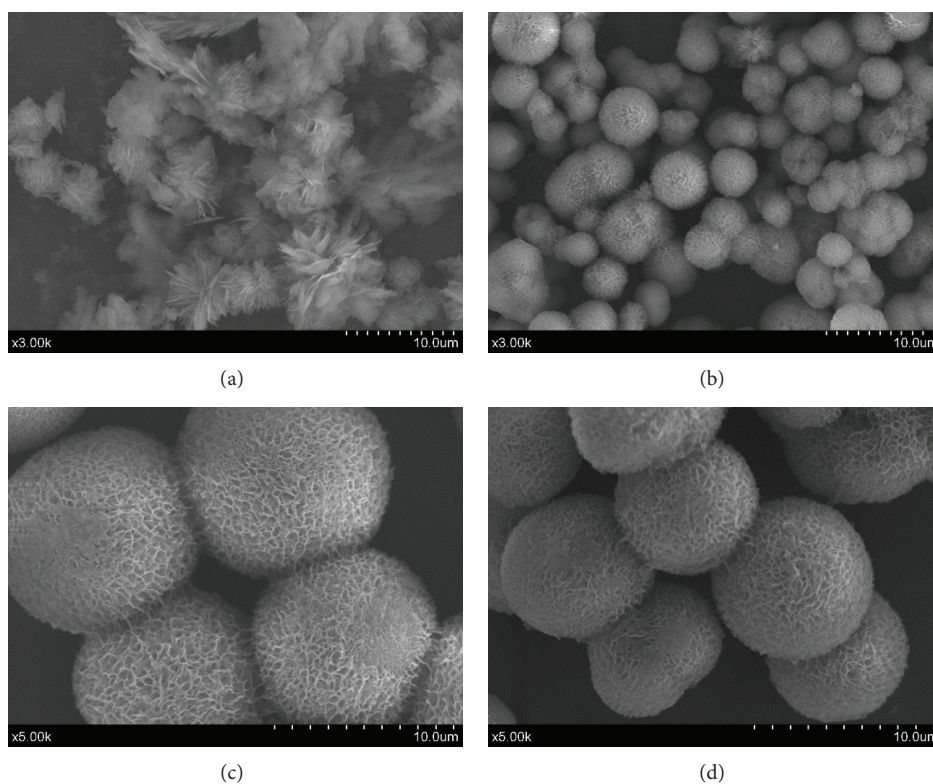


FIGURE 6: SEM images of the as-prepared ZnO microspheres synthesized under the different amount of trisodium citrate and urea: (a) 0 mmol trisodium citrate; (b) 0.5 mmol trisodium citrate; (c) 3 mmol urea; (d) 4 mmol urea.

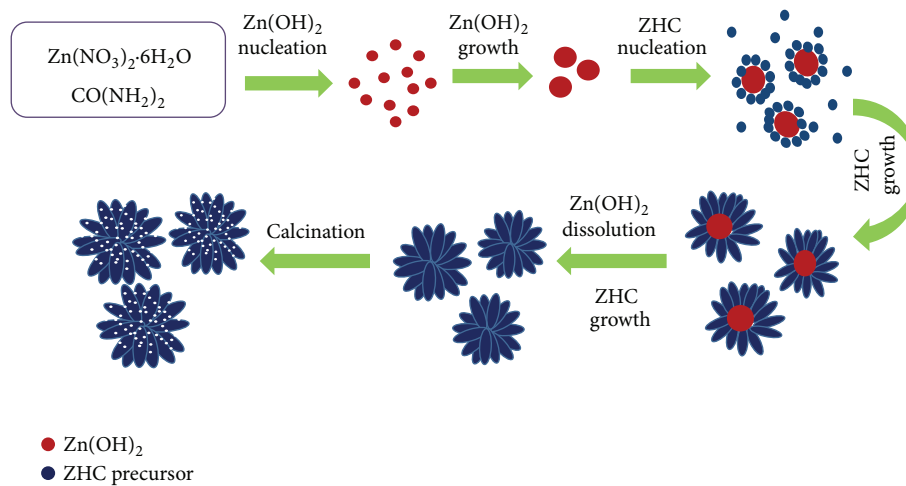
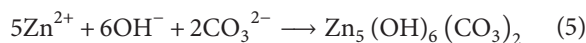
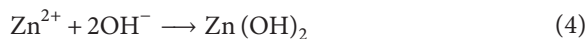
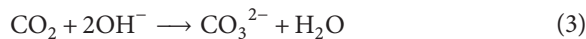


FIGURE 7: Schematic illustrations of growth mechanism of the porous ZnO microspheres.

Figures 6(c) and 6(d). When the amount of urea is 3 mmol, the samples had a spherical structure and relatively uniform sizes with diameter of about $8\ \mu\text{m}$. When the amount of urea increased to 4 mmol (Figure 6(d)), the samples had a spherical structure with diameter of approximately $6\ \mu\text{m}$. Compared with Figure 6(d), the size of the microspheres shown in Figure 6(c) becomes smaller, owing to the increasing of urea, and the reaction points of ZnO microspheres become more. Based on the above analysis, it can be seen that the amount of urea can affect the size of ZnO microspheres.

Based on the above experimental results and analysis, we proposed the growth mechanism of the porous ZnO microspheres. The formation mechanism was shown in Figure 7. In this formation process, trisodium citrate and urea were used as complexant and precipitant, respectively. The chemical reactions can be written as follows:



At the beginning of reaction, the solution is neutral. when the temperature exceeds 80°C , the urea begins to decompose, and then OH^- obtained from the reactions (1) and (2) will react with Zn^{2+} and generate $\text{Zn}(\text{OH})_2$ (reaction (4)). As the reaction proceeded, solution becomes saturated gradually, $\text{Zn}(\text{OH})_2$ starts to nucleate and then grows further into $\text{Zn}(\text{OH})_2$ spheres. According to the reaction (3), the

concentration of CO_3^{2-} in solution is increasing with the reaction proceeding, and then Zn^{2+} and OH^- react with CO_3^{2-} (reaction (5)) and generate ZHC precursor on the surface of $\text{Zn}(\text{OH})_2$ spheres. As the reaction progresses, the concentration of Zn^{2+} in the solution decreased, in order to supplement the Zn^{2+} , the $\text{Zn}(\text{OH})_2$ spheres begin to dissolve gradually, and then more and more nanosheets grow out from a crystal nucleus (reaction (6)) and finally assemble into the ZHC precursor spheres. The $\text{Zn}(\text{OH})_2$ spheres disappeared and ZHC precursor microspheres formed completely after 6 h.

In the process of the reaction, trisodium citrate as complexing agent has very important influence on the morphology of the samples. Citrate anion ($\text{C}_5\text{H}_7\text{O}_5\text{COO}^-$) and Zn^{2+} formed complex, hindering the reaction of Zn^{2+} , OH^- , and CO_3^{2-} , which slows down the formation velocity of ZHC precursor and controls the morphology of precursors. In addition, the citrate ions can be adsorbed on the surface of nanosheets effectively, limiting the horizontal and vertical growth of the nanosheets. Finally, the ZHC precursors were calcinated at 500°C for 2 h in the air condition, the porous ZnO microspheres were obtained, owing to the ZHC precursors decomposed in the calcination process, and then the water and carbon dioxide were volatilized (reaction (7)).

In the end, we tested the gas-sensing performances of the sensors based on the flower-like porous ZnO microspheres, which were synthesized by a simple hydrothermal method with zinc nitrate hexahydrate (3 mmol), urea (6 mmol), and trisodium citrate (0.5 mmol) as raw materials at 120°C for 6 h. In order to determine the optimal operating temperature, gas response of the sensors based on porous ZnO microspheres toward 50 ppm ethanol was investigated at different operating temperature, and the result is shown in Figure 8(a). It can be seen that the response to ethanol gas increased rapidly with the increase in operating temperature from 220 to 280°C and reached maximum at 280°C . After that, the response decreased with further increase in the operating temperature. Obviously, the optimal operating temperature

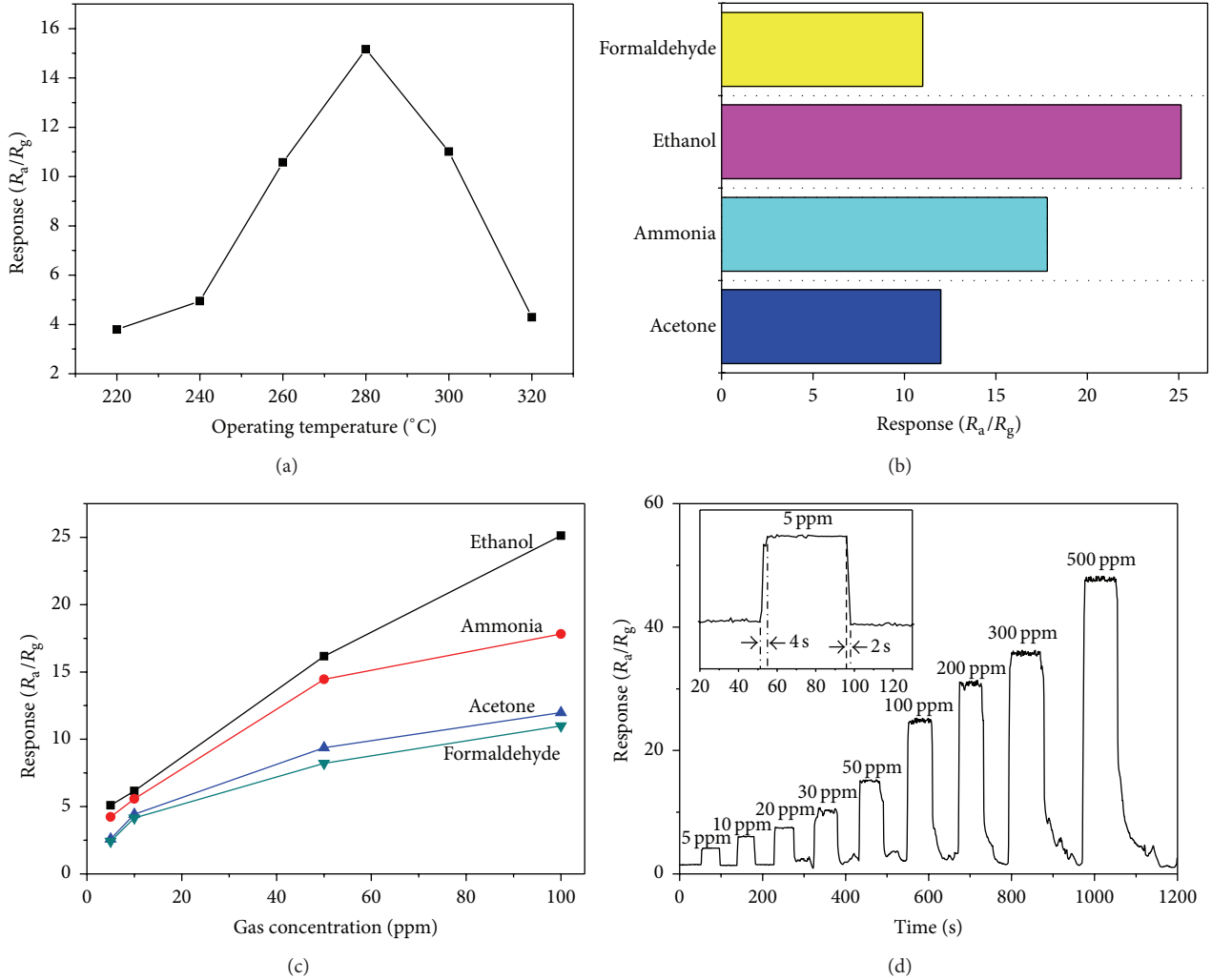
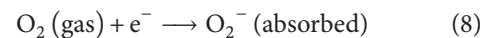


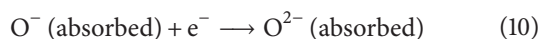
FIGURE 8: (a) Effect of operating temperature on the gas response of porous ZnO microspheres to 50 ppm ethanol gas. (b) Selectivity of porous ZnO microspheres to different testing gases. (c) Selectivity of ZnO microspheres versus testing gases concentration. (d) Response and recovery curves of porous ZnO microspheres upon exposure to ethanol gas.

of the sensors based on porous ZnO microspheres could be selected as 280 $^{\circ}\text{C}$. Figure 8(b) shows the responses of the as-prepared sensors to the various organic vapors, such as formaldehyde, ammonia, ethanol, and acetone with the concentration of 100 ppm at an operating temperature of 280 $^{\circ}\text{C}$. It is clearly found that the response of sensor to ethanol gas was highest among the test gases. Consequently, the sensor based on porous ZnO microspheres showed good selectivity toward ethanol compared to the other gases at the operating temperature of 280 $^{\circ}\text{C}$. The sensing properties of porous ZnO microspheres sensors to 5, 10, 50, and 100 ppm of formaldehyde, ammonia, ethanol, and acetone are measured at 280 $^{\circ}\text{C}$, as shown in Figure 8(c). The sensor has a larger value of response to ethanol but worse response to formaldehyde, ammonia, and acetone under the same concentration. These findings confirm the superior selectivity of porous ZnO microspheres sensors to ethanol. Figure 8(d) displays response and recovery curves of the ZnO sensors to ethanol gas with different concentrations (5 to 500 ppm) at

an operating temperature of 280 $^{\circ}\text{C}$. According to Figure 8(d), it can be observed that the sensor exhibits fast response and recovery times, and the sensitivity of porous ZnO to ethanol gases increased with the increasing of ethanol concentration. The response time and recovery time of the as-fabricated porous ZnO microspheres sensor for 5 ppm ethanol were 4 s and 2 s, respectively (inset of Figure 8(d)).

The gas-sensing mechanism of 3D porous ZnO microspheres can be explained by the surface charge model [32]. When exposed in different type of gases, resistance of semiconductor oxide materials alters. When the ZnO sensor is exposed in air, oxygen molecules in the atmosphere are absorbed on the surface of ZnO nanosheets by capturing free electrons from the conduction band, generating oxygen ions, such as O_2^- , O^- , and O^{2-} [1, 33], leading to the electron concentration of the conduction band decreasing and the resistance of ZnO sensor increasing. The surface reactions can be described as follows:





When ZnO is exposed to the ethanol gas, the ethanol molecules will react with the adsorbed oxygen ions on the surface and release the electrons back to the conduction band. This results in the electron concentration increasing and as a consequence the resistance of the materials decreases. The chemical reactions can be written as follows:



When increasing the concentration of ethanol, more and more electrons were released back to the conduction band, leading to the resistance of sensors decreasing. That is why the sensitivity of porous ZnO to ethanol gases increased with the increasing of ethanol concentration.

Moreover, the reasons for the superior gas-sensing properties of porous ZnO microspheres were possibly attributed to the abundant pores increasing the specific surface areas. It was well known that large specific surface areas provided more active sites and promoted gas diffusion. Thus, the porous ZnO microspheres were promising candidates for gas-sensing applications, especially for the detection of ethanol.

4. Conclusions

In summary, the porous ZnO microspheres have been successfully synthesized by calcining the ZHC precursor microsphere, which were the reaction products of a hydrothermal reaction by zinc nitrate hexahydrate and urea in the presence of trisodium citrate. The porous ZnO microspheres are assembled by numerous porous nanosheets. The approach provided a simple, effective, low-cost, and environment friendly method to largely synthesize the porous ZnO microspheres. Furthermore, the formation mechanism of the porous ZnO microspheres was speculated by the experimental results and analysis. The gas-sensing properties test indicated that the ZnO gas sensors exhibit excellent sensing performances to ethanol, owing to their large specific surface area and outstanding gas-sensing properties. The porous ZnO microspheres were promising candidates for the applications of ethanol sensitive material.

Conflict of Interests

The authors declare that there is no conflict of interests regarding the publication of this paper.

Acknowledgments

This work is supported by the National Natural Science Foundation of China (nos. 51372103 and 51202092), the

special grade of the financial support from China Postdoctoral Science Foundation (2014T70485), and the China Postdoctoral Science Foundation (2013M531285).

References

- [1] L. L. Wang, H. M. Dou, F. Li, J. N. Deng, Z. Lou, and T. Zhang, "Controllable and enhanced HCHO sensing performances of different-shelled ZnO hollow microspheres," *Sensors and Actuators B: Chemical*, vol. 183, pp. 467–473, 2013.
- [2] C.-T. Lee and T.-J. Wu, "Light distribution and light extraction improvement mechanisms of remote GaN-based white light-emitting-diodes using ZnO nanorod array," *Journal of Luminescence*, vol. 137, pp. 143–147, 2013.
- [3] C. T. Pan, Y. C. Chen, C. C. Hsieh et al., "Ultrasonic sensing device with ZnO piezoelectric nanorods by selectively electro-spraying method," *Sensors and Actuators A: Physical*, vol. 216, pp. 318–327, 2014.
- [4] N. Uekawa, T. Saito, T. Kojima, and K. Kakegawa, "Control of orientation and electrical conductivity of doped ZnO films using a layered double hydroxide nanoparticle precursor and spark plasma sintering process," *Scripta Materialia*, vol. 69, no. 2, pp. 131–134, 2013.
- [5] J. R. Huang, H. B. Ren, P. P. Sun, C. P. Gu, Y. F. Sun, and J. H. Liu, "Facile synthesis of porous ZnO nanowires consisting of ordered nanocrystallites and their enhanced gas-sensing property," *Sensors and Actuators B: Chemical*, vol. 188, pp. 249–256, 2013.
- [6] X. H. Zhao, F. J. Lou, M. Li, X. D. Lou, Z. Z. Li, and J. G. Zhou, "Sol-gel-based hydrothermal method for the synthesis of 3D flower-like ZnO microstructures composed of nanosheets for photocatalytic applications," *Ceramics International*, vol. 40, no. 4, pp. 5507–5514, 2014.
- [7] S. J. Pearton and F. Ren, "Advances in ZnO-based materials for light emitting diodes," *Current Opinion in Chemical Engineering*, vol. 3, pp. 51–55, 2014.
- [8] D. Y. Jiang, J. Y. Zhang, Y. M. Lu et al., "Ultraviolet Schottky detector based on epitaxial ZnO thin film," *Solid-State Electronics*, vol. 52, no. 5, pp. 679–682, 2008.
- [9] S. S. Ma, R. Li, C. P. Lv, W. Xu, and X. L. Gou, "Facile synthesis of ZnO nanorod arrays and hierarchical nanostructures for photocatalysis and gas sensor applications," *Journal of Hazardous Materials*, vol. 192, no. 2, pp. 730–740, 2011.
- [10] B.-H. Lee and S.-M. Kang, "Properties of ZnO varistor blocks under multiple lightning impulse voltages," *Current Applied Physics*, vol. 6, no. 5, pp. 844–851, 2006.
- [11] M. Raja, N. Muthukumarasamy, D. Velauthapillai, R. Balasundaraprabhu, S. Agilan, and T. S. Senthil, "Studies on bundle like ZnO nanorods for solar cell applications," *Solar Energy*, vol. 106, pp. 129–135, 2014.
- [12] R. Murugan, T. Woods, P. Fleming, D. Sullivan, S. Ramakrishna, and P. R. Babu, "Synthesis and photocatalytic application of ZnO nanoarrows," *Materials Letters*, vol. 128, pp. 404–407, 2014.
- [13] Q. Hou, L. Q. Zhu, H. N. Chen, H. C. Liu, and W. P. Li, "Growth of flower-like porous ZnO nanosheets by electrodeposition with $\text{Zn}_5(\text{OH})_8(\text{NO}_3)_2 \cdot 2\text{H}_2\text{O}$ as precursor," *Electrochimica Acta*, vol. 78, pp. 55–64, 2012.
- [14] C.-F. Li, C.-Y. Hsu, and Y.-Y. Li, " NH_3 sensing properties of ZnO thin films prepared via sol-gel method," *Journal of Alloys and Compounds*, vol. 606, pp. 27–31, 2014.

- [15] G. C. Qi, S. Z. Zhao, and Z. H. Yuan, "From function-guided assembly of a lotus leaf-like ZnO nanostructure to a formaldehyde gas-sensing application," *Sensors and Actuators B: Chemical*, vol. 184, pp. 143–149, 2013.
- [16] Y. Zeng, L. Qiao, Y. F. Bing et al., "Development of microstructure CO sensor based on hierarchically porous ZnO nanosheet thin films," *Sensors and Actuators B: Chemical*, vol. 173, pp. 897–902, 2012.
- [17] A. Mortezaali and R. Moradi, "The correlation between the substrate temperature and morphological ZnO nanostructures for H₂S gas sensors," *Sensors and Actuators A: Physical*, vol. 206, pp. 30–34, 2014.
- [18] S. H. Wei, S. M. Wang, Y. Zhang, and M. H. Zhou, "Different morphologies of ZnO and their ethanol sensing property," *Sensors and Actuators B: Chemical*, vol. 192, pp. 480–487, 2014.
- [19] C.-J. Chang, C.-Y. Lin, J.-K. Chen, and M.-H. Hsu, "Ce-doped ZnO nanorods based low operation temperature NO₂ gas sensors," *Ceramics International*, vol. 40, no. 7, pp. 10867–10875, 2014.
- [20] M. S. Samuel, J. Koshy, A. Chandran, and K. C. George, "Electrical charge transport and dielectric response in ZnO nanotubes," *Current Applied Physics*, vol. 11, no. 4, pp. 1094–1099, 2011.
- [21] M. Raja, N. Muthukumarasamy, D. Velauthapillai, and R. Balasundaraprabhu, "Influence of copper on the morphology and properties of one dimensional ZnO nanorod structures," *Superlattices and Microstructures*, vol. 72, pp. 102–110, 2014.
- [22] G. Meng, X. D. Fang, W. W. Dong et al., "One step synthesis of vertically aligned ZnO nanowire arrays with tunable length," *Applied Surface Science*, vol. 256, no. 22, pp. 6543–6549, 2010.
- [23] R. Zhang, M. Hummelgård, and H. Olin, "A facile one-step method for synthesising a parallelogram-shaped single-crystalline ZnO nanosheet," *Materials Science and Engineering B*, vol. 184, no. 1, pp. 1–6, 2014.
- [24] J. Karamdel, C. F. Dee, and B. Y. Majlis, "Characterization and aging effect study of nitrogen-doped ZnO nanofilm," *Applied Surface Science*, vol. 256, no. 21, pp. 6164–6167, 2010.
- [25] C. P. Gu, J. R. Huang, Y. J. Wu, M. H. Zhai, Y. F. Sun, and J. H. Liu, "Preparation of porous flower-like ZnO nanostructures and their gas-sensing property," *Journal of Alloys and Compounds*, vol. 509, no. 13, pp. 4499–4504, 2011.
- [26] B. X. Li and Y. F. Wang, "Hierarchically assembled porous ZnO microstructures and applications in a gas sensor," *Superlattices and Microstructures*, vol. 49, no. 4, pp. 433–440, 2011.
- [27] F. B. Gu, D. You, Z. H. Wang, D. M. Han, and G. S. Guo, "Improvement of gas-sensing property by defect engineering in microwave-assisted synthesized 3D ZnO nanostructures," *Sensors and Actuators B: Chemical*, vol. 204, pp. 342–350, 2014.
- [28] C. Li, G. J. Fang, W. J. Guan, and X. Z. Zhao, "Multipod ZnO 3D microstructures," *Materials Letters*, vol. 61, no. 14–15, pp. 3310–3313, 2007.
- [29] X. L. Cai, F. X. Wang, D. W. Yan, Z. M. Zhu, and X. F. Gu, "Luminescence characteristics and growth mechanism of awl-like ZnO Nanostructures fabricated on Ni-coated silicon substrate via chemical vapor deposition method," *Ceramics International*, vol. 40, no. 8, pp. 12293–12298, 2014.
- [30] M. Shamsipur, S. M. Pourmortazavi, S. S. Hajimirsadeghi, M. M. Zahedi, and M. Rahimi-Nasrabadi, "Facile synthesis of zinc carbonate and zinc oxide nanoparticles via direct carbonation and thermal decomposition," *Ceramics International*, vol. 39, no. 1, pp. 819–827, 2014.
- [31] C. L. Shao, L. Tu, A. Yu, B. Li, and X. F. Zhou, "From Zn₄(CO₃)(OH)₆·H₂O curling nanopetals to ZnO stretching porous nanosheets: growth mechanism and gas sensing property," *Thin Solid Films*, vol. 525, pp. 148–153, 2012.
- [32] W. W. Guo, T. N. Liu, J. X. Wang et al., "Hierarchical ZnO porous microspheres and their gas-sensing properties," *Ceramics International*, vol. 39, no. 5, pp. 5919–5924, 2013.
- [33] J. S. Cui, J. B. Sun, X. Liu, J. W. Li, X. Z. Ma, and T. T. Chen, "Fabrication of hierarchical flower-like porous ZnO nanostructures from layered ZnC₂O₄·3Zn(OH)₂ and gas sensing properties," *Applied Surface Science*, vol. 308, pp. 17–23, 2014.

Research Article

Rapid and Sensitive Detection of Lung Cancer Biomarker Using Nanoporous Biosensor Based on Localized Surface Plasmon Resonance Coupled with Interferometry

Jae-Sung Lee,¹ Sae-Wan Kim,¹ Eun-Yoon Jang,² Byoung-Ho Kang,³ Sang-Won Lee,¹ Gopalan Sai-Anand,¹ Seung-Ha Lee,⁴ Dae-Hyuk Kwon,⁵ and Shin-Won Kang¹

¹School of Electronics Engineering, College of IT Engineering, Kyungpook National University, Daegu 702-701, Republic of Korea

²Gyeongbuk Institute of IT Convergence Industry Technology, Gyeongsangbuk-do 712-832, Republic of Korea

³Center for Functional Devices Fusion Platform, Kyungpook National University, Daegu 702-701, Republic of Korea

⁴Department of Biomedical, School of Medicine, Dankook University, Chungnam 330-714, Republic of Korea

⁵Department of Electronics Engineering, Kyungil University, Gyeongsangbuk-do 712-702, Republic of Korea

Correspondence should be addressed to Shin-Won Kang; swkang@knu.ac.kr

Received 22 May 2015; Accepted 15 July 2015

Academic Editor: Anh-Tuan Le

Copyright © 2015 Jae-Sung Lee et al. This is an open access article distributed under the Creative Commons Attribution License, which permits unrestricted use, distribution, and reproduction in any medium, provided the original work is properly cited.

We propose a nanobiosensor to evaluate a lung cancer-specific biomarker. The nanobiosensor is based on an anodic aluminum oxide (AAO) chip and functions on the principles of localized surface plasmon resonance (LSPR) and interferometry. The pore-depth of the fabricated nanoporous AAO chip was $1\ \mu\text{m}$ and was obtained using a two-step electrochemical anodization process. The sensor chip is sensitive to the refractive index (RI) changes of the surrounding medium and also provides simple and label-free detection when specific antibodies are immobilized on the gold-deposited surface of the AAO chip. In order to confirm the effectiveness of the sensor, the antibodies were immobilized on the surface of the AAO chip, and the lung cancer-specific biomarker was applied atop of the immobilized-antibody layer using the self-assembled monolayer method. The nanoporous AAO chip was used as a sensor system to detect serum amyloid A1, which is a lung cancer-specific biomarker. The specific reaction of the antigen-antibody contributes to the change in the RI. This in turn causes a shift in the resonance spectrum in the refractive interference pattern. The limit of detection (LOD) was found to be $100\ \text{ag/mL}$ and the biosensor had high sensitivity over a wide concentration range.

1. Introduction

Highly sensitive and rapid detection of biomarkers is essential for biosensors used in medical diagnostics, genetics, or environmental monitoring applications [1, 2]. Nanotechnology based biosensor devices have the potential to overcome many of the disadvantages of conventional health diagnostic and monitoring methods. Among various nanotechnology based biosensors, electrochemical nanoscale biosensors offer the ability to measure biomedical parameters directly and rapidly, without using fluorescent labels. Nanoscale sensors also offer the potential for *in vivo* sensing.

The development of ultrasensitive sensing and biosensing devices using nanomaterials and nanostructures received a

great deal of attention in the last decade, primarily because of their unique physical and chemical properties. Nanobiosensors, in particular, are analytical devices that utilize nanoscale detector components to identify minute biological elements with enhanced sensitivity [3]. These biosensors are important in the field of biotechnology because of their direct, faster, more accurate, and more selective detection of the analyte at low concentrations [4, 5].

Recently, considerable research has been carried out to develop nanobiosensors using nanostructures, such as nanofibers, nanoparticles, nanowires, nanorods, and nanotubes. These nanostructures are important in the manufacturing of the biosensor because of their unique electronic, optical, magnetic, thermoelectrical, and chemical properties [6–9].

The nanostructures in these biosensors are highly selective and sensitive; hence, they are used for medical diagnosis, monitoring of diseases, drug discovery, and the detection of environmentally relevant biological agents [10].

The combination of nanostructures and biomolecules is of considerable interest in the field of nanobiotechnology. Fundamentally, biosensors are based on the coupling of a ligand-receptor binding reaction to a signal transducer [11]. Several techniques for the detection of biomolecules based on the ligand-receptor binding reaction have been reported. These include techniques, such as optical sensors using light [12, 13], semiconductor sensors using changes in electric properties due to an external stimulus, and chemical sensors using chemical changes [14, 15]. Although each of these techniques has its individual strengths and weaknesses, a strong case has been made that the optical type biosensors have greater potential. In particular, techniques that are based on localized surface plasmon resonance (LSPR) on gold-deposited nanostructures are fast becoming the methods of choice in many affinity biosensing applications [16, 17]. LSPR has been used to monitor a broad range of analyte-surface binding interactions, including the adsorption of small molecules, ligand-receptor binding, protein adsorption on self-assembled monolayers (SAMs), antibody-antigen binding, and protein-DNA interactions [18, 19].

All of these properties make anodic aluminum oxide (AAO) an excellent sensing platform with exciting opportunities in the development of advanced, simple, smart, and cost-effective sensing devices that may be used in numerous analytical applications. In addition, AAO chip has a unique set of chemical, optical, mechanical and electrical properties. These properties include chemical resistance, thermal stability, biocompatibility, and a large surface area. The AAO chips can be synthesized via anodization of metal aluminum. Using this procedure, precise control of the pore diameter and length can be achieved [20]. Owing to these fairly well-defined nanopores, AAO chips have been used in popular applications in many areas, such as nanostructured-material preparation and biological and chemical separations [21, 22]. The use of AAO in these for applications has a lot of potential in future developments and in the translation of these research products into commercial devices.

In our previous work, we confirmed that AAO chips can be used to detect biomolecules [23, 24]. Furthermore, we successfully fabricated a biosensor where the controlled pore-depth and a uniform surface could be retained. The AAO chip responses were evaluated by the surface RI changes through the interaction between the interference and LSPR.

In this study, we describe major advances and developments in the lung cancer-specific biomarker sensor system based on a nanoporous AAO chip. The lung cancer-specific biomarker of choice was serum amyloid A1 (SAA1). Herein, we will briefly describe the nanoporous structures of AAO prepared at 1 μm of pore-depth, various pore diameters, ranging from 15 nm to 95 nm, using a two-step electrochemical anodization procedure. We also describe their key optical and electrochemical properties, which make AAO ideal for specific sensing applications. The pore diameters of the AAO

chip were tuned using a pore-widening treatment as a function of the anodization conditions. The sensor chip is sensitive to the refractive index (RI) of the surrounding medium and also provides simple and label-free detection when specific antibodies are immobilized to the gold-deposited surface of AAO chip. The specific antigen-antibody reaction contributes to the change in the RI that causes a shift in the resonance spectrum of the refractive interference pattern. The results indicate that the pore size has to be large enough to allow biomolecules to enter the pores freely, but small enough to retain the optical reflectivity of the AAO membrane. The limit of detection (LOD) of our sensor system for SAA1 was at a concentration of 100 ag/mL. Our proposed AAO chip has high sensitivity and real-time detection of biomolecular interactions. These properties allow these biosensors to be applied in a wide array of applications.

2. Experimental Section

2.1. Materials. Aluminum sheet, perchloric acid, ethanol, oxalic acid, phosphoric acid, chromic acid, 11-mercapto-1-undecanol acid, N-(3-dimethylaminopropyl)-N'-ethylcarbodiimide hydrochloride (EDC), N-hydroxysuccinimide (NHS), and dimethyl sulfoxide (DMSO) were supplied by Sigma-Aldrich (USA). Buffer solution of Tris-HCl (pH 7.4) (WELGENE Inc. Korea) was used.

2.2. Serum Amyloid A (SAA). SAA is a high density lipoprotein- (HDL-) associated apolipoprotein and is known to play a major role in the modulation of inflammation and in the metabolism and transport of cholesterol [25]. It has been recently proposed that SAA is a potentially useful biomarker to monitor patients harboring human tumors, including gastric and nasopharyngeal cancer [26, 27]. Moreover, in lung cancer patients, using mass spectrometry and proteomic technologies, the SAA was identified as the top differentially expressed protein that was able to differentiate the serum of patients from the serum of healthy individuals. Among four human SAA gene families, the acute SAAs, SAA1 and SAA2, are known to be induced up to several hundredfold. SAA3 is a pseudogene whereas the SAA4 is constantly expressed [28, 29]. In the present report, we propose that SAA1 is a good serum biomarker for the detection of lung cancer.

2.3. Principle of Sensor Operation and Structure. In order to increase the sensitivity of the sensor system, we developed a sensor chip designed to detect the SAA1 antigen (ProtanBio, Korea) using both interferometry and LSPR. Gold was deposited on a nanoporous structure to induce LSPR and to allow immobilization of a SAA1 antibody (100 $\mu\text{g/mL}$, ProtanBio, Korea). When the light is vertically incident, the interference fringe pattern appears as the difference in optical path between the upper part of the gold-deposited nanostructure and the lower part of the core. The reaction of the SAA1 antigen with the SAA1 antibody using the SAM method causes a change in the wavelength-dependent refractive index of the sensing membrane. The wavelength shift and the change in reflectance intensity are caused by

TABLE 1: Parameters for fabrication of various pore diameters of AAO chip.

Sample	Electrolyte	Anodization voltage (V)	2nd anodization time
(a)	0.3 M oxalic acid	20	50
(b)	0.3 M oxalic acid	40	16
(c)	0.4 M oxalic acid	50	7
(d)	0.1 M phosphoric acid	50	190
(e)	1 M phosphoric acid	50	60

the interference. Thus, the target material is measured by the effective optical thickness (L) of the detection membrane and spectrum change in reflection light from RI.

Effective L was demonstrated by [30] to be the multiple of RI and thickness by the following equation:

$$\begin{aligned} m\lambda_1 &= 2n_{\lambda_1}L, \\ (m+1)\lambda_2 &= 2n_{\lambda_2}L. \end{aligned} \quad (1)$$

Here, m is the order of interference meaning optical path length difference and phase shift of reflection light; λ is the wavelength of light; n_{λ} is the effective RI at the wavelength λ [30]. λ_1 and λ_2 show interference neighboring waves of orders m and $m+1$, respectively. Because the band gap of the AAO membrane is large n_{λ} it can be expressed as a constant at long wavelength bandwidth. Thus, the relationship between fringe order m , λ_1 , and λ_2 can be given by the following equation:

$$\frac{\lambda_1}{\lambda_2} = \frac{(m+1)}{m}. \quad (2)$$

To enhance the sensors sensitivity, several research groups focused on nanoscale optical sensors using nanostructures and nanoparticles. Thus, the proposed LSPR-based biosensor depends on the shape and size of gold nanostructure deposited on the AAO membrane. The LSPR phenomenon can be understood using the RI response model of propagation surface plasmon on a metal surface [31]:

$$\Delta\lambda_{\max} = m\Delta n \left[1 - e^{(-2d/l_d)} \right]. \quad (3)$$

Here, $\Delta\lambda_{\max}$ is the wavelength shift, m is the refractive sensitivity, Δn is the change in the RI by optical adsorption, d is the effective thickness of the adsorption surface, and l_d is the characteristic electromagnetic field decay length. As shown in (1), the RI and L of detection membrane are changed when the analyte on the surface of metal structure is detected by the antigen-antibody reaction. In addition, based on (3), extremely small changes such as the change in the RI of the surrounding media can be detected using LSPR by the antigen-antibody reaction. In the present report, the proposed sensing system causes a significant change in sensitivity, as observed by both optical LSPR and interferometry. A schematic diagram of the fabricated AAO chip and the optical detection method is shown in Figure 1.

2.4. Fabrication of AAO Chip. AAO chip can be obtained using a two-step anodization process of the aluminum sheet

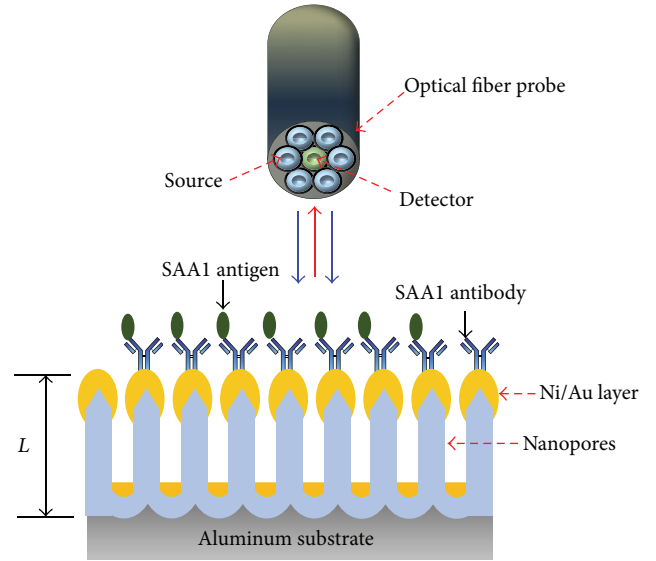


FIGURE 1: Schematic diagram of the fabricated AAO chip and the optical detection method.

that was anodized using electrolytes [32]. In order to obtain various diameters of the pore, the AAO chip was controlled by changing the anodization conditions, such as the applied voltage, the anodization time, and the types of electrolyte acids. The composition of the parameters for fabrication of nanoporous AAO chip is given in Table 1. Initially, the aluminum sheet was placed in a mixed solution of 70% perchloric acid and 30% ethanol and a voltage of 20 V was applied to remove impurities, the native oxide layer, and to smoothen the surface of the aluminum sheet. Second, to generate the oxide layer, the aluminum sheet was cleaned and was placed in a different electrolyte acid (0.3, 0.4 M oxalic acid and 0.1, 1 M phosphoric acid) and applied with a bias for each different voltage setting for 30 min. The anodization process was maintained at 9°C in a circulator system. Third, to remove the first AAO layer, the aluminum sheet was placed in a solution that consisted of 6 wt% phosphoric acid and 1.8 wt% chromic acid for 90 min at 60°C. Finally, the second anodization process was performed using the same conditions as in the first anodization.

The AAO chip was fabricated with different diameters of the pore by controlling the anodization conditions. We measured the pore diameter and surface uniformity using

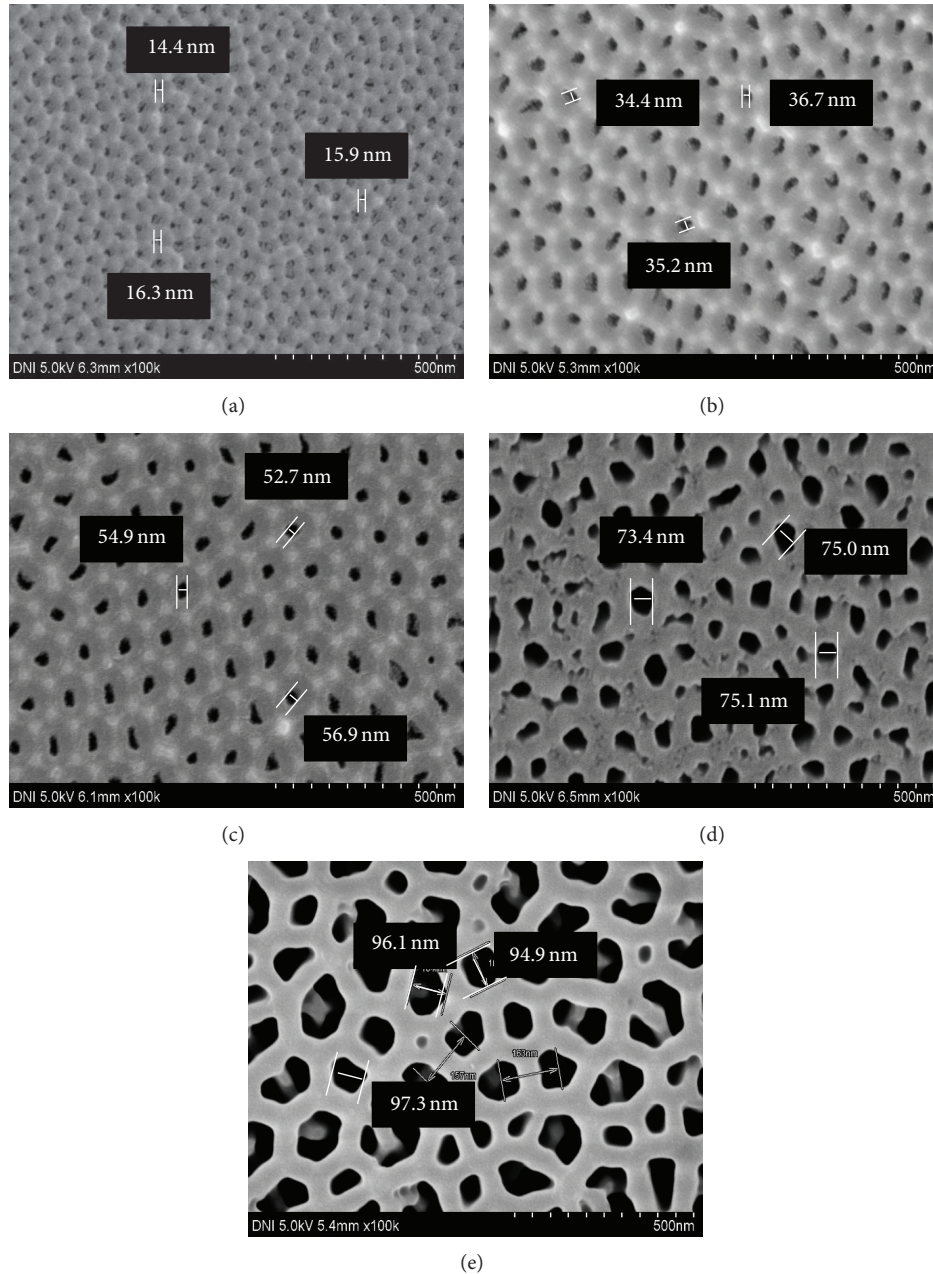


FIGURE 2: SEM image of fabricated various pore diameters of AAO chip: (a) 15 nm, (b) 35 nm, (c) 55 nm, (d) 75 nm, and (e) 95 nm pore diameters.

scanning electron microscopy (SEM; Hitachi S-4800) as a structural diagnostic technique. A SEM image of the fabricated AAO chip is shown in Figure 2. The results indicate that the five different pore diameters of AAO (15, 35, 55, 75, and 95 nm) depended on the type of the anodizing method used. The pore-depth of the fabricated AAO chips was standardized at $1\ \mu\text{m}$ in Figure 3. The pore-depth exhibited the best sensitivity at $1\ \mu\text{m}$ thickness because the changes in the effective L became larger as the pore-depth decreased [23]. We also found that when the fabrication of the AAO chip's pore-depth was less than $1\ \mu\text{m}$ the surface uniformity was compromised.

2.5. Fabrication of the Sensing Membrane. Deposition of gold on the nanostructure has an important role in the induction of LSPR and immobilization of the antibodies on the surface of biocompatible materials. In order to fabricate the sensing membrane, an electron-beam evaporator was used to deposit nickel and gold with thicknesses of 5 nm and 15 nm, respectively. The evaporator was operated using a pressure setting of 4.0×10^{-6} torr and a speed of $0.1\ \text{\AA}/\text{sec}$. Both gold and silver adhered to nickel and were reported to show improved SPR phenomenon when compared to pure gold and silver [33]. Therefore, by depositing the nickel, we successfully obtained the gold deposited onto AAO membrane.

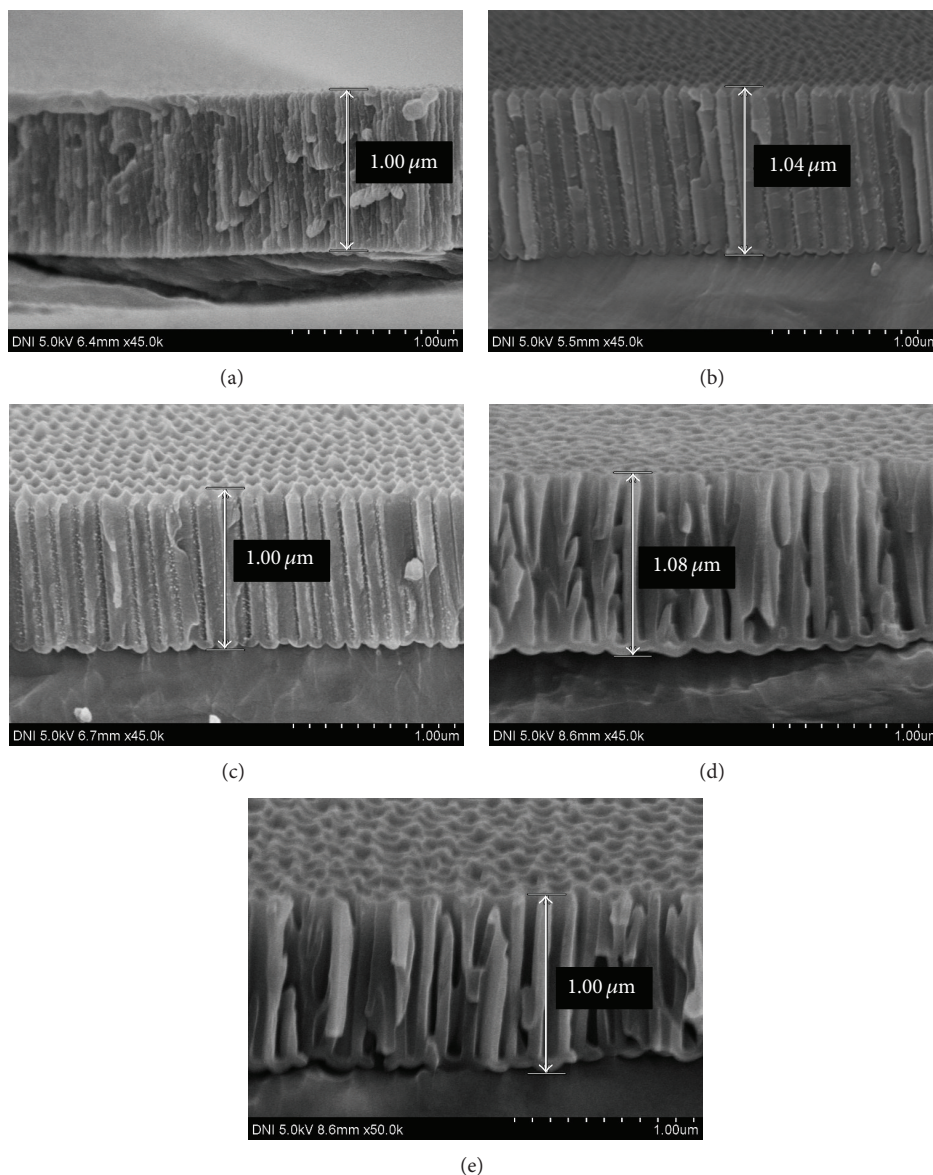


FIGURE 3: SEM image of a pore-depth of an AAO template with various pore diameters: (a) 15 nm, (b) 35 nm, (c) 55 nm, (d) 75 nm, and (e) 95 nm pore diameters.

After deposition, alkanethiol SAM was used to immobilize the antibody to the sensing membrane that has strong surface affinity to gold, silver, and copper. One advantage of this procedure is the relatively easy fabrication and the fact that gold, silver, and copper have extremely high affinity to biomaterials. Therefore, the gold deposited AAO chip was immersed in a solution of 11-mercapto-1-undecanol acid in ethanol and incubated for 24 h [34]. The strong bonding between the gold surface and thiol occurs in the buffer solution, and SAM is completed using a high carboxylic functional group. In order to help bonding of the SAM with carboxyl functional groups and the SAA1 antibody, N-(3-dimethylaminopropyl)-N'-ethylcarbodiimide hydrochloride (EDC) and N-hydroxysuccinimide (NHS) were prepared in distilled water and dimethyl sulfoxide (DMSO) mixed at

identical ratio at concentrations of 200 mM and 50 mM, respectively. The mixed solution was stirred for 1 h until the sensing membrane with SAM was formed. Finally, the SAA1 antibody (100 μg/mL) was stirred for 1 h to finish the sensing membrane of the AAO chip. The nonspecific binding of antibody was washed out using a buffer solution of Tris-HCl (pH 7.4). The schematic diagram for SAA1 antibody immobilization process is shown in Figure 4.

2.6. Experimental Setup. The experimental setup used to investigate the detection of lung cancer biomarkers using the nanoporous AAO chip is shown in Figure 5. The measurement system consisted of a spectrometer (QE65000, Ocean Optics Inc.), a white light source (DH-2000-BAL, Ocean Optics Inc.), a reflectance optical probe, an antigen-antibody

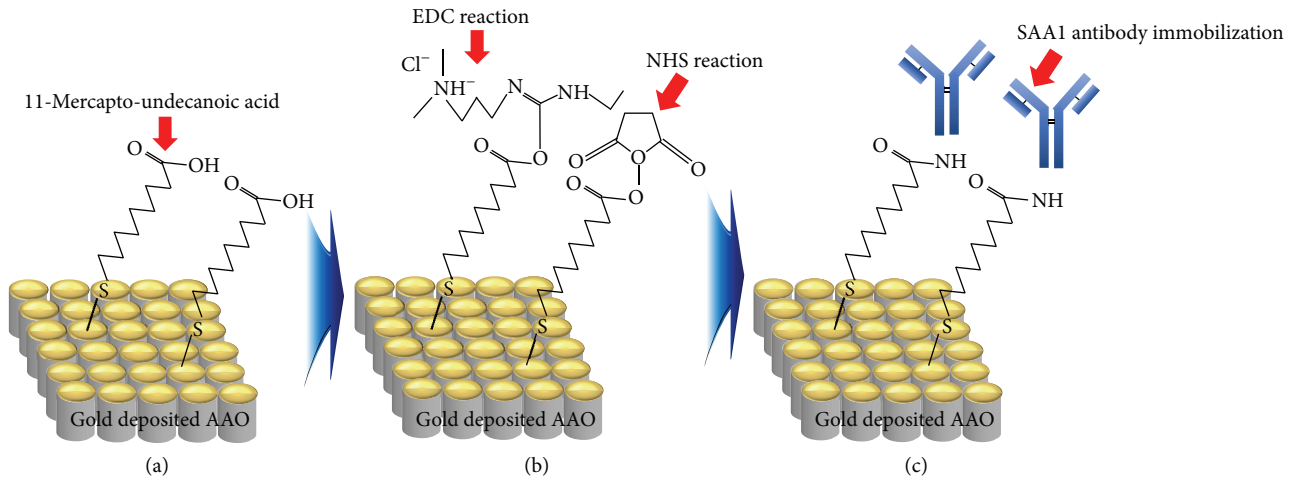


FIGURE 4: Schematic illustration of the surface functionalization steps of gold modified AAO for SAA1 antibody: (a) the formation of self-assembled monolayers (SAMs) of carboxyl-containing thiol followed by (b) covalent attachment of streptavidin of activated SAMs after activation with coupling (NHS/EDC) agents and finally (c) immobilization of SAA1 antibody.

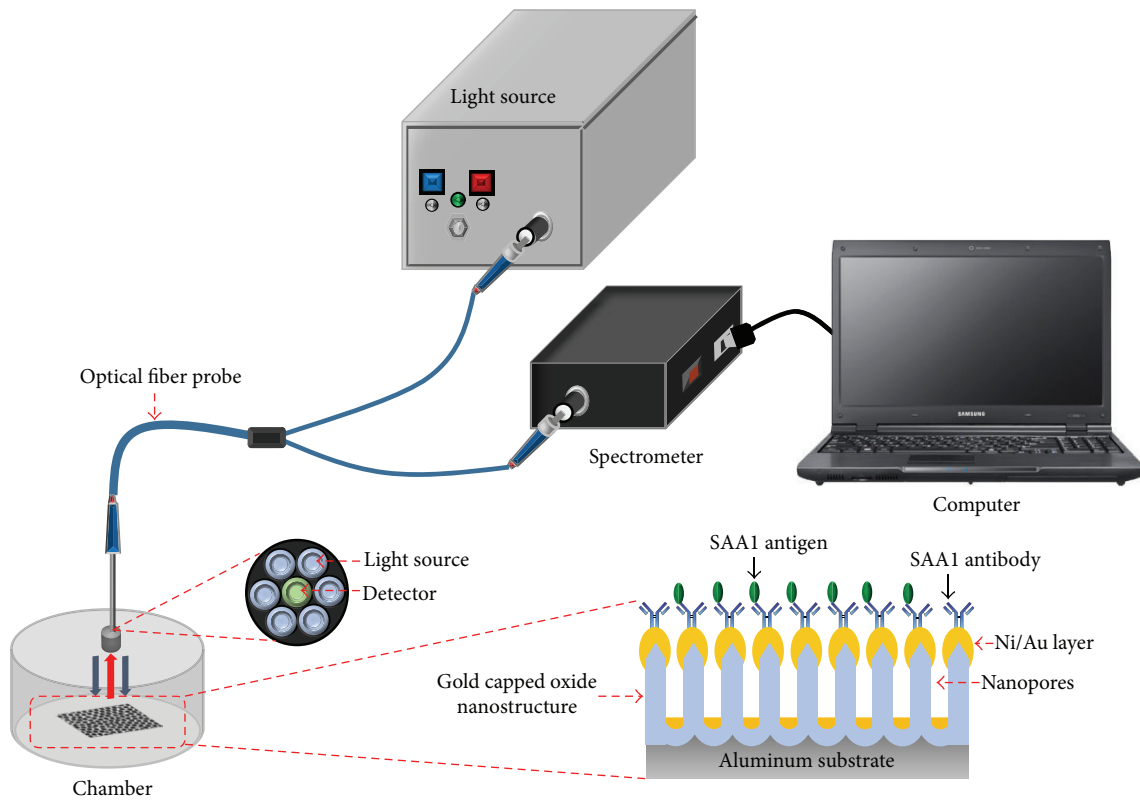


FIGURE 5: Schematic diagram of the lung cancer biomarker measurement system.

reaction chamber, and the AAO chip. The white light source operates in dual mode using deuterium and tungsten-halogen lamps, with the wavelength range of 210 to 1500 nm. The spectrometer has a wide detection range of 200 to 1100 nm and a maximum resolution of 0.14 nm. The spectrometer is equipped with diverse measurement functions that include transmission, absorption, and reflection. When the light is incident on one direction, the optical probe is connected to

the white light source while the other direction is connected to spectrometer. The light is incident in the vertical direction to the sensing membrane through an optical probe fixed to the fabricated chamber. The reflected light is sent to the spectrometer through a light detector using the same optical probe. The reflected light was analyzed using computer spectro-analysis program (Spectrasuit, Ocean Optics Inc.) connected to the spectrometer.

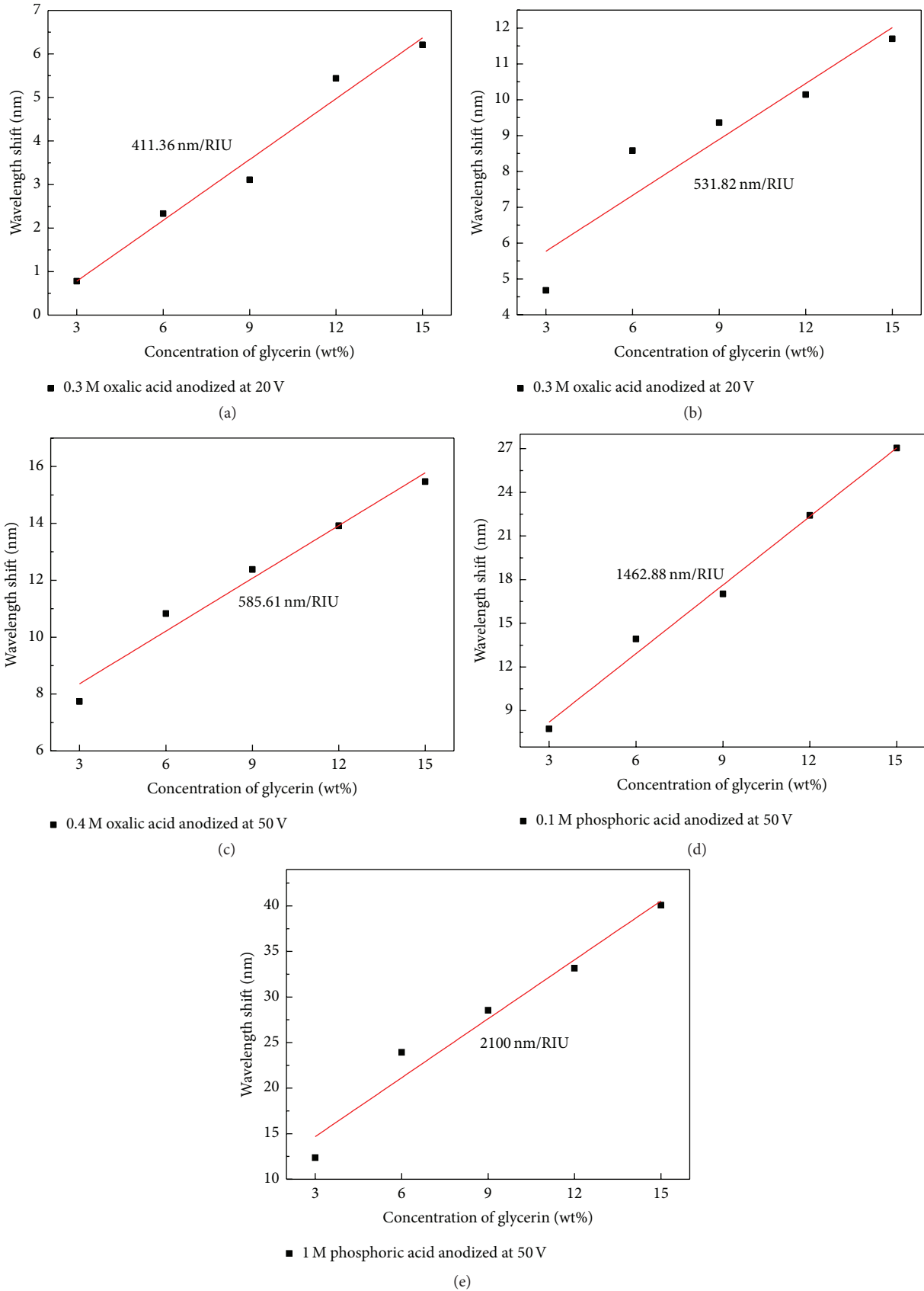


FIGURE 6: The wavelength shift of various pore diameters of AAO chip according to changes in refractive index of glycerin solutions: (a) 15 nm, (b) 35 nm, (c) 55 nm, (d) 75 nm, and (e) 95 nm.

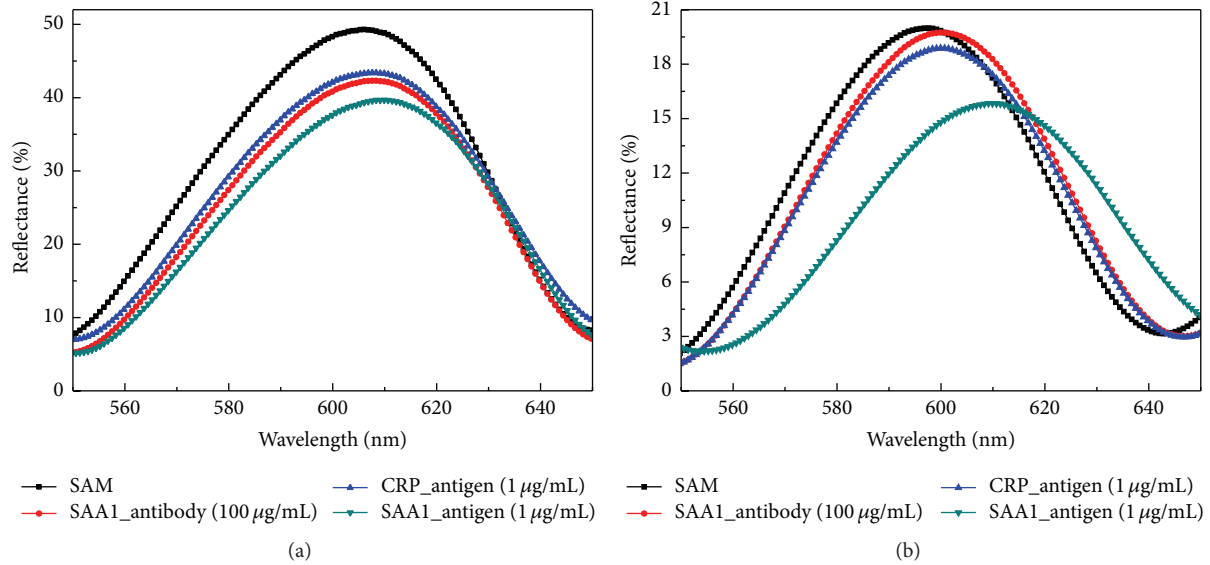


FIGURE 7: Selectivity evaluation of the AAO chip: pore diameter of (a) 15 nm and (b) 95 nm.

3. Results and Discussions

3.1. Optical Characteristics of the Sensing Membrane. The optical properties of the sensor chip were verified by detecting changes in the surface refraction. In order to measure optical properties of the change in the interference spectrum against the change in refraction, a glycerin solution was diluted to 3, 6, 9, 12, and 15% concentrations in distilled water to prepare the refraction solution. Glycerin is commonly used as a RI standard to determine the weight-percent variation. The RI of the refraction solution was performed using an Abbe refractometer (Prisma, CETI, England). The refractive indices were found to be 1.3359, 1.3392, 1.3430, 1.3458, and 1.3491. After spin-coating, the prepared refraction solution was added to the gold-deposited AAO chip (15, 35, 55, 75, and 95 nm). Next, the optical properties were verified using a measurement system. As a result, the sensitivity was found to be dependent on the increases in the pore diameters of the AAO chip. Figure 6 shows the shifting of the reflective interference signal on the nanoporous AAO chip according to various RIs of the glycerin solutions. The result shows that the sensitivity of the AAO chip with the 95 nm pore diameter is higher than the sensitivities recorded for other diameter sizes of the pore. The AAO chip with the 95 nm pore diameter was found to have 2100 nm/refractive index unit (RIU). We confirmed that the proposed AAO chip can detect RI changes of the surrounding media that result from exposure to the SAA1 antigen.

3.2. Response Characteristics SAA1. To observe the selectivity of the fabricated AAO chip, we evaluated the AAO chips (15 and 95 nm) that can distinguish between SAA1 antigen and C-reactive protein (CRP) antigen. The concentration of SAA1 antigen used was 1 µg/mL, and also the concentration of the CRP antigen was 1 µg/mL in the selectivity experiment. As the results shown in Figure 7, the CRP antigen did not make significant changes in reflectance wavelength, which

indicated that no nonspecific binding of the CRP antigen took place on the sensing membrane. However, the SAA1 antigen caused a notable reflectance wavelength shift. The SAA1 antigen wavelengths of the AAO chips with 15 and 95 nm pore diameters were ranging from 606 nm to 609 nm and 597 nm to 609 nm, respectively. These results revealed the significant response difference between the lineage-specific recognition and the nonspecific reaction. Subsequently, we confirmed other kinds of antigens with the fabricated AAO chip in order to estimate its selectivity.

A nanoporous AAO chip was fabricated to detect immune responses with high sensitivity by combining LSPR with interference. In addition, to evaluate the possibility of its application as a biosensor, the detection properties of the SAA1 antigen were measured. In order to confirm the response characteristics, we applied various concentrations of SAA1 antigen (10 ag/mL, 100 ag/mL, 1 fg/mL, 1 pg/mL, 1 ng/mL, and 1 µg/mL) to the sensing membrane that has SAA1 antibodies immobilized on surface of the AAO chip. Nonspecific binding of the detection membrane prepared by immobilizing the SAA1 antibody was removed by washing with Tris-HCl buffer solution prior to measurement of the reference reflection's wavelength. For improved reliability of the measurement system, the SAA1 antigen was allowed to react with the SAA1 antibody that was immobilized to the sensing membrane by injecting the antigen into the reaction chamber. The shift in the reflection spectrum of the membrane was then measured in real-time. The wavelength shift of reflectance spectra of the nanoporous AAO chip according to concentrations of SAA1 is shown in Figure 8.

Figure 8 shows the reflective interference signal according to various concentrations of SAA1 as a bathochromic shift in the nanoporous AAO chip (15 and 95 nm). When comparing the sensitivity of AAO chips of different pore diameters, it was observed that the AAO chip with the 95 nm pore diameter had larger shifts in the fringe pattern. Moreover, the LOD of

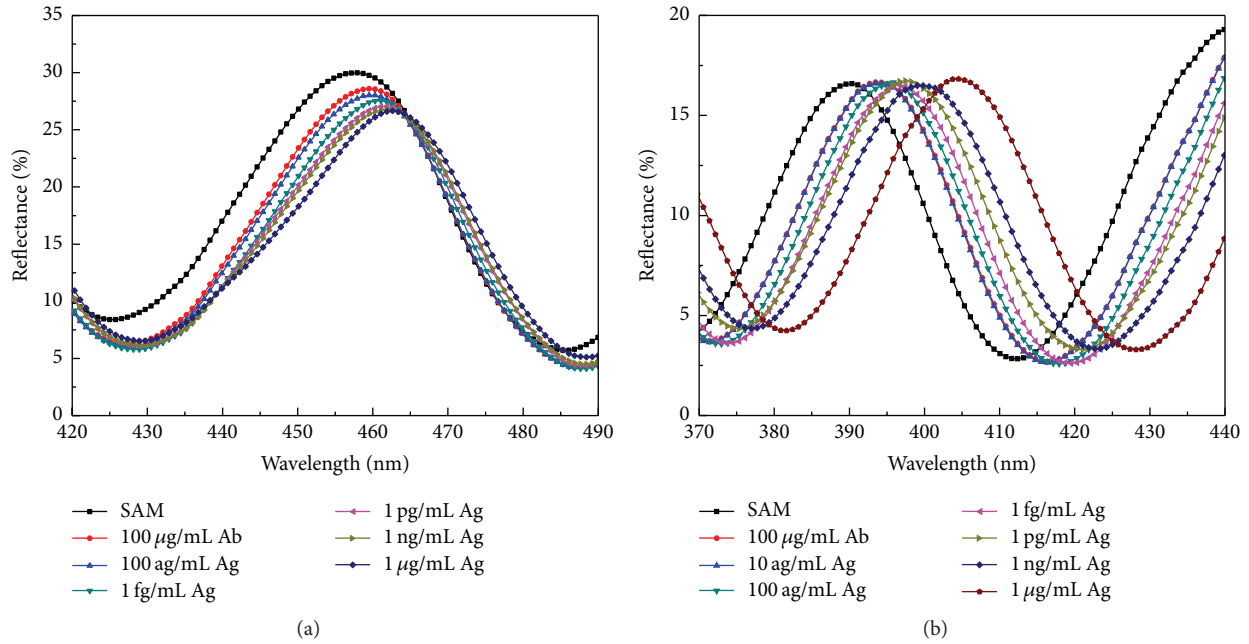


FIGURE 8: The wavelength shift of reflectance spectra AAO chip according to concentrations of SAA1: pore diameter of (a) 15 nm and (b) 95 nm.

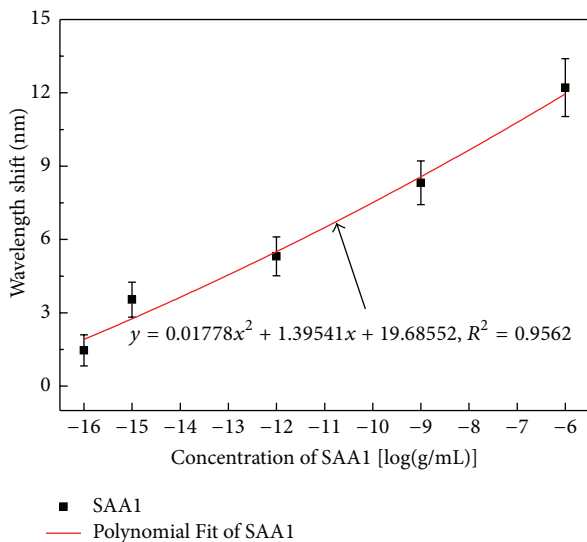


FIGURE 9: The polynomial-regression analysis response according to variations in SAA1 concentrations.

the AAO chips with 15 and 95 nm pore diameters were found to be 1 fg/mL and 100 ag/mL, respectively. The experimental measurements were repeated five times. As a result, we confirmed that the nanoporous AAO chip with 95 nm pore diameter appears to have the highest sensitivity and performance. These experiments were repeated several times. Moreover, the polynomial-regression analysis showed a good correlation coefficient (R^2), $R^2 = 0.9562$. Figure 9 shows the polynomial-regression analysis response to variations in SAA1 concentrations.

4. Conclusions

In this study, nanoporous AAO chips, wherein interference and LSPR occur simultaneously, were fabricated, and their response properties for various SAA1 concentrations were evaluated in real-time. The AAO chip with excellent surface uniformity was prepared through optimization of the anodization process that could adjust the various pore diameters. The AAO chip quantitatively detected SAA1 with high sensitivity. We obtained high sensitivity (2100 nm/RIU) for optical responses to the changes in the surface RI of the nanoporous AAO membrane. In addition, the SAA1 antigen concentration of 10 ag/mL was also detected via experiments based on immune response. The reflection spectrum properties were analyzed by reacting SAA1 antigen instead of the target biomaterial to evaluate the selectivity of the nanoporous AAO chip and then by analyzing the reflection wavelength. As a result, the sensitivity properties induced by changes in pore diameters were measured to evaluate interference. Best response properties were verified using the device with a 95 nm pore diameter because of the relative change in effective optical pore diameter of the nanoporous AAO membrane. The fabricated AAO chip was verified so it reacts with high selectivity to the lung cancer-specific biomaterial. The detection limit was found to be 100 ag/mL. In the future, we plan to extend the analysis to include biomarker experiments that use pore diameters larger than 95 nm.

Conflict of Interests

The authors declare that there is no conflict of interests regarding the publication of this paper.

Authors' Contribution

Jae-Sung Lee and Sae-Wan Kim contributed equally to this work.

Acknowledgment

This work was supported by the National Research Foundation of Korea (NRF) grant funded by the Korea Government (MSIP) (no. NRF2014R1A2A1A11050377).

References

- [1] A. Hasan, M. Nurunnabi, M. Morshed et al., "Recent advances in application of biosensors in tissue engineering," *BioMed Research International*, vol. 2014, Article ID 307519, 18 pages, 2014.
- [2] A. Malima, S. Siavoshi, T. Musacchio et al., "Highly sensitive microscale in vivo sensor enabled by electrophoretic assembly of nanoparticles for multiple biomarker detection," *Lab on a Chip*, vol. 12, no. 22, pp. 4748–4754, 2012.
- [3] M. E. Ali, U. Hashim, S. Mustafa et al., "Nanobiosensor for detection and quantification of DNA sequences in degraded mixed meats," *Journal of Nanomaterials*, vol. 2011, Article ID 781098, 11 pages, 2011.
- [4] A. N. Lad and Y. K. Agrawal, "SiO₂-based nanobiosensor monitoring toxicological behavior of Mitoxantrone in vitro," *Applied Nanoscience*, vol. 4, no. 5, pp. 523–529, 2014.
- [5] C. H. Choi, "Integrated nanobiosensor technology for biomedical application," *Nanobiosensors in Disease Diagnosis*, vol. 2012, article 1, pp. 1–4, 2012.
- [6] J. Zhang, C. S. Day, and D. L. Carroll, "Controlled growth of novel hyper-branched nanostructures in nanoporous alumina membrane," *Chemical Communications*, vol. 7, no. 45, pp. 6937–6939, 2009.
- [7] A. Numnuam, P. Thavarungkul, and P. Kanatharana, "An amperometric uric acid biosensor based on chitosan-carbon nanotubes electrospun nanofiber on silver nanoparticles," *Analytical and Bioanalytical Chemistry*, vol. 406, no. 15, pp. 3763–3772, 2014.
- [8] R. D. Jean, W. D. Cheng, M. H. Hsiao, F. H. Chou, J. S. Bow, and D. M. Liu, "Highly electrostatically-induced detection selectivity and sensitivity for a colloidal biosensor made of chitosan nanoparticle decorated with a few bare-surfaced gold nanorods," *Biosensors and Bioelectronics*, vol. 52, no. 15, pp. 111–117, 2014.
- [9] M. J. Kiani, M. A. A. Razak, F. K. Che Harun, M. T. Ahmadi, and M. Rahmani, "SWCNT-based biosensor modelling for pH detection," *Journal of Nanomaterials*, vol. 2015, Article ID 721251, 7 pages, 2015.
- [10] J. Zhao, X. Zhang, C. R. Yonzon, A. J. Haes, and R. P. Van Duyne, "Localized surface plasmon resonance biosensors," *Nanomedicine*, vol. 1, no. 2, pp. 219–228, 2006.
- [11] I. M. Klotz, *Ligand-Receptor Energetics: A Guide for the Perplexed*, Wiley, 1997.
- [12] D. Kim, K. Kerman, M. Saito et al., "Label-free DNA biosensor based on localized surface plasmon resonance coupled with interferometry," *Analytical Chemistry*, vol. 79, no. 5, pp. 1855–1864, 2007.
- [13] X. Fan, I. M. White, S. I. Shopova, H. Zhu, J. D. Suter, and Y. Sun, "Sensitive optical biosensors for unlabeled targets: a review," *Analytica Chimica Acta*, vol. 620, no. 1–2, pp. 8–26, 2008.
- [14] M. M. Rahman, A. J. Ahammad, J. Jin, S. J. Ahn, and J. Lee, "A comprehensive review of glucose biosensors based on nanostructured metal-oxides," *Sensors*, vol. 10, no. 5, pp. 4855–4886, 2010.
- [15] B. D. Malhotra and A. Chaubey, "Biosensors for clinical diagnostics industry," *Sensors and Actuators B: Chemical*, vol. 91, no. 1–3, pp. 117–127, 2003.
- [16] M. Saigusa, K. Tsuboi, Y. Konosu, M. Ashizawa, A. Tanioka, and H. Matsumoto, "Highly sensitive local surface plasmon resonance in anisotropic Au nanoparticles deposited on nanofibers," *Journal of Nanomaterials*, vol. 2015, Article ID 829273, 8 pages, 2015.
- [17] P. Schuck, "Reliable determination of binding affinity and kinetics using surface plasmon resonance biosensors," *Current Opinion in Biotechnology*, vol. 8, no. 4, pp. 498–502, 1997.
- [18] D. A. Mann, M. Kanai, D. J. Maly, and L. L. Kiessling, "Probing low affinity and multivalent interactions with surface plasmon resonance: ligands for concanavalin A," *Journal of the American Chemical Society*, vol. 120, no. 41, pp. 10575–10582, 1998.
- [19] J. M. Brockman, A. G. Frutos, and R. M. Corn, "A multistep chemical modification procedure to create DNA arrays on gold surfaces for the study of protein-DNA interactions with surface plasmon resonance imaging," *Journal of the American Chemical Society*, vol. 121, no. 35, pp. 8044–8051, 1999.
- [20] K. C. Popat, G. Mor, C. A. Grimes, and T. A. Desai, "Surface modification of nanoporous alumina surfaces with poly(ethylene glycol)," *Langmuir*, vol. 20, no. 19, pp. 8035–8041, 2004.
- [21] S. Zhao, H. Roberge, A. Yelon, and T. Veres, "New application of AAO template: a mold for nanoring and nanocone arrays," *Journal of the American Chemical Society*, vol. 128, no. 38, pp. 12352–12353, 2006.
- [22] I. Vlasiouk, A. Krasnoslobodtsev, S. Smirnov, and M. Germann, "'Direct' detection and separation of DNA using nanoporous alumina filters," *Langmuir*, vol. 20, no. 23, pp. 9913–9915, 2004.
- [23] S. H. Yeom, O. G. Kim, B. H. Kang et al., "Highly sensitive nanoporous lattice biosensor based on localized surface plasmon resonance and interference," *Optics Express*, vol. 19, no. 23, pp. 22882–22891, 2011.
- [24] S. Yeom, M. Han, B. Kang et al., "Enhancement of the sensitivity of LSPR-based CRP immunosensors by Au nanoparticle antibody conjugation," *Sensors and Actuators B: Chemical*, vol. 177, pp. 376–383, 2013.
- [25] T. Yamada, "Serum amyloid A (SAA): a concise review of biology, assay methods and clinical usefulness," *Clinical Chemistry and Laboratory Medicine*, vol. 37, no. 4, pp. 381–388, 1999.
- [26] M. Kimura, Y. Tomita, T. Imai et al., "Significance of serum amyloid a on the prognosis in patients with renal cell carcinoma," *Cancer*, vol. 92, no. 8, pp. 2072–2075, 2001.
- [27] W. C. Cho, T. T. Yip, W. W. Cheng, and J. S. Au, "Serum amyloid A is elevated in the serum of lung cancer patients with poor prognosis," *British Journal of Cancer*, vol. 102, no. 12, pp. 1731–1735, 2010.
- [28] B. A. Howard, M. Z. Wang, M. J. Campa, C. Corro, M. C. Fitzgerald, and E. F. Patz, "Identification and validation of a potential lung cancer serum biomarker detected by matrix-assisted laser desorption/ionization-time of flight spectra analysis," *Proteomics*, vol. 3, no. 9, pp. 1720–1724, 2003.

- [29] H. Biran, N. Friedman, L. Neumann, M. Pras, and R. Shainkin-Kestenbaum, "Serum amyloid A (SAA) variations in patients with cancer: correlation with disease activity, stage, primary site, and prognosis," *Journal of Clinical Pathology*, vol. 39, no. 7, pp. 794–797, 1986.
- [30] B. B. Rossi, *Optics*, Addison-Wesley, 1957.
- [31] A. V. Whitney, J. W. Elam, S. Zou et al., "Localized surface plasmon resonance nanosensor: a high-resolution distance-dependence study using atomic layer deposition," *The Journal of Physical Chemistry B*, vol. 109, no. 43, pp. 20522–20528, 2005.
- [32] H. Masuda and K. Fukuda, "Ordered metal nanohole arrays made by a two-step replication of honeycomb structures of anodic alumina," *Science*, vol. 268, no. 5216, pp. 1466–1468, 1995.
- [33] H. Liu, B. Wang, E. S. P. Leong et al., "Enhanced surface plasmon resonance on a smooth silver film with a seed growth layer," *ACS Nano*, vol. 4, no. 6, pp. 3139–3146, 2010.
- [34] N. K. Chaki, M. Aslam, J. Sharma, and K. Vijayamohanan, "Applications of self-assembled monolayers in materials chemistry," *Journal of Chemical Sciences*, vol. 113, no. 5-6, pp. 659–670, 2001.

Research Article

Preparation of Mixed Semiconductors for Methyl Orange Degradation

Sangeeta Adhikari and Debasish Sarkar

Department of Ceramic Engineering, National Institute of Technology, Rourkela, Odisha 769008, India

Correspondence should be addressed to Debasish Sarkar; dsarkar@nitrkl.ac.in

Received 4 April 2015; Accepted 17 May 2015

Academic Editor: Anh-Tuan Le

Copyright © 2015 S. Adhikari and D. Sarkar. This is an open access article distributed under the Creative Commons Attribution License, which permits unrestricted use, distribution, and reproduction in any medium, provided the original work is properly cited.

Attempts were made to compare the photocatalytic efficacy in between quasi-fiber and near spherical commercial grade ZnO through the addition of monoclinic WO₃ nanocuboid. Mixed oxide semiconductors were assessed for their dye degradation performance under irradiation of visible light energy. Surface area and the particle morphology pattern have an influence on the resultant photocatalytic features of these mixed oxide composites. The high porous quasi-fibrous ZnO was successfully fabricated by a simple solution combustion method. It is deliberately made of clusters of primary near spherical particles that supports WO₃ nanocuboid embedment and shows interactive characteristics in comparison to the counterpart commercial near spherical ZnO combined with WO₃. The photocatalytic activity significantly increases up to 95% under visible radiation for 90 min due to high surface area imparted by unique quasi-fiber morphology. The photogenerated electron-hole pair interaction mechanism has been proposed to support the photocatalytic behavior.

1. Introduction

Environmental pollution caused by anthropogenic sources majorly contributes to the overall imbalance of the ecosystem. Release of waste organic dye solution directly into the water system from the textile and small scale industries is a serious problem faced by developed and developing nations in the world. Most of the common pollutants include toxic organic as well as inorganic compounds along with some biological pathogens that are naturally present in the environment. In the recent era, industrial waste water purification using photocatalysis is an active research area of interest [1]. Metal oxide semiconductor photocatalysts offer a way for the treatment of organic contaminants in the presence of solar energy. Visible light-driven oxidation process technology using semiconductor materials has grown for many energy and environmental benefits [2, 3]. The nanostructured ZnO has been studied widely for photocatalytic application [4, 5]. The UV range activity limits the utilization of ZnO as a visible light photocatalyst. Furthermore, the photocatalyst requires further improvement due to its fast recombination

rate of the photogenerated electron-hole pairs [6]. Literature reports the augmentation in photocatalytic activity of ZnO by coupling with other semiconductor materials like ZnSe [7], WO₃ [8], CdS [9], and so forth. Among the semiconductors, tungsten oxide semiconductor is worthy of attention due to its small band gap enabling absorption in the visible region, stable physicochemical properties, and resistance to photocorrosion effect [10]. Synthetic attempts to prepare this mixed oxide for photocatalytic purpose are limited in recent literature. Hence, surface modification has been done by loading different amount of WO₃ in ZnO to degrade different dyes [11, 12]. Surface modified ZnO nanorods with WO₃ nanoparticles coated on the surface were synthesized through hydrothermal technique for efficient degradation of endocrine disrupting chemicals like phenol, bisphenol A, and methylparaben under irradiation of 55 W compact fluorescence lamp [12]. In another research, WO₃-ZnO composites were prepared using the wet chemical method and further used to degrade methyl orange. High degradation was observed with 3 mol% WO₃ loaded ZnO under UV light irradiation for 3 h [11]. The existing reports disclose a

maximum 50% efficiency achievement under visible light using WO_3 modified ZnO nanoparticles [13, 14]. The literature lacks in reporting high photocatalytic activity using the visible light after the versatile surface modification. Therefore, the development of WO_3 -ZnO nanocomposites is a critical challenge for efficient visible light photocatalytic activity. In the present study, nanocuboid WO_3 and quasi-fibrous ZnO have been prepared by wet chemical methods and assessed the photocatalytic performance of mixed oxide nanocomposites under visible light irradiation. A further comparison has been carried out with reference to commercial ZnO powders with exploration to the charge separation mechanism.

2. Experimental Procedure

2.1. Synthesis of Nanoparticles. Tungsten trioxide (WO_3) nanoparticle was synthesized by hydrothermal treatment of the precipitate solution formed by mixing sodium tungstate dihydrate and 4 M fluoroboric acid at 180°C for 6 hr. The detailed experimental procedure can be found elsewhere [15]. Fluoroboric acid was used as structure directing reagents for the confined growth of WO_3 nanoparticles. The reaction slurry was poured into a Teflon-lined beaker and kept in a hot air oven at prerequisite temperature. The powder obtained was isolated after thorough washing with water and isopropanol followed by drying at 80°C .

In another end, a rapid combustion process was followed to prepare quasi-fibrous ZnO nanoparticles (FZ) at temperature 450°C for 30 min from a gel solution of zinc nitrate hexahydrate and oxalic acid in stoichiometry [16]. Easy dissolution of metal nitrate helps in the formation of the gel. The gel solution was kept in a preheated muffle furnace for combustion. A white porous mass was obtained after the complete reaction.

2.2. Preparation of WO_3 -ZnO Nanocomposites. The WO_3 -ZnO nanocomposite was prepared by mixing of an optimum amount of 10 wt% WO_3 to 90 wt% ZnO (10% WO_3 -FZ) nanopowders using mortar and pestle followed by high-frequency ultrasonication to form a colloidal solution. The colloidal solution was dried at 80°C in the oven with heat treatment at 450°C for 2 hr to establish effective mixing of both the oxides. Similarly, commercial ZnO (CMZ) powder was mixed with nanocuboid WO_3 for the comparative study.

2.3. Characterization of Both Nanoparticles. X-ray diffraction (XRD) patterns for the powders were obtained using a Philips X-ray diffractometer with Ni filtered $\text{Cu-K}\alpha$ radiation ($\lambda = 1.5418 \text{ \AA}$). Detailed morphology was studied by transmission electron microscope (JEOL JEM-2100). FESEM and elemental distribution images for both 10 wt% WO_3 -FZ and 10 wt% WO_3 -CMZ nanocomposites were carried out using Nova NanoSEM FEI-450 system. UV-Visible diffuse reflectance measurement was carried out through Shimadzu spectrophotometer (UV-2450) to evaluate the band gap energy of the individual nanopowders and mixed oxide nanocomposites. Specific surface areas of all the nanopowders were measured using Quantachrome Autosorb, USA, BET apparatus with nitrogen as the adsorbate.

2.4. Photocatalytic Experiments. The photocatalytic experiments were performed in a metal halide reactor containing 50 mL of 20 mg/L aqueous solution of methyl orange (MO) and 50 mg mixed oxide catalyst. The distance between the reactor and the lamp was 2 cm. After each reaction, 2 mL of slurry was taken out and centrifuged for separating the aliquot and catalyst. The UV-Vis absorbance of the aliquot was measured, and catalyst along with the aliquot was poured back to the reaction solution after energetic hand shaking. The degradation efficiency was calculated as follows:

$$\eta = \frac{C_o - C}{C_o} \times 100, \quad (1)$$

where C_o is the absorbance of original MO solution and C is the absorbance of the MO solution after visible light irradiation at certain time interval. The photoactivity of commercial ZnO (CMZ) and nanocomposite of 10 wt% WO_3 -CMZ was also carried out for comparison.

3. Results and Discussion

3.1. Phase and Morphological Analysis. XRD pattern is depicted to analyze the phase composition and structure of all WO_3 , FZ, CMZ, and 10 wt% WO_3 -FZ nanopowders. As shown in Figure 1, all of the peaks of WO_3 are indexed to pure crystalline monoclinic WO_3 (JCPDS Card number 72-0677) crystal phase. The XRD patterns of quasi-fibers ZnO (FZ) and commercial ZnO (CMZ) matches well with the standard hexagonal wurtzite structure (JCPDS Card number 75-0576) where CMZ is found to be highly crystalline in comparison to FZ nanopowders. The 10 wt% WO_3 -FZ nanocomposite shows the presence of both monoclinic WO_3 (*) and hexagonal FZ (#) phases. Figure 2 reveals the FESEM images of all individual nanopowders (WO_3 and ZnO) and 10 wt% WO_3 -FZ nanocomposites. Figure 2(a) shows soft agglomerated cuboid-like WO_3 nanoparticles with average length $\sim 142 \text{ nm}$, width $\sim 118 \text{ nm}$, and thickness $\sim 80 \text{ nm}$, respectively. Combustion synthesized ZnO nanopowders have fiber-like morphology which is grown along a confined direction as shown in Figure 2(b). The quasi-fibers are found to have average particle length $\sim 3 \mu\text{m}$ and width $\sim 0.6 \mu\text{m}$, respectively [16]. Commercial ZnO (Figure 2(c)) is represented by highly agglomerated near spherical and anisotropic nanocomposite, whereas cuboid particles are found intimately embedded in the FZ matrix that has been illustrated and confirmed later by FESEM element mapping. The specific BET surface areas of WO_3 , FZ, CMZ, and 10% WO_3 -FZ are measured to be $5.16 \text{ m}^2/\text{g}$, $17.8 \text{ m}^2/\text{g}$, $6.19 \text{ m}^2/\text{g}$, and $15.9 \text{ m}^2/\text{g}$, respectively. A further decrease in surface area to $5.09 \text{ m}^2/\text{g}$ is observed for nanocomposite prepared using commercial ZnO powders.

In addition, TEM images of WO_3 , FZ, and CMZ put forward the clear picture of the nanopowders as represented in Figure 3. The cuboid morphology in Figure 3(a) is found to have average particle length of $\sim 150 \text{ nm}$ and width $\sim 120 \text{ nm}$. The tilting of particles at a certain angle shows the imperfect edges of individual cuboids. In FZ (Figure 3(b)), hard agglomeration of spherical particles takes place along one direction to form quasi-fiber-like particles. The in situ particle

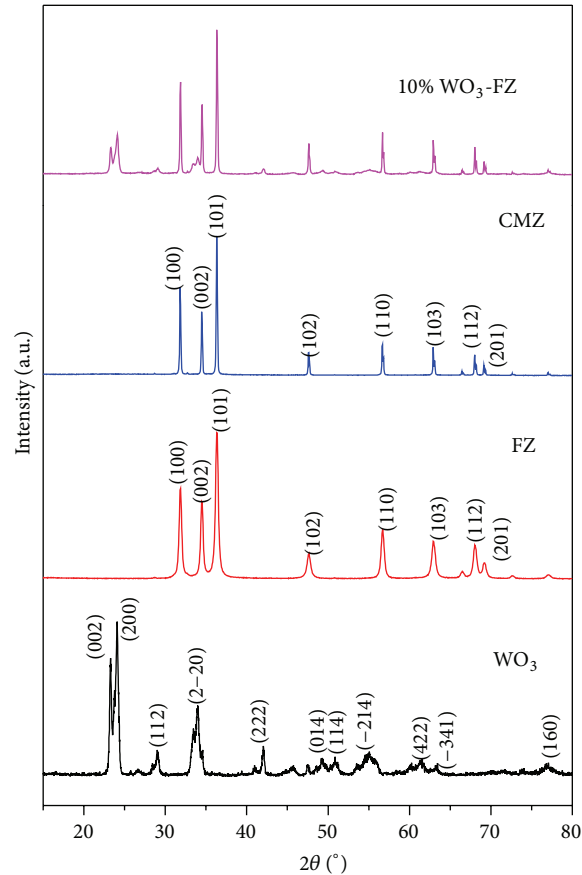


FIGURE 1: Composite X-ray diffraction pattern of WO_3 , FZ, CMZ, and 10% WO_3 -FZ.

welding takes place along a particular direction during the exothermic reaction forming fibrous structure for ZnO. The spherical particles are found to have average diameter of ~ 55 nm. Different aspect ratio particles are observed for CMZ with average particle size of ~ 225 nm as shown in Figure 3(c). The particles are seen to have high anisotropy in comparison to synthesized quasi-fiber ZnO.

3.2. Band Gap Determination. Figure 4 shows the UV-DRS spectra pattern of WO_3 , FZ, 10% WO_3 -FZ, and CMZ, respectively. A distinct right shift of 10% WO_3 -FZ nanocomposite (blue color line) has been observed compared to the counterpart pure quasi-fiber ZnO (FZ). This depicts that the optical absorption ability of the nanocomposite persists in the whole range of visible light spectrum [17]. The band gap calculation for the individual nanoparticles and the nanocomposite has been carried out using Tauc plot. The Tauc plot is derived from the square root of Kubelka-Munk function ($\text{KMU} = (1 - R)^2/2R$, R = reflectance) multiplied by the photon energy and plotted against photon energy ($E_{\text{photon}} = h\nu$). Different degree of band gap energy (E_g) for WO_3 , FZ, 10% WO_3 -FZ, and CMZ is calculated to be 2.6 eV, 2.95 eV, 3.05 eV, and 3.17 eV, respectively.

3.3. Elemental Analysis of WO_3 -ZnO Nanocomposites. Figures 5(a) and 5(b) represent the FESEM elemental mapping

of both essential 10% WO_3 -FZ and 10% WO_3 -CMZ nanocomposites. Individual elements such as W and Zn are represented in green and red color, whereas common blue color homogeneously distributed all along the matrix represents the oxygen atom. The distinct morphology clearly demonstrates the intimate contact in between two classes of particles in both the nanocomposites. However, a close look eventually depicts the presence of WO_3 on fibrous ZnO, whereas nanocuboid WO_3 is seen covered by commercial near spherical ZnO particles.

3.4. Photocatalytic Degradation of Methyl Orange. The photocatalytic activity of 10% WO_3 -FZ nanocomposite has been studied by degrading methyl orange under metal halide irradiation. As a comparison, degradation of MO with WO_3 , ZnO quasi-fibers, commercial ZnO, and 10% WO_3 -CMZ photocatalysts is also carried out under similar conditions. Figure 6 shows degradation profile for MO degradation. The degradation graph is plotted with respect to MO concentration as a function of irradiation time C to the initial concentration C_0 . It can be seen that only 18% of MO is degraded with individual WO_3 nanopowders. However, a difference of 12% is observed between CMZ and FZ that reveals higher activity of combustion synthesized ZnO than the commercial ZnO photocatalyst. High degradation of 95% is observed in the presence of 10% WO_3 -FZ nanocomposites,

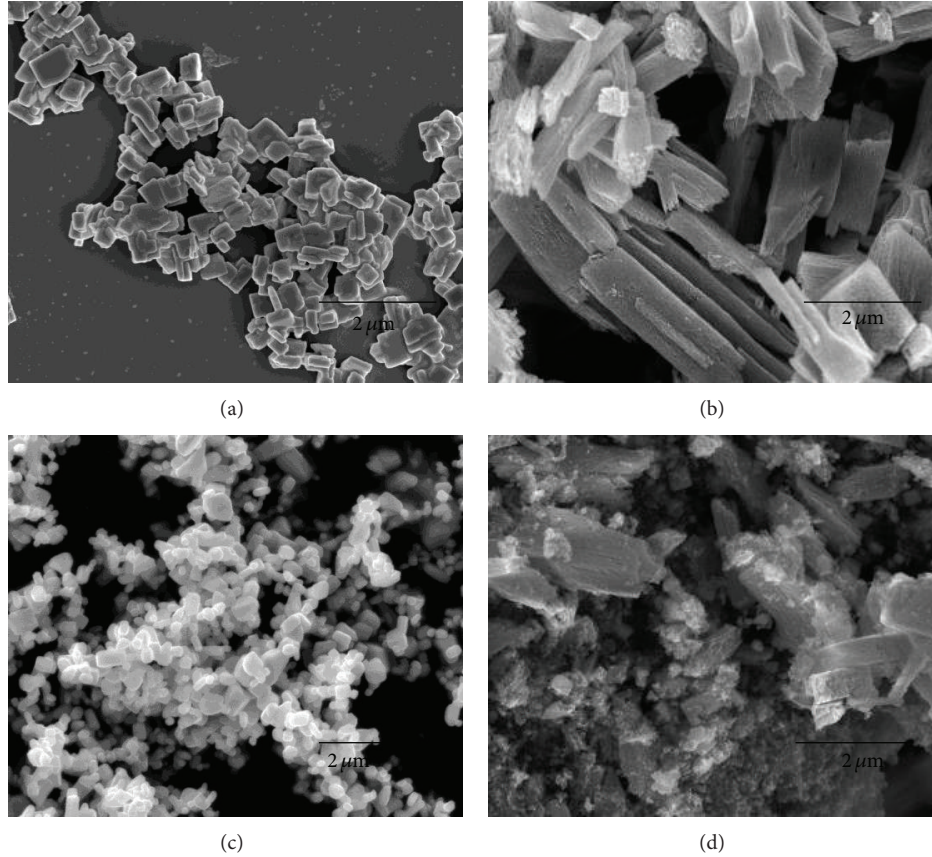


FIGURE 2: FESEM images of (a) WO_3 nanoparticles, (b) FZ, (c) CMZ, and (d) 10% WO_3 -FZ.

whereas a relatively low 85% degradation is observed for 10% WO_3 -CMZ.

The degradation kinetics has been calculated following the first-order kinetic equation: $\ln(C/C_0) = -kt$, where k is the first-order rate constant and t is the time [18]. The kinetic constant of FZ is 1.2 times higher than CMZ, whereas the kinetic constant of 10% WO_3 -FZ nanocomposite shows 2.0 times higher degradation than 10% WO_3 -CMZ, respectively. The correlation coefficient (R^2) observed after linear fitting shows $R^2 > 95$ for all the powders that depicts that the photochemical reaction followed first-order kinetics (Figure 7). Representative photodegradation data of all the powders and nanocomposites is tabulated in Table 1.

3.5. Photocatalytic Mechanism. The enhanced photocatalytic performance of 10% WO_3 -FZ nanocomposite can be attributed to the effective separation of photogenerated electron-hole pairs. However, well elemental dispersion in the WO_3 -FZ composite matrix and exposure of large number of active sites due to high surface area of quasi-fibrous ZnO play a vital role in charge separation. Since the composite has a narrow band gap WO_3 and wide band gap ZnO semiconductors, the possible mechanism for the nanocomposite could be harvesting visible light energy through narrow band gap WO_3 present on the surface of quasi-fiber ZnO for excitation of electrons as shown in Figure 8. The recombination of

TABLE 1: Representative surface area and photodegradation data of methyl orange.

Sample	Surface area (m^2/g)	% degradation	R^2	k (min^{-1})
WO_3	5.16	18%	0.9679	-0.00221
FZ	17.8	80%	0.9927	-0.01832
CMZ	6.19	68%	0.9531	-0.01277
10% WO_3 -FZ	15.9	95%	0.9831	-0.03459
10% WO_3 -CMZ	5.09	85%	0.9756	-0.02191

electron-hole pair is reduced via trapping of photoexcited electrons by ZnO to make the system be in equilibrium. These electrons and holes react with surface molecules like O_2 and H_2O to produce superoxide and hydroxyl radical anions. The $\cdot\text{O}_2^-$ and $\cdot\text{OH}$ species further reacts with dye molecules to degrade them to lower inorganic molecules like CO_2 and H_2O . Similar observation has been reported for ZnO doped Bi_2O_3 powder under visible irradiation for 6 hr [19].

4. Conclusions

Apparent fusion within primary nanoparticle develops quasi-fiber ZnO during combustion process and structure directing

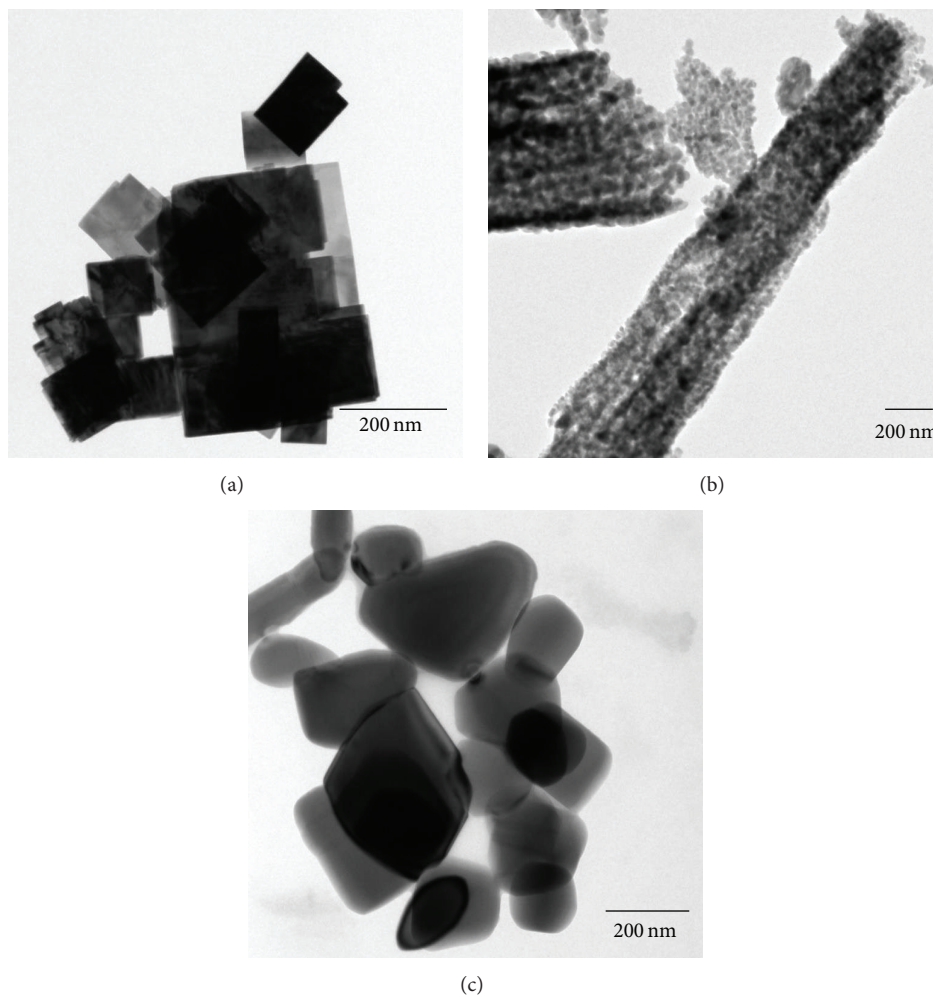


FIGURE 3: TEM images of (a) WO_3 , (b) FZ, and (c) CMZ.

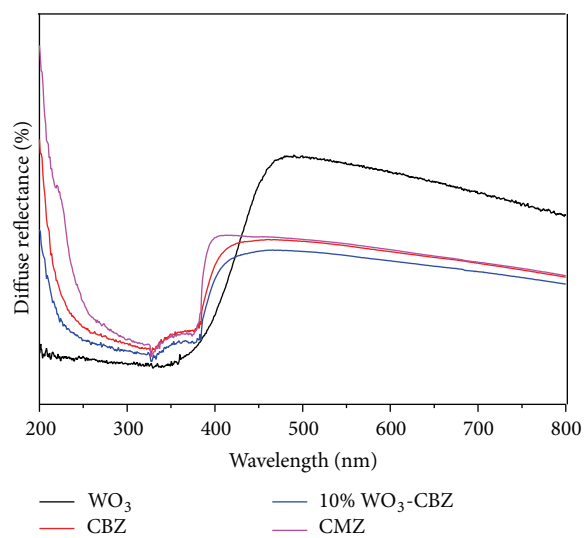


FIGURE 4: Composite UV diffuse reflectance spectrum.

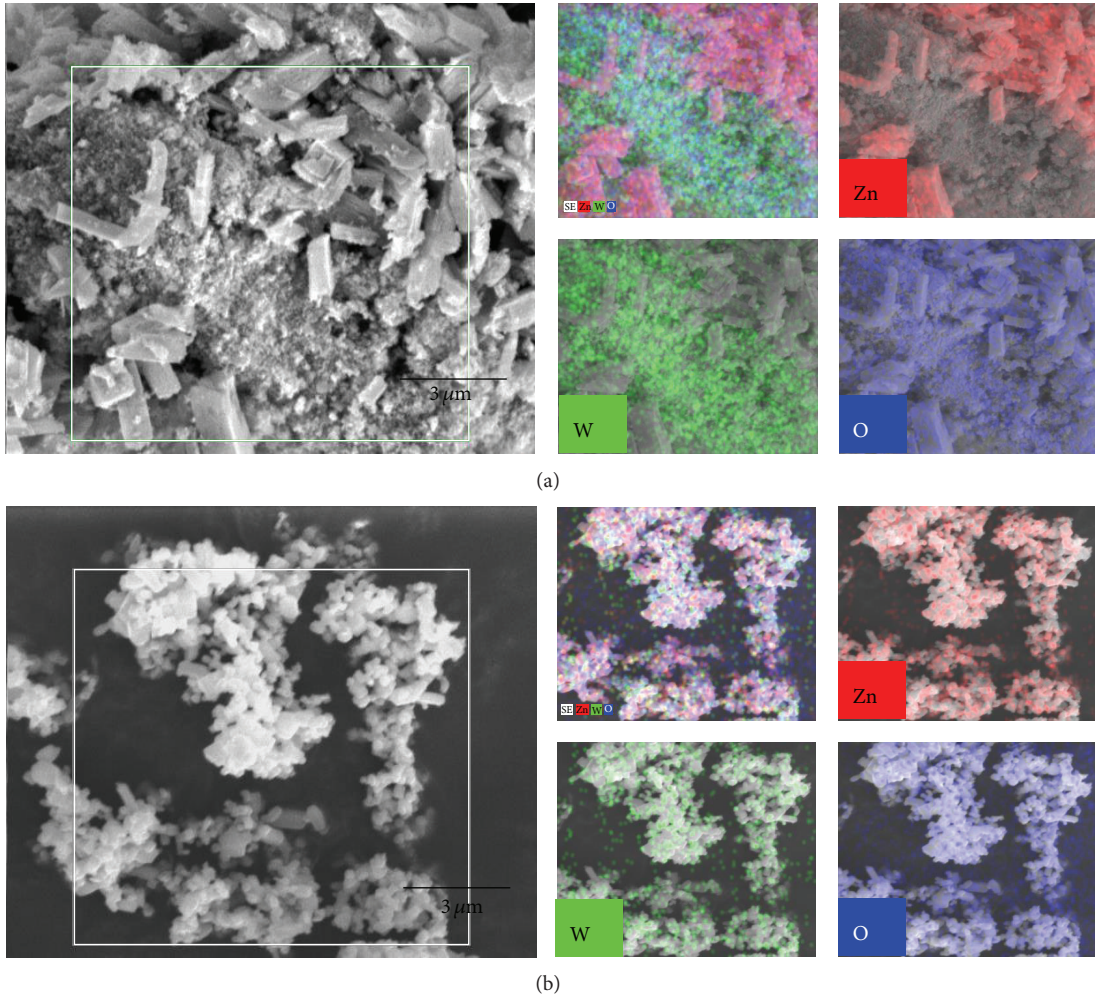


FIGURE 5: FESEM elemental mapping of (a) 10% WO₃-FZ and (b) 10% WO₃-CMZ.

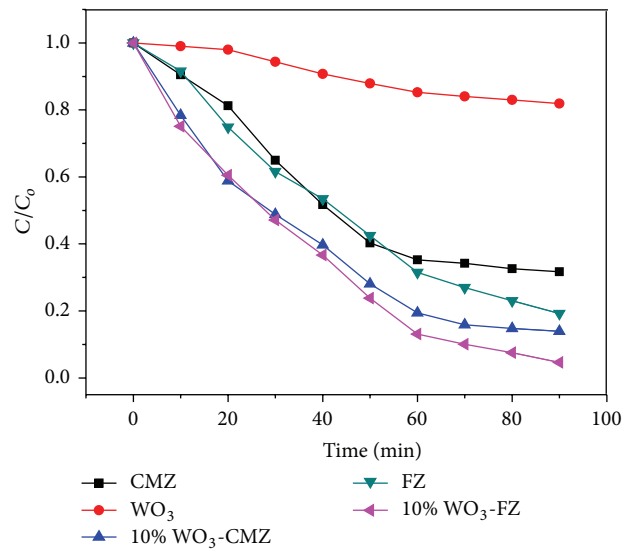


FIGURE 6: Degradation profile for methyl orange degradation.

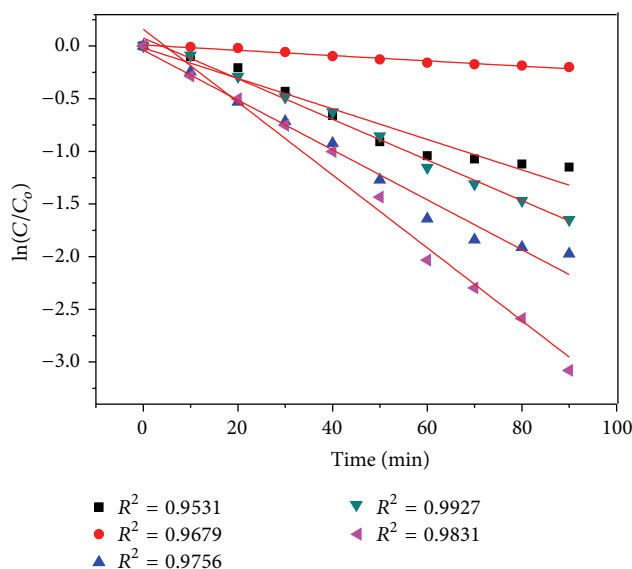


FIGURE 7: Kinetic profile for methyl orange degradation.

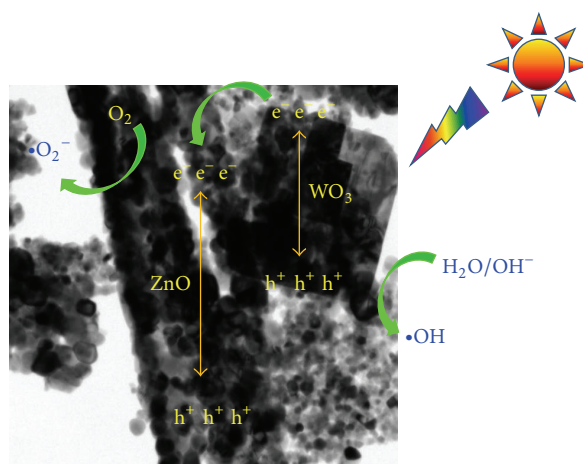


FIGURE 8: Schematic diagram of WO_3 -ZnO photocatalysis.

agent fluoroboric acid directs cuboid shape in WO_3 . An optimum amount of 10 wt% nanocuboid WO_3 in quasi-fibrous ZnO matrix is an effective choice for methyl orange dye degradation compared to commercial ZnO nanoparticles. The band gap difference and intimate contact initiate the visible light harvesting and electron excitation and reduce the electron-hole pair recombination to maintain equilibrium in the photochemical system. This process directs the radical reaction and hence subsequent dye degradation. The prepared mixed oxide nanocomposite of WO_3 and ZnO is found as an effective photocatalyst for degradation of organic pollutants in water.

Conflict of Interests

The authors declare that there is no conflict of interests regarding the publication of this paper.

Acknowledgments

The authors would like to thank Department of Science and Technology for research assistance. Special thanks are due to Mr. Subhabrata Chakraborty for FESEM measurements.

References

- [1] N. S. Lewis and D. G. Nocera, "Powering the planet: chemical challenges in solar energy utilization," *Proceedings of the National Academy of Sciences of the United States of America*, vol. 103, no. 43, pp. 15729–15735, 2006.
- [2] K. Maeda, T. Takata, M. Hara et al., "GaN:ZnO solid solution as a photocatalyst for visible-light-driven overall water splitting," *Journal of the American Chemical Society*, vol. 127, no. 23, pp. 8286–8287, 2005.
- [3] R. Asahi, T. Morikawa, T. Ohwaki, K. Aoki, and Y. Taga, "Visible-light photocatalysis in nitrogen-doped titanium oxides," *Science*, vol. 293, no. 5528, pp. 269–271, 2001.

- [4] G. Wang, D. Chen, H. Zhang, J. Z. Zhang, and J. H. Li, "Tunable photocurrent spectrum in well-oriented zinc oxide nanorod arrays with enhanced photocatalytic activity," *The Journal of Physical Chemistry C*, vol. 112, no. 24, pp. 8850–8855, 2008.
- [5] J. Bae, J. B. Han, X.-M. Zhang et al., "ZnO nanotubes grown at low temperature using gas catalysts and their enhanced photocatalytic activities," *Journal of Physical Chemistry C*, vol. 113, no. 24, pp. 10379–10383, 2009.
- [6] L. R. Zheng, Y. H. Zheng, C. Q. Chen et al., "Network structured SnO₂/ZnO heterojunction nanocatalyst with high photocatalytic activity," *Inorganic Chemistry*, vol. 48, no. 5, pp. 1819–1825, 2009.
- [7] W. Chen, N. Zhang, M. Y. Zhang, X. T. Zhang, H. Gao, and J. Wen, "Controllable growth of ZnO-ZnSe heterostructures for visible-light photocatalysis," *CrystEngComm*, vol. 16, no. 6, pp. 1201–1206, 2014.
- [8] B. Subash, B. Krishnakumar, B. Sreedhar, M. Swaminathan, and M. Shanthi, "Highly active WO₃-Ag-ZnO photocatalyst driven by day light illumination," *Superlattices and Microstructures*, vol. 54, no. 1, pp. 155–171, 2013.
- [9] J. Nayak, S. N. Sahu, J. Kasuya, and S. Nozaki, "CdS-ZnO composite nanorods: synthesis, characterization and application for photocatalytic degradation of 3,4-dihydroxy benzoic acid," *Applied Surface Science*, vol. 254, no. 22, pp. 7215–7218, 2008.
- [10] H. Zheng, J. Z. Ou, M. S. Strano, R. B. Kaner, A. Mitchell, and K. Kalantar-Zadeh, "Nanostructured tungsten oxide—properties, synthesis, and applications," *Advanced Functional Materials*, vol. 21, no. 12, pp. 2175–2196, 2011.
- [11] J. Xie, Z. Zhou, Y. Lian et al., "Simple preparation of WO₃-ZnO composites with UV-Vis photocatalytic activity and energy storage ability," *Ceramics International*, vol. 40, no. 8, pp. 12519–12524, 2014.
- [12] S.-M. Lam, J.-C. Sin, A. Z. Abdullah, and A. R. Mohamed, "ZnO nanorods surface-decorated by WO₃ nanoparticles for photocatalytic degradation of endocrine disruptors under a compact fluorescent lamp," *Ceramics International*, vol. 39, no. 3, pp. 2343–2352, 2013.
- [13] C. Yu, K. Yang, Q. Shu, J. C. Yu, F. Cao, and X. Li, "Preparation of WO₃/ZnO composite photocatalyst and its photocatalytic performance," *Chinese Journal of Catalysis*, vol. 32, no. 3-4, pp. 555–565, 2011.
- [14] Y. Wang, L. Cai, Y. Li, Y. Tang, and C. Xie, "Structural and photoelectrocatalytic characteristic of ZnO/ZnWO₄/WO₃ nanocomposites with double heterojunctions," *Physica E: Low-Dimensional Systems and Nanostructures*, vol. 43, no. 1, pp. 503–509, 2010.
- [15] S. Adhikari and D. Sarkar, "Hydrothermal synthesis and electrochromism of WO₃ nanocuboids," *RSC Advances*, vol. 4, no. 39, pp. 20145–20153, 2014.
- [16] S. Adhikari, D. Sarkar, and G. Madras, "Synthesis and photocatalytic performance of quasi-fibrous ZnO," *RSC Advances*, vol. 4, no. 99, pp. 55807–55814, 2014.
- [17] S. Wei, Z. Shao, X. Lu, Y. Liu, L. Cao, and Y. He, "Photocatalytic degradation of methyl orange over ITO/CdS/ZnO interface composite films," *Journal of Environmental Sciences*, vol. 21, no. 7, pp. 991–996, 2009.
- [18] J. Matos, J. Laine, and J. M. Hermann, "Synergy effect in the photocatalytic degradation of phenol on a suspended mixture of titania and activated carbon," *Applied Catalysis B: Environmental*, vol. 18, no. 3-4, pp. 281–291, 1998.
- [19] C. Chen, J. Weng, J. Chen et al., "Photocatalyst ZnO-doped Bi₂O₃ powder prepared by spray pyrolysis," *Powder Technology*, vol. 272, pp. 316–321, 2015.

Research Article

Preparation and Evaluation of Pralidoxime-Loaded PLGA Nanoparticles as Potential Carriers of the Drug across the Blood Brain Barrier

Washington Chigumira,¹ Prosper Maposa,¹ Louis L. Gadaga,¹ Admire Dube,² Dexter Tagwireyi,¹ and Charles C. Maponga¹

¹Drug and Toxicology Information Service (DaTIS), School of Pharmacy, College of Health Sciences, University of Zimbabwe, P.O. Box A 178, Avondale, Harare, Zimbabwe

²School of Pharmacy, University of Western Cape, Robert Sobukwe Road, Bellville 7535, South Africa

Correspondence should be addressed to Prosper Maposa; promaposa@gmail.com

Received 15 May 2015; Accepted 24 June 2015

Academic Editor: Anh-Tuan Le

Copyright © 2015 Washington Chigumira et al. This is an open access article distributed under the Creative Commons Attribution License, which permits unrestricted use, distribution, and reproduction in any medium, provided the original work is properly cited.

Pralidoxime is an organophosphate antidote with poor central nervous system distribution due to a high polarity. In the present study, pralidoxime-loaded poly(lactic-co-glycolic acid) nanoparticles were prepared and evaluated as a potential delivery system of the drug into the central nervous system. The nanoparticles were prepared using double emulsion solvent evaporation method. Poly(lactic-co-glycolic acid) (PLGA) in ethyl acetate made the organic phase and pralidoxime in water made the aqueous phase. The system was stabilized by polyvinyl alcohol. Different drug/polymer ratios were used (1:1, 1:2, and 1:4) and the fabricated particles were characterized for encapsulation efficiency using UV-VIS Spectroscopy; particle size distribution, polydispersity index, and zeta potential using photon correlation spectroscopy; and *in vitro* drug release profile using UV-VIS Spectroscopy. Mean particle sizes were 386.6 nm, 304.7 nm, and 322.8 nm, encapsulation efficiency was 28.58%, 51.91%, and 68.78%, and zeta potential was 5.04 mV, 3.31 mV, and 5.98 mV for particles with drug/polymer ratios 1:1, 1:2, and 1:4, respectively. *In vitro* drug release profile changed from biphasic to monobasic as the drug/polymer ratio decreased from 1:1 to 1:4. Stable pralidoxime-loaded PLGA nanoparticles were produced using double emulsion solvent evaporation techniques.

1. Introduction

Organophosphates (OP) intoxication accounts for the highest number of poisoning cases across the globe [1, 2]. It is estimated that about three million people are exposed to organophosphates each year, with up to three hundred thousand fatalities [1, 2]. Severe poisoning affects peripheral and central nervous systems and eventually causes paralysis of body extremities and respiratory muscle. The major cause of death in severe poisoning cases is respiratory failure due to depression of central nervous system (CNS) respiratory center, neuromuscular weakness (mainly the diaphragm muscle), and excessive bronchosecretions [3].

Despite the wide use of organophosphates [4] and high OP intoxication incidences worldwide [1], the management

of severe acute OP poisoning cases is still a challenge with the available drugs. Pralidoxime was reported to be of great benefit in reversing respiratory symptoms of OP poisoning [5] but its use is limited due to a poor blood brain barrier penetration [6]. Organophosphates, on the contrary, can freely pass the barrier resulting in various CNS poisoning effects. Improved CNS distribution of oximes can potentially improve the drug effectiveness in the management of organophosphate poisoning through reversal of the nicotinic and muscarinic receptor effects both peripherally and centrally.

Efforts to overcome the blood brain barrier (BBB) have focused on altering either the barrier integrity and characteristics or the drug properties. Nanoparticles might be a better technique to circumvent the BBB since no BBB or

drug manipulation is necessary. Poly(lactic-co-glycolic acid) PLGA nanoparticles have proved to improve the blood brain barrier penetration of a number of drugs that are poorly distributed in the CNS [7]. The current study is aimed at fabrication and analyses of pralidoxime-loaded PLGA nanoparticles, using different drug/polymer ratios, for potential use in the delivery of the drug into the central nervous system.

2. Materials and Methods

2.1. Materials. Pralidoxime chloride (pyridine-2-aldoxime methochloride) (RD grade), PLGA (50:50), ethyl acetate, and polyvinyl alcohol (PVA) were obtained from Sigma Aldrich Company, Germany. Disodium orthophosphate, citric acid, potassium dihydrogen orthophosphate, sodium hydroxide (NaOH), and sodium chloride (NaCl) were obtained from Associated Chemical Enterprise (South Africa). Distilled water was used in all the experiments. The following equipment was used during the study: pH meter (Jenway, UK), vortex mixer (Heidolph Reax 2000, Germany), magnetic stirring plate (Sigma Aldrich, Germany), sonicator (Westwood Ultrasonics, UK), ultracentrifuge (Beckman Optima LE-80k Ultracentrifuge, USA and Hermle Z160M, Germany), UV-VIS Spectrophotometer (Shimadzu, Japan), and Zetasizer (Malvern Zetasizer Nano ZS90, UK).

2.2. Fabrication of Pralidoxime-Loaded PLGA Nanoparticles. Pralidoxime-loaded PLGA nanoparticles were prepared using a double emulsion solvent evaporation method. 1.2 mL aqueous pralidoxime solution (25 mg/mL, 50 mg/mL, or 100 mg/mL) was emulsified in 8 mL of ethyl acetate containing PLGA (120 mg) by means of homogenization on an ice bath at a speed of 13000 rpm for 90 seconds. The primary emulsion was further emulsified in 32 mL of 2% (w/v) PVA solution containing 5% (w/v) of NaCl by homogenization at 25000 rpm for 10 minutes on an ice bath. The resultant double emulsion was stirred for 4 hours at 25°C on a magnetic stirring plate at 500 rpm. The nanoparticle suspension was then kept under refrigeration overnight. The nanoparticles were recovered by ultracentrifugation at 13,400 rpm for 30 minutes at 4°C. Following this, nanoparticle sediments were washed thrice with water then lyophilized overnight.

2.3. Encapsulation Efficiency. The nanoparticles were destroyed by acetonitrile in 1 mL eppendorf tubes under a vortex mixer, immediately after the washing step of fabrication (before lyophilization). The resultant solution was passed through a membrane filter (0.22 µm pore size) and the amount of pralidoxime contained in the destroyed nanoparticles was determined by a UV-VIS spectrophotometer at 263 nm. The amount of pralidoxime loaded in the nanoparticles was determined by measuring the amount of the drug encapsulated per mL of nanoparticle suspension,

TABLE 1: Encapsulation efficiency of pralidoxime-loaded PLGA nanoparticles with different drug/polymer ratios.

Drug/polymer ratio	Loading efficiency (mg/mL)	Encapsulation efficiency (%)
1:1	0.98	28.58 ± 0.01
1:2	0.89	51.91 ± 0.02
1:4	0.59	68.78 ± 0.03

Encapsulation efficiency is recorded as mean ± SD.

which was done in triplicates. Encapsulation efficiency was calculated according to the following formula:

$$\begin{aligned} & \text{Encapsulation Efficiency (EE)} \\ &= \frac{\text{Amt of pralidoxime entrapped}}{\text{total amt of pralidoxime added}} \times 100\%. \end{aligned} \quad (1)$$

2.4. Particle Size, Polydispersity Index, and Zeta Potential. The particle size distribution, polydispersity index, and zeta potential of the pralidoxime-loaded PLGA nanoparticles were determined in triplicates by a photon correlation spectroscopy (PCS) using a zetasizer (Malvern Zetasizer Nano ZS90, UK). Approximately, 1 mg of each sample was dissolved in 1 mL of deionized water. The dissolved sample was sonicated for 30 minutes. The samples were placed in a zetasizer and the particle size, polydispersity index, and zeta potential were then observed.

2.5. In Vitro Drug Release Analysis. The *in vitro* pralidoxime release from the PLGA nanoparticles was carried out at 37°C in simulated blood fluid (pH 7.4). The buffer solution was prepared according to the United States Pharmacopoeia (USP 2007). 1 mL phosphate buffer solution (pH 7.4) was placed in eppendorf tubes (containing the washed nanoparticle samples) sufficient for all the time points required. The eppendorf tubes were placed in a water bath at 37°C. The samples were withdrawn for analysis after 1.0, 2.0, 3.0, 4.0, 6.0, and 24.0 hours. The absorbance of the solutions was determined in triplicates by UV spectroscopy at 263 nm.

2.6. Analysis of Results. ANOVA was done on the results using GraphPad Prism 5. All the statistical tests were done at 95% level of significance.

3. Results

3.1. Encapsulation Efficiency. Nanoparticles with drug/polymer ratio of 1:4 had highest encapsulation efficiency (68.78%) and the encapsulation efficiency decreased with increase in drug/polymer ratio as illustrated in Table 1. The differences in encapsulation efficiency among nanoparticles with different drug/polymer ratios were statistically significant at 5% standard error ($P = 0.0001$ for all the combinations).

3.2. Particles Size and Polydispersity Index (PDI). The results for the particle size, polydispersity, and zeta potential are

TABLE 2: Mean particle size, polydispersity index (PDI), and zeta potential for pralidoxime-loaded PLGA nanoparticles with different drug : polymer ratio.

Drug/polymer ratio	Particle size (nm)	Zeta potential (mV)	PDI
1:1	386.6 ± 15.33	5.04 ± 0.35	0.323 ± 0.021
1:2	304.7 ± 7.167	3.31 ± 0.27	0.180 ± 0.032
1:4	322.8 ± 2.193	5.98 ± 0.30	0.203 ± 0.001

Data represented as mean ± SD.

shown in Table 2. The least mean particle size observed was 304.7 nm for the particles with drug/polymer ratio 1:2, followed by 322.8 nm for drug/polymer ratio 1:4 but the difference was statistically insignificant at 5% standard error ($P = 0.3540$). The particles with drug/polymer ratio 1:1 were the largest (386.6 nm) and statistically different from the others at 5% standard error ($P = 0.001$ for all the combinations).

Polydispersity index was less than 0.5 for all the three samples. The particles with drug/polymer ratios 1:2 and 1:4 had the least PDIs and their difference at 5% standard error was insignificant ($P = 0.2423$). The highest PDI value observed was (0.323 \bar{D}) for particles with drug/polymer ratio 1:1 and was significantly different from the other two values ($P = 0.0005$).

3.3. Zeta Potential. Zeta potential of the produced nanoparticles was significantly different among all the three samples at 5% standard error ($P = 0.001$, $P = 0.01$, and $P = 0.0001$ for the comparison of particles with drug/polymer ratios 1:1 and 1:2, 1:1 and 1:4, and 1:2 and 1:4, resp.). The highest zeta potential (5.98 mV) was observed for the particles with drug/polymer ratio 1:4 and the lowest value (3.31 mV) was observed for the particles with drug/polymer ratio 1:2.

3.4. In Vitro Drug Release. The drug release profile was biphasic for the sample with drug/polymer ratio 1:1. This then shifted towards monophasic as the drug/polymer ratio decreased to 1:4 (Figure 1).

4. Discussion

Drug encapsulation into nanoparticles modifies the drug's pharmacokinetics by masking its physicochemical properties. In turn, the nanoparticle characteristics determine the pharmacokinetics and stability of the drug. *In vitro* characterization of nanoparticles gives a prediction of a drug's pharmacokinetics in physiological fluids so as to improve its stability in a formulation.

High encapsulation efficiency observed for particles with drug/polymer ratio 1:4 (Table 1) is favorable. High encapsulation efficiency minimizes drug wastage during the fabrication process. It also ensures high drug concentration at the target site and increased drug residence time.

Other studies have however recorded that encapsulation efficiency of water soluble drugs can be as high as 80% to 100% when the double emulsion evaporation method is used [8].

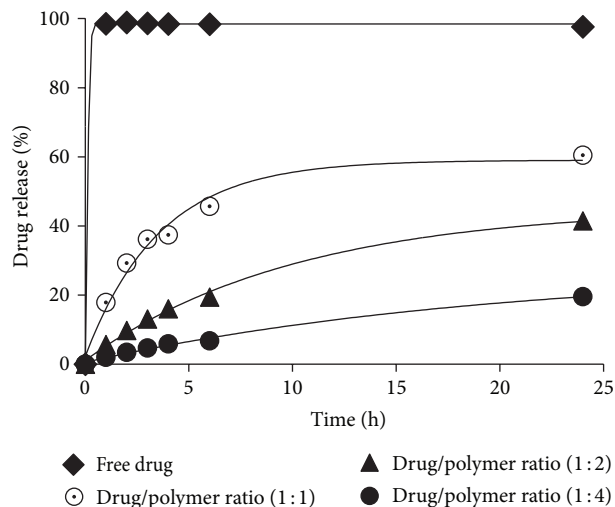


FIGURE 1: Graph of drug release profile of pralidoxime-loaded PLGA nanoparticles in comparison with the free drug.

The reduced encapsulation efficiency observed in this study (69.27%) can be attributed to low PLGA concentration in the dispersed phase [9]. This leads to a less viscous solution which leads to slow precipitation of the PLGA at the dispersed phase surface, resulting in increased drug diffusion across the phase boundary and low encapsulation consequently [9]. High pralidoxime solubility in water (the continuous phase) is also a factor that reduces encapsulation efficiency [10]. Other possible contributing factors include high PLGA solubility in ethyl acetate, low ratio of the dispersed phase to continuous phase (encapsulation efficiency increases with increase in the volume of the continuous phase), high stirring rate during fabrication in an effort to minimize the final particle size, and high PVA concentration which was used as an emulsifier [10, 11].

The decrease in encapsulation efficiency with increase in drug/polymer ratio was in line with the results of studies by Trivedi and colleagues [12] as well as Nagda and colleagues [11]. In high drug/polymer ratios, the polymer layer surrounding the drug molecules is thin; hence the drug can easily escape encapsulation before polymer solidification unlike in the presence of low drug/polymer ratio where the diffusion layer is thick.

Particle size is an important factor to consider in circumvention of the blood brain barrier. Small particles are of great interest as opposed to larger particles that would be trapped in the tight junctions [13]. Moreover, nanoparticles for central nervous system drug delivery should not have a higher tendency of aggregation. The degree of nanoparticle aggregation in a liquid medium can be determined by the polydispersity index, values close to zero being favorable as opposed to those close to one, which indicate a high degree of aggregation.

The particles produced for all the three samples with different drug/polymer ratios were small (in the nanometer range) and formed monodispersion in water; PDI < 0.5 (Table 2) means that there was a uniform size and shape

distribution for the particles in each sample. Monodispersion favors cellular uptake of the nanoparticles as opposed to aggregated particles (the presence of which can be shown by a high PDI) which interferes with it due to the big size.

Though cell membranes allow a free passage of particles less than 1 nm in diameter [14], because of their size, the nanoparticles can potentially enhance pralidoxime delivery into the central nervous system by increasing pralidoxime concentration inside or at the BBB cell luminal surface. Thus they create a higher concentration gradient between the blood and brain than the one obtainable after systemic administration of the free drug [15]. The drug's pharmacokinetics can also be altered to favor the central nervous system delivery by increased circulation time of the drug in the blood stream as systems such as mononuclear phagocyte system only tag and remove particles with a minimal diameter of 1 micrometer from the circulation [16]. *In vivo* studies might however be necessary to ascertain this.

Much smaller pralidoxime-loaded PLGA nanoparticles could be obtained. One of the reasons that could have resulted in the recorded particles size might be the shearing method used (homogenization) which was recorded to be associated with large particles [17]. The use of ultrasonication (using a probe sonicator) could have possibly resulted in even much smaller particles.

For the three samples with different drug/polymer ratios, zeta potential values were small (less than 20) (Table 2). The low values can be an indication of how the pralidoxime is encapsulated in PLGA nanoparticles, shielded in the polymer not adsorbed at the polymer surface [18]. Low zeta potential values are however associated with low stability of particles due to low electrostatic repulsive forces between the particles; consequently, the particles will have a high tendency of aggregating which in turn compromises the stability of the particles in a formulation [19].

On the contrary, small PDI values (close to zero) (Table 2) show that all the samples formed monodispersions in water, a scenario which is impossible in the presence of aggregating. This suggests that the particles were stable despite the low zeta potential values. Since PLGA is a large molecule (polymer), the stability could be more due to steric hindrance than surface charge [19]. Moreover, an adsorbed layer of a polymer or large molecular weight molecule tends to shift plane of shear further from the particle surface and, as a result, the measured zeta potential decreases [20]. This means that, even in the case of highly charged particles, a relatively low zeta potential value can be recorded.

The nature of the recorded zeta potential values (small and positively charged) can improve the pharmacokinetics of the drug by increasing the circulation time of the nanoparticles in the blood [21]. Negatively charged nanoparticles are quickly cleared from the blood stream by fixed macrophages of the reticuloendothelial system [22]. Likewise, highly surface charged particles are efficiently phagocytized by murine macrophages more than those with small charge [21].

For the drug to be released from the PLGA nanoparticles, the PLGA undergoes degradation by hydrolysis or biodegradation through cleavage of its backbone ester linkage into oligomers and finally monomers [23]. The clear biphasic

release profile of the sample with drug/polymer ratio 1:1 indicates the presence of pralidoxime close to or at the PLGA surface [24]. This accounts for the initial burst in drug release as the drug gets in contact with water. The rapid release is related to pralidoxime solubility and water penetration into the PLGA matrix [25]. Subsequently, the graph shows a delayed release profile. This can be attributed to the progressive pralidoxime release through the thicker pralidoxime depleted layer [25]. Water inside the drug matrix hydrolyses the PLGA into its oligomeric then monomeric soluble products [23]. The drug then freely passes and is released by erosion and diffusion until there is a complete PLGA solubilization. The biphasic release profile might be favourable since it can be used for controlled drug release.

The first phase (rapid release) is less pronounced for the sample with drug/polymer ratio 1:2. The delayed release phase is dominant. This indicates that there is little pralidoxime close to the PLGA surface [23]. For the sample with drug/polymer ratio 1:4, the initial rapid release phase is invisible on the graph (Figure 1). This shows that pralidoxime is completely shielded by PLGA and no drug molecules are close to the polymer surface. This type of drug release (monophasic but sustained) may be convenient to the patient as it reduces dosing frequency and increases compliance. However, it takes time before the onset of action is experienced, something undesirable in managing a poisoned patient. Therefore, a loading dose might be necessary in this case or initiating this drug in combination with another organophosphate antidote, for example, atropine.

5. Conclusion

The pralidoxime-loaded PLGA nanoparticles were produced by the double emulsion solvent evaporation method with the highest encapsulation efficiency being 68.78% (for particles with drug/polymer ratio 1:4), lowest mean particle size of 304.7 nm (from particles with drug/polymer ratio 1:2 though not statistically different from the size recorded by the particles with drug/polymer ratio 1:4), and the highest zeta potential being 5.98 mV (recorded for particles with drug/polymer ratio 1:4). The *in vitro* drug release changed from biphasic to monophasic from the drug/polymer ratios 1:1 to 1:4. Generally, the drug/polymer ratio 1:4 produced better results compared to the ratios 1:1 and 1:2.

Conflict of Interests

The authors declare that there is no conflict of interests regarding the publication of this paper.

Acknowledgments

The authors would like to thank technicians at the Western Cape University (South Africa) for assistance in the in particle size, PDI, and zeta potential characterization. The authors also acknowledge the following departments at the University of Zimbabwe for their laboratories and equipment: Department of Biochemistry, Department of Physiology, and Faculty of Veterinary Sciences. We also acknowledge the Innovation

and Commercialization (ICF) grant received for the purpose of developing this study.

References

- [1] Y. Li, C. Sun, Z. Qiu et al., "Clinical toxicology in China: current situation and future development," *Clinical Toxicology*, vol. 47, no. 4, pp. 263–269, 2009.
- [2] M. Eddleston, N. A. Buckley, P. Eyer, and A. H. Dawson, "Management of acute organophosphorus pesticide poisoning," *The Lancet*, vol. 371, no. 9612, pp. 597–607, 2008.
- [3] N. J. Secaucus and Occupational Health Services, *MSDS for Methyl Parathion*, OHS, 1991.
- [4] M. Balali-Mood and K. Balali-Mood, "Neurotoxic disorders of organophosphorus compounds and their managements," *Archives of Iranian Medicine*, vol. 11, no. 1, pp. 65–89, 2008.
- [5] G. M. Tush and M. I. Anstead, "Pralidoxime continuous infusion in the treatment of organophosphate poisoning," *Annals of Pharmacotherapy*, vol. 31, no. 4, pp. 441–444, 1997.
- [6] R. I. Ellyn and J. H. Wills, "Oximes antagonistic to inhibitors of cholinesterase," *Journal of pharmaceutical sciences*, vol. 53, pp. 995–1007, 1964.
- [7] Y. E. Choonara, V. Pillay, V. M. K. Ndesendo et al., "Polymeric emulsion and crosslink-mediated synthesis of super-stable nanoparticles as sustained-release anti-tuberculosis drug carriers," *Colloids and Surfaces B: Biointerfaces*, vol. 87, no. 2, pp. 243–254, 2011.
- [8] M. Iwata and J. W. McGinity, "Preparation of multi-phase microspheres of poly(D,L-lactic acid) and poly(D,L-lactic-co-glycolic acid) containing a W/O emulsion by a multiple emulsion solvent evaporation technique," *Journal of Microencapsulation*, vol. 9, no. 2, pp. 201–214, 1991.
- [9] H. Rafati, A. G. A. Coombes, J. Adler, J. Holland, and S. S. Davis, "Protein-loaded poly(DL-lactide-co-glycolide) microparticles for oral administration: formulation, structural and release characteristics," *Journal of Controlled Release*, vol. 43, no. 1, pp. 89–102, 1997.
- [10] R. C. Mehta, B. C. Thanoo, and P. P. DeLuca, "Peptide containing microspheres from low molecular weight and hydrophilic poly(D,L-lactide-co-glycolide)," *Journal of Controlled Release*, vol. 41, no. 3, pp. 249–257, 1996.
- [11] C. D. Nagda, N. P. Chotai, S. B. Patel, T. J. Soni, and U. L. Patel, "Preparation and in vitro evaluation of bioadhesive microparticulate system," *International Journal of Pharmaceutical Sciences and Nanotechnology*, vol. 1, no. 3, pp. 257–266, 2008.
- [12] P. Trivedi, A. Verma, and N. Garud, "Preparation and characterization of aceclofenac microspheres," *Asian Journal of Pharmaceutics*, vol. 2, no. 2, pp. 110–115, 2008.
- [13] J. Panyam, W.-Z. Zhou, S. Prabha, S. K. Sahoo, and V. Labhasetwar, "Rapid endo-lysosomal escape of poly(DL-lactide-co-glycolide) nanoparticles: implications for drug and gene delivery," *The FASEB Journal*, vol. 16, no. 10, pp. 1217–1226, 2002.
- [14] P. R. Lockman, R. J. Mumper, M. A. Khan, and D. D. Allen, "Nanoparticle technology for drug delivery across the blood brain barrier," *Drug Development and Industrial Pharmacy*, vol. 28, no. 1, pp. 1–13, 2002.
- [15] M. Masserini, "Nanoparticles for brain drug delivery," *ISRN Biochemistry*, vol. 2013, Article ID 238428, 18 pages, 2013.
- [16] R. L. McCall and R. W. Sirianni, "PLGA nanoparticles formed by single- or double-emulsion with vitamin E-TPGS," *Journal of Visualised Experiments*, vol. 82, Article ID e51015, pp. 1–8, 2013.
- [17] B. N. Fredricksen, *PLGA and PLA particles as vaccine delivery systems for Atlantic salmon [Ph.D. thesis]*, University of Tromsø, 2012.
- [18] N. Csaba, M. Garcia-Fuentes, and M. J. Alonso, "The performance of nanocarriers for transmucosal drug delivery," *Expert Opinion on Drug Delivery*, vol. 3, no. 4, pp. 463–478, 2006.
- [19] S. Honary and F. Zahir, "Effect of zeta potential on the properties of nano-drug delivery systems—a review (Part 2)," *Tropical Journal of Pharmaceutical Research*, vol. 12, no. 2, pp. 265–273, 2013.
- [20] F. Quaglia, L. Ostacolo, A. Mazzaglia, V. Villari, D. Zaccaria, and M. T. Sciortino, "The intracellular effects of non-ionic amphiphilic cyclodextrin nanoparticles in the delivery of anti-cancer drugs," *Biomaterials*, vol. 30, no. 3, pp. 374–382, 2009.
- [21] C. He, Y. Hu, L. Yin, C. Tang, and C. Yin, "Effects of particle size and surface charge on cellular uptake and biodistribution of polymeric nanoparticles," *Biomaterials*, vol. 31, no. 13, pp. 3657–3666, 2010.
- [22] M. K. Khan, S. S. Nigavekar, L. D. Minc et al., "In vivo biodistribution of dendrimers and dendrimer nanocomposites—implications for cancer imaging and therapy," *Technology in Cancer Research and Treatment*, vol. 4, no. 6, pp. 603–613, 2005.
- [23] H. K. Makadia and S. J. Siegel, "Poly Lactic-co-Glycolic Acid (PLGA) as biodegradable controlled drug delivery carrier," *Polymers*, vol. 3, no. 3, pp. 1377–1397, 2011.
- [24] L. C. Amann, M. J. Gandall, R. Lin, Y. Liang, and S. J. Siegel, "In vitro-in vivo correlations of scalable PLGA-risperidone implants for the treatment of schizophrenia," *Pharmaceutical Research*, vol. 27, no. 8, pp. 1730–1737, 2010.
- [25] M. Ramchandani and D. Robinson, "In vitro and in vivo release of ciprofloxacin from PLGA 50:50 implants," *Journal of Controlled Release*, vol. 54, no. 2, pp. 167–175, 1998.

Research Article

Gold Nanoparticles Increase PLK1-Specific Small Interfering RNA Transfection and Induce Apoptosis of Drug Resistance Breast Cancer Cells

Ying Tian,¹ Yunlei Zhang,¹ Jing Pan,¹ Nan Lu,¹ Shouju Wang,¹ and Guangming Lu^{1,2}

¹Department of Medical Imaging, Jinling Hospital, School of Medicine, Nanjing University, Nanjing 210002, China

²State Key Laboratory of Analytical Chemistry for Life Science, School of Chemistry and Chemical Engineering, Nanjing University, Nanjing 210093, China

Correspondence should be addressed to Shouju Wang; shouju.wang@gmail.com and Guangming Lu; cjr.luguangming@vip.163.com

Received 22 May 2015; Accepted 27 July 2015

Academic Editor: Anh-Tuan Le

Copyright © 2015 Ying Tian et al. This is an open access article distributed under the Creative Commons Attribution License, which permits unrestricted use, distribution, and reproduction in any medium, provided the original work is properly cited.

Drug resistance is a major barrier that limits the effectiveness of chemotherapies against breast cancer. Here, gold nanoparticles (GNPs) characterized by good dispersivity, high stability, low cytotoxicity, and simple synthesis were developed to deliver small interfering RNA (siRNA) against PLK1 (PLK1-siRNA) and overcome the drug resistance of breast cancer cells. Compared with the commonly used Lipofectamine 2000, GNPs showed higher PLK1-siRNA delivery efficiency and resulted in the remarkable gene silencing of *PLK1* in drug resistance breast cancer cells MCF-7/MDR1 with low cytotoxicity *in vitro*. Moreover, delivery of PLK1-siRNA by GNPs could cause 14.23% apoptosis of MCF-7/MDR1 cells, which was apparently higher than 11.01% apoptosis conducted by Lipofectamine 2000. In addition, GNPs showed strong X-ray attenuation coefficient, indicating the potential theranostic application of this system. Therefore, this study disclosed an important step in the use of GNPs as transfection vector of siRNA that will be of great benefit to gene therapy against drug resistant cancer.

1. Introduction

Breast cancer is the most common cancer in women worldwide which is expected to account for 29% of all new cancers among women in the near future [1, 2]. The currently used clinical methods in cancer treatment mainly include surgery, chemotherapy, radiation therapy, immunotherapy, and biologic therapy [3]. Efficient suppression of growth of tumors and their metastatic lesions is a vital factor for breast cancer therapy [4]. However, despite the remarkable progress in breast cancer treatment in the last decade, the appearance of drug resistance greatly decreases the prognosis and survival rate of cancers and leads to ~90% failure of chemotherapy treatment in patients with metastatic cancers [5, 6]. Therefore, new strategies to overcome the drug resistance of breast cancer and increase antitumor efficacy are urgently needed.

The most prominent gene involved in drug resistance is multidrug-resistant protein 1 (*MDR1*), encoding the drug

efflux transporter P-glycoprotein. The overexpression of *MDR1* makes cancer cells resistant to a wide range of chemotherapeutic drugs [7, 8]. Previous studies showed that the overexpression of oncogene polo-like kinase 1 (*PLK1*) could upregulate the transcriptional expression of activator protein 1, one of the most important transcription factors of DNA binding protein, resulting in elevation of its target *MDR1* [9]. *PLK1*, a serine/threonine protein kinase, plays a key role in cell proliferation. Its overexpression is closely related to poor prognosis in cancer treatment [10, 11]. Knock-down of *PLK1* gene by small interfering RNA (siRNA) could downregulate the expression of *MDR1* and induce apoptosis of cancer cells. This will greatly benefit the treatment of drug resistant breast cancers [12].

RNA interference (RNAi) as one of the most powerful methods for gene knockdown has shown its great potential application in cancer gene therapy [13, 14]. However, siRNA by itself is difficult to exert silencing function due to its

fast degradation in physiological environment and poor cell penetrability. A well-designed vector will greatly increase the therapeutic efficiency of siRNA [15]. Currently, kinds of vectors including liposomes, polymers, and peptides have been developed [16–18]. These vectors can protect siRNA from degradation and improve delivery efficiency. However, the clinical applications of these methods are hindered by their complicated procedure, potential toxicity, and inability for theranostic applications. Therefore, exploring new delivery vectors with the promising advantages will be greatly valuable to gene therapy [19–22].

Gold nanoparticles (GNPs) are featured with small size, good dispersivity, high stability, low cytotoxicity, and simple synthesis procedure [23, 24]. They have been proved as potential candidates in biomedical application. The surface of GNPs can be easily modified by oligonuclear acids, large biomolecules, or peptides to boost their cell uptake and facilitate drug-delivery [25]. Furthermore, gold has high atomic number and strong X-ray attenuation coefficient, making it favorable for developing X-ray imaging [26–28]. So, GNPs can be used as the agent for X-ray imaging and siRNA delivery. In this study, polyethylenimine (PEI) coated GNPs were used to transport the specific siRNA against *PLK1* (PLK1-siRNA) to conquer drug resistance of MCF-7/MDRI breast cancer cells.

The *in vitro* experiments showed that the GNPs could effectively transfer PLK1-siRNA into MCF-7/MDRI cells with little toxicity. The expression of PLK1 was downregulated after siRNA transfection when the weight ratio between GNPs and siRNA is 4, evaluated by western blot analysis. The terminal deoxynucleotidyl transferase-mediated dUTP nick end labeling (TUNEL) and flow cytometry assays further demonstrated that GNPs-siRNA transfection led to higher efficiency of apoptosis in MCF-7/MDRI cells, compared with Lipofectamine 2000. The enhanced X-ray attenuation intensities of GNPs-PEI were also confirmed by X-ray imaging, and this effect promptly increased with the rise of the concentration of gold. This work will be very valuable to further exploit the transfection methods of siRNA, promote gene therapy, and develop biological imaging for drug resistant cancers.

2. Materials and Methods

2.1. Materials. Polyethyleneimine (PEI, branched, Mw 25 000), II-mercaptoundecanoic acid (MUA), chloroauric acid ($\text{HAuCl}_4 \cdot 3\text{H}_2\text{O}$), and 3-(4,5-dimethylthiazol-2-yl)-2,5-diphenyltetrazolium bromide (MTT) were obtained from Sigma-Aldrich. Diethylpyrocarbonate (DEPC) water and Lipofectamine 2000 transfection kit were purchased from Invitrogen. Sodium citrate and dimethyl sulfoxide (DMSO) were got from the Shanghai Chemical Corp. (Shanghai, China). Paraformaldehyde and DAPI were provided by KeyGEN Biotech Co., Ltd. (Jiangsu, China). GelRed was purchased from Biotium Inc. (Hayward, California, USA). Anti-PLK1 antibody and anti-MDR1 antibody were obtained from Abcam Company (Cambridge, UK). Bovine serum albumin (BSA) was got from Amresco Company (Solon, Ohio, USA). *In situ* cell death detection kit was purchased from Roche Inc. (Indianapolis, Indiana, USA). Human

breast cancer cells (MCF-7) and human embryonic kidney (293T) cells were purchased from ATCC (Manassas, VA). Dulbecco's Modified Eagle Medium (DMEM), Opti-MEN I Reduced-Serum Medium (Opti-MEM), fetal bovine serum (FBS), trypsin, and penicillin/streptomycin were bought from Gibco/Life Technologies (Grand Island, New York, USA). The duplexed PLK1-siRNA with or without a Cy 5 fluorophore on the 5' end of the sense strand was purchased from Ribobio Co., Ltd. (Guangzhou, China).

2.2. Synthesis of GNPs-PEI. The GNPs seed solution was prepared by adding 3 mL of 1% sodium citrate solution to 100 mL of boiling 1.0 mM HAuCl_4 solution under vigorous stirring until the transparent solution changed to dark red. The solution cooled to room temperature (RT) before use. Next, 20 μL of 20 mM MUA was added to 10 mL GNPs solution and kept stirring for 1 h at RT. Then the GNPs were purified by centrifugation for two times and dispersed in 10 mL water. The aqueous solution was mixed slowly with 1 mL of 10 mg/mL PEI and stirred at RT for 2 h. After stirring, the GNPs-PEI solution was adjusted to pH 7.0 and centrifuged for two times to purify before use.

2.3. Cell Culture. Human breast cancer cells (MCF-7), human embryonic kidney cells (293T), and drug resistant breast cancer cells (MCF-7/MDRI) were all cultured in DMEM with 10% FBS and 1% penicillin/streptomycin in a humidified incubator at 37°C under 5% CO_2 atmosphere with 95% relative humidity. The drug resistant cell line MCF-7/MDRI was established from MCF-7 cells through doxorubicin selection.

2.4. Preparation of PLK1-siRNA. The inhibitory effect of siRNA on the expression of PLK1 gene was tested. The sequence of PLK1-siRNA were 5'-UGAAGAAGAUCA-CCCUCUUA-3', 5'-GGCAACCAAAGUCGAAUUAU-3', 5'-GUCUCAAGGCCUCCUAAUA-3', and 5'-GAUCAC-CCUCCUAAAUAU-3'. Firstly, MCF-7/MDRI cells were cultured (2.5×10^6 cells per well) on a 6-well plate until the confluence reached ~90%. Lipofectamine 2000 (10 μL) was diluted in 250 μL Opti-MEM and incubated for 5 min and then was mixed with 4 μg PLK1-siRNA diluted in 250 μL Opti-MEM for 30 min at room temperature. After 6 h of incubation, the transfection solution was discarded and replaced with fresh DMEM for another 24 h. Cell apoptosis was determined by the *in situ* cell death detection kit according to the manufacturer's instruction. Images of cell apoptosis under the effect of PLK1-siRNA were recorded by a fluorescence microscope (Olympus IX71, Japan) equipped with fluorescent filter sets (excitation, 450–500 nm; emission, 515–565 nm).

2.5. PLK1-siRNA Binding to GNPs-PEI. GNPs-PEI was mixed with siRNA (20 mM) and incubated for 15 min at room temperature. To evaluate the siRNA binding ability, various weight ratios between GNPs and siRNA (0 to 4) were mixed and visualized on 1% (w/v) agarose gel containing 0.01% (v/v) GelRed. The electrophoresis was carried out for 15 min at a constant voltage of 100 V in buffer. The siRNA bands were

differentiated using a Tanon UV Gel Image System (Shanghai, China).

2.6. Characterization of GNPs, GNPs-PEI, and GNPs-siRNA. The sizes and morphologies of the GNPs were characterized by transmission electron microscopy (TEM) using a JEOL JEM-2100 microscope (Japan) at 200 kV. The absorbance spectra of GNPs, GNPs-PEI, and GNPs-siRNA were recorded through a UV/VIS spectrometer Lambda 35 (PerkinElmer, USA). The surface charge and the diameter of the samples in water were obtained via a ZetaPALS Analyzer (Brookhaven, USA). About 1 mL aqueous solution of GNPs-PEI with different weight (35–280 μg) was prepared for X-ray imaging through an IVIS Lumina XR (Xenogen Corporation-Caliper, Alameda, CA, USA). And the X-ray intensity ratio between the signal area of GNPs-PEI and the background area was calculated by analysis software.

2.7. Cytotoxicity Assay. MTT assay was employed to test the cytotoxicity of GNPs-PEI against breast cancer cells and normal cells. MCF-7/MDR1 breast cancer cells and 293T normal cells were seeded (1×10^4 cells per well) in a 96-well plate, respectively, until the confluence reached $\sim 70\%$. Then the cells were incubated with different weights of GNPs (0–1.6 μg) for 24 h and 48 h at 37°C . Next, the medium was replaced by 200 μL medium with 20 μL MTT (5 mg/mL) solution. The cells were incubated for additional 4 h and diluted in 150 μL dimethyl sulfoxide (DMSO) to dissolve the blue formazan crystals. The absorbance at 570 nm for each well was recorded by an automated microplate reader (BioTek, Winooski, Vermont, USA) to calculate the viability of cells.

2.8. Cellular Uptake Test. Breast cancer cells MCF-7/MDR1 were cultured (5×10^4 cells per well) in a 24-well plate with cover slips and incubated at 37°C with 5% CO_2 for 24 h. The cells on the cover slips were incubated with Lipofectamine 2000 bearing Cy 5 fluorescence-labeling siRNA for 4 h and 24 h. As parallel groups, the cells were treated with GNPs-siRNA (weight ratio = 1) for 4 h and 24 h. Finally, MCF-7/MDR1 cells were washed and fixed in 4% paraformaldehyde and then stained with DAPI for nucleus imaging. After washing again, the cover slips were mounted and observed using an Olympus Fluoview FV10i (Olympus Instruments, Tokyo, Japan).

2.9. Western Blot Analysis. MCF-7 and MCF-7/MDR1 cells were transfected with PLK1-siRNA using Lipofectamine 2000 and GNPs delivery vehicles as above described. After that, the cells were lysed on ice and centrifuged at 4°C for 5 min. About 10 μL of the supernatants was used for protein quantitative analysis through Bradford assay (Bio-Rad, USA). The remaining mixtures were mixed with Laemmli's buffer and held at 95°C for 10 min for protein denaturation. Next, after separating proteins in the SDS-PAGE gel, they were electroblotted to a hydrophobic polyvinylidene difluoride (PVDF) membrane, and the membranes were blocked in buffer containing 5% (w/v) nonfat dry milk. After washing,

membranes were incubated with primary antibody PLK1 (1 : 1000) and GAPDH (1 : 1000) overnight at 4°C , respectively, followed by washing and incubation with secondary antibody for 1 h at RT. The signals of the membrane were recorded by DAB coloration after washing again. Finally, immunoreactive bands were visualized and quantified using ImageJ software.

2.10. Cell Apoptosis Assay. The PLK-siRNA mediated apoptosis of MCF-7/MDR1 cells was tested by the *in situ* cell death detection kit of Roche and flow cytometry (FCM) after siRNA transfection using Lipofectamine 2000 or GNPs delivery vehicles. Firstly, MCF-7/MDR1 cells were cultured (2.5×10^6 cells per well) on a 6-well plate until the confluence reached $\sim 90\%$. The mixtures of Lipofectamine 2000 (10 μL) with PLK1-siRNA (4 μg) and GNPs (4 μg) carrying PLK1-siRNA (4 μg) were added into wells and incubated for 24 h. Cells without any treatment were used as control. Subsequently, the cells were harvested and stained with annexin V/FITC and PI according to the instructions. The apoptotic cells were recorded by a fluorescence microscope and a FACSCalibur flow cytometer (Becton, Dickinson and Company, Franklin Lakes, New Jersey, USA).

2.11. Statistical Analysis. All statistical comparisons were performed using Student's *t*-test. Data was expressed as mean \pm SD. A two-sided *P* value of less than 0.05 was considered statistically significant in all of the statistical tests.

3. Results and Discussion

3.1. PLK1-Specific siRNA Induced Apoptosis of MCF-7/MDR1 Cells. Four different specific siRNAs were chosen to silence *PLK1* expression through the widely used Lipofectamine 2000. The possible apoptosis of the treated cells was analyzed by TUNEL assay. As shown in Figure 1, annexin V/FITC labeling MCF-7/MDR1 cells exhibited strong green color after transfection by the Lipofectamine 2000 carrying PLK1-siRNA. This demonstrated that the PLK1-siRNA could effectively induce apoptosis of MCF-7/MDR1 cells. Moreover, cells after treatment by siRNA-4 showed more apoptotic cells than other siRNAs. Therefore, PLK1-specific siRNA-4 was a perfect candidate to evaluate the transfection efficiency of GNPs.

3.2. Morphology and Characteristics of GNPs, GNPs-PEI, and GNPs-siRNA. Polyethyleneimine (PEI) has been known to be a gene delivery vector because of its high buffering capacity to enhance the endosome escape of nucleic acid. In this study, PEI was functionalized with GNPs to deliver siRNA, which could condense and protect RNA from high cellular internalization. The binding capability of siRNA to GNPs is a key factor to silence *PLK1* gene in MCF-7/MDR1 cells. Therefore, different weight ratios between GNPs and siRNA were evaluated by gel retardation assay. As shown in Figure 2(a), the migration of siRNA was gradually retarded as the weigh ratios between GNPs and siRNA increased, compared with free siRNA. The band completely disappeared from the gel when the weight ratio became 1 : 1. This weight ratio was chosen for the following characterization of GNPs.

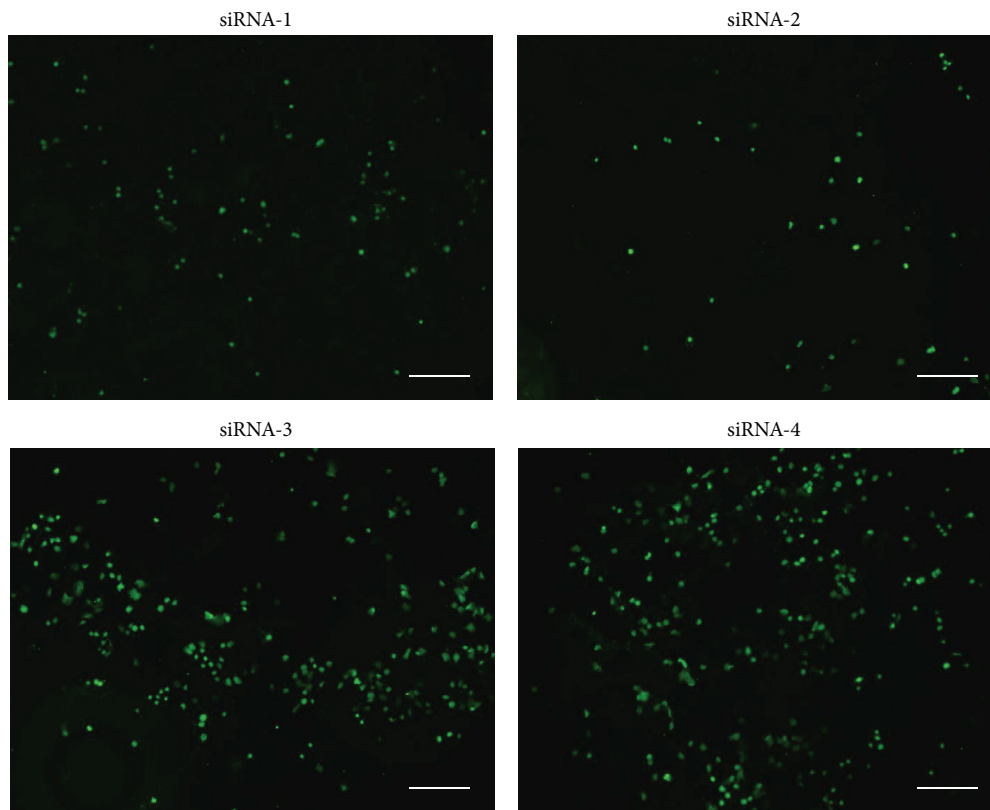


FIGURE 1: PLK1-specific siRNAs induced apoptosis of MCF-7/MDR1 cells. Cells were incubated with four different Lipofectamine 2000-siRNAs for 24 h and evaluated by TUNEL assay. Scale bars: 100 μm .

This also indicated the high binding efficiency of siRNA to GNPs. The GNPs would be an ideal carrier for RNA delivery.

The morphologies and sizes of GNPs were observed by TEM. Figure 2(b) showed that GNPs exhibited excellent dispersivity and spherical structure with an average diameter of ~ 20 nm. As shown in Figure 2(c), GNPs, GNPs-PEI, and GNPs-siRNA displayed broad plasmon spectra peaked at ~ 520 nm due to the surface plasmon resonance (SPR) of gold, which indicated that siRNA was successfully loaded onto the surface of gold under the assistance of PEI but slightly influenced the absorbance value of particles. The zeta potential of the nanoparticles exhibited positive charge at 36.70 ± 3.00 mV and 38.12 ± 2.23 mV, due to the PEI modification, but showed negative charge at -34.33 ± 1.03 mV before modification (Figure 2(d)). The dynamic light scattering (DLS) assay demonstrated that the hydrodynamic sizes of GNPs-PEI and GNPs-siRNA were 52.7 ± 0.7 nm and 54.3 ± 0.7 nm, respectively, which were higher than unmodified GNPs (29.7 ± 0.7) (Figure 2(e)).

Gold has large atomic number and strong X-ray attenuation coefficient, making it favorable for X-ray imaging. Figure 2(f) showed that the X-ray attenuation intensities of GNPs-PEI increased as the rise of gold concentrations. At higher concentration ($280 \mu\text{g}$), the X-ray intensity ratio of GNPs-PEI could exceed 4. The results revealed that

GNPs-PEI could strengthen the X-ray attenuation intensities in a concentration-dependent way, indicating the potential theranostic application of this siRNA delivery system.

3.3. Cytotoxicity of GNPs against MCF-7/MDR1 Cancer Cells and 293T Normal Cells. The toxicity of nanoparticles is a vital factor for their clinical translation application. Here, the biocompatibility of GNPs-PEI was determined by treating MCF-7/MDR1 breast cancer cells and 293T normal cells with different weights of GNPs-PEI. The MTT results showed that the weight of gold (from $0.1 \mu\text{g}$ to $1.6 \mu\text{g}$) did not affect the proliferation of the cells. The viability of cancer cells and normal cells totally surpassed 90% after 24 h and 48 h incubation with GNPs-PEI (Figure 3). This indicated that the PEI-modified gold nanoparticles were not toxic to both cancer and normal cells and exhibited well biocompatibility.

3.4. Cellular Uptake Study. Confocal laser scanning microscopy was used to evaluate the transfection of siRNA into cells conducted by Lipofectamine 2000/GNPs after incubation for 4 h and 24 h. It was observed that the GNPs-siRNA labeled with Cy 5 (red) entered MCF-7/MDR1 cells and was distributed in cytoplasm around the nucleus after 4 h treatment, but not Lipofectamine 2000-siRNA

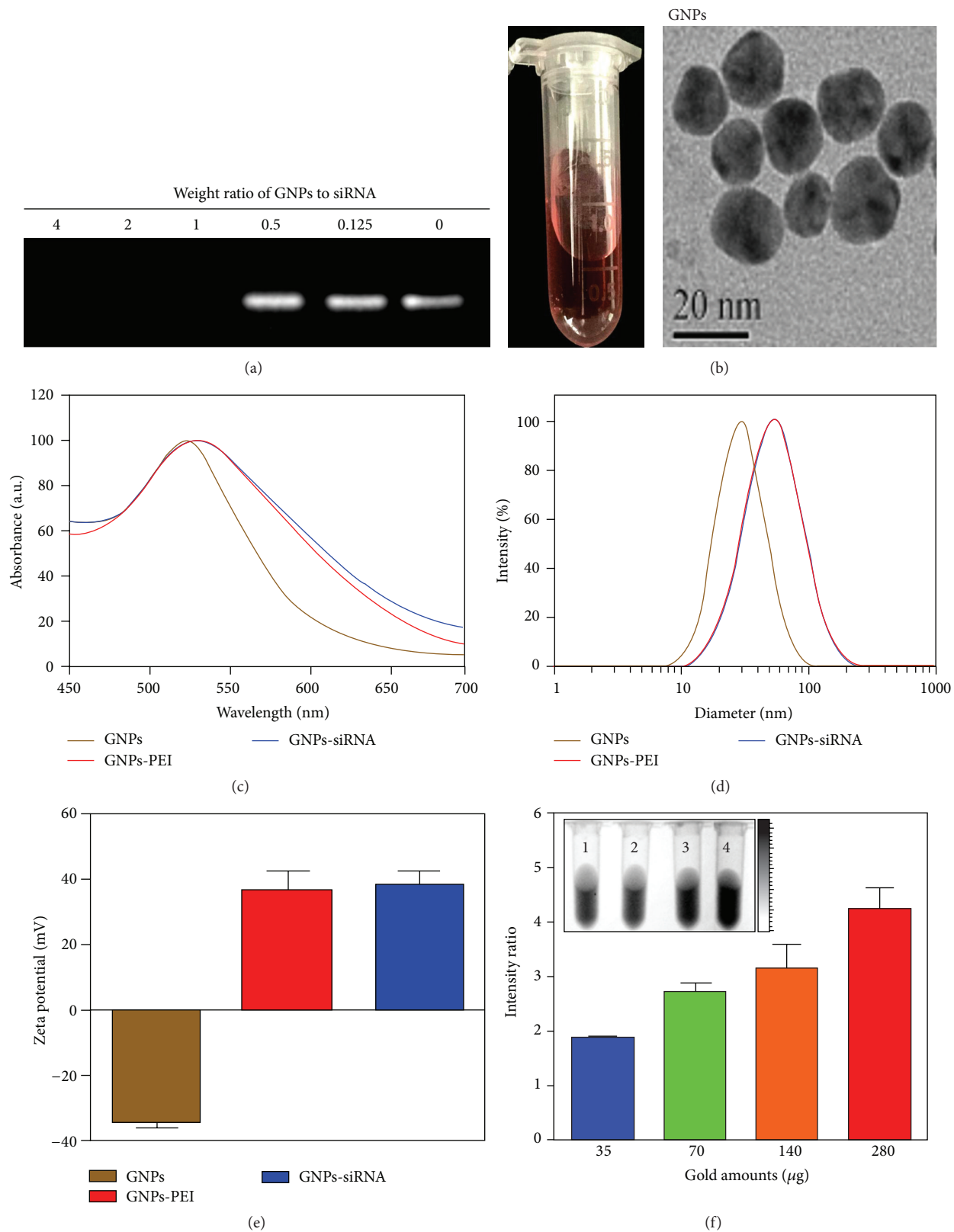


FIGURE 2: (a) Gel retardation assay of GNP-siRNA. Lanes from left to right indicate different weight ratios (4, 2, 1, 0.5, and 0.125) between GNPs and siRNA. The 0 weight ratio stands for free siRNA. (b) TEM images of GNP-siRNA conjugates. Scale bars: 20 nm. (c) UV-VIS spectra of GNPs, GNP-PEI, and GNP-siRNA from 450 to 700 nm. (d) Zeta potential of GNPs, GNP-PEI, and GNP-siRNA. (e) Diameters of GNPs, GNP-PEI, and GNP-siRNA. (f) X-ray images and intensity ratios of GNP-PEI with different weights (1: 35 μg , 2: 70 μg , 3: 140 μg , and 4: 280 μg).

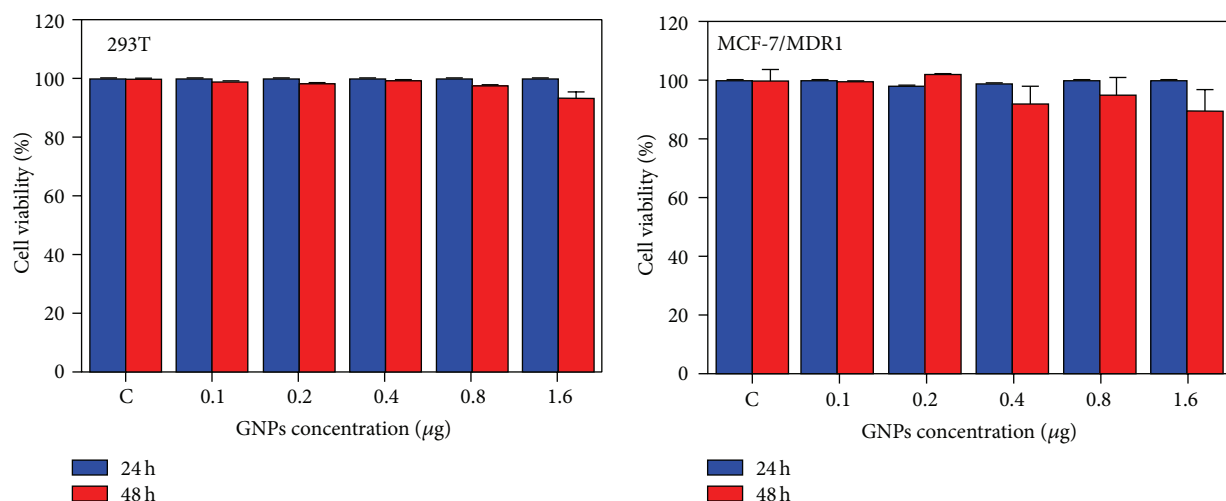


FIGURE 3: Cell viability of 293T cells and MCF-7/MDR1 cells after incubation with GNPs-PEI at different weights for 24 h and 48 h.

(Figure 4). At 24 h, the GNPs-siRNA treated group showed higher red fluorescence intensities, and the intensity of GNPs-siRNA treated group was conspicuously stronger than Lipofectamine 2000-siRNA group. The result clearly demonstrated that the transfection of siRNA conducted by GNPs was in a time-dependent manner and showed higher efficiency than the commonly used Lipofectamine 2000. This indicated that GNPs-based RNA delivery system had potential to be used in gene therapy.

3.5. GNPs-siRNA Transfection Restrained the Expression of *PLK1* Gene. To further investigate the knockdown efficiency of GNPs-siRNA, the expression of the siRNA targeting gene-*PLK1* was analyzed by western blot. The high expression of *PLK1* protein generally concerns the proliferation of malignant cells. The results showed that MCF-7/MDR1 drug resistant breast cancer cells had more *PLK1* protein than MCF-7 cancer cells (Figure 5). Compared with the control, there was almost no change of *PLK1* band in GNPs-treated group. However, the protein level of *PLK1* obviously decreased in the cells after treatment by Lip-siRNA and GNPs-siRNA at different weights, especially the weight of 4 between GNPs and siRNA. The amount of *PLK1* protein in MCF-7/MDR1 cells reduced almost 49% and 81% after treatment with Lipofectamine and GNPs, respectively (Figure 5). This indicated that GNPs-mediated transfection of siRNA resulted in significant inhibition of *PLK1* gene expression in MCF-7/MDR1 cells, and it was more efficient than Lipofectamine 2000. The results indicated that GNPs-siRNA was suitable for the delivery of siRNA and could efficiently downregulate its targeting genes.

3.6. GNPs-siRNA Transfection Induced Apoptosis of MCF-7/MDR1 Cells. *PLK1* is closely related to cell division and apoptosis. The downregulation of *PLK1* could induce apoptosis of drug resistance cells. Therefore, TUNEL assay and

flow cytometry were employed to evaluate the apoptosis of MCF-7/MDR1 cells after treatment by GNPs-siRNA. In TUNEL assay, both GNPs-siRNA and Lip-siRNA resulted in apoptosis of MCF-7/MDR1 cells, compared with the control group (Figure 6(a)). However, GNPs-siRNA treated group showed more apoptotic cells than Lip-siRNA by comparing the green fluorescence images (apoptotic cells) with the images (total cells) taken under the bright field. The flow cytometry test further confirmed that GNPs-siRNA and Lip-siRNA could induce apoptosis of MCF-7/MDR1 cells, and the apoptosis rates got to 14.23% and 11.01% after 24 h incubation, respectively, while there was only 1.71% apoptosis of cells in the control group (Figure 6(b)). Apoptosis rate was closely related to the amounts of *PLK1*-siRNA in the cells. This meant that GNPs could deliver more *PLK1*-specific siRNA into the cells than Lipofectamine 2000. The assay provided convincing evidence that GNPs-siRNA was a favorable vector for siRNA delivery and would greatly benefit the gene therapy for cancer.

4. Conclusions

In this study, PEI-capped GNPs efficiently delivered *PLK1*-specific siRNA into the drug resistance MCF-7/MDR1 breast cancer cells and showed higher transfection efficiency than the commercial kit Lipofectamine 2000. The transfection of *PLK1*-specific siRNA into cells not only silenced its targeting genes but also induced apoptosis of the drug resistant breast cancer cells. It was worth noting that exclusive GNPs were not toxic to normal/cancer cells. Importantly, the GNPs could be visualized by X-ray imaging in a concentration-dependent manner because of the excellent properties of gold. Overall, this work disclosed the great potential of GNPs as the excellent delivery system in gene therapy for drug resistance cancers and the further application of X-ray imaging.

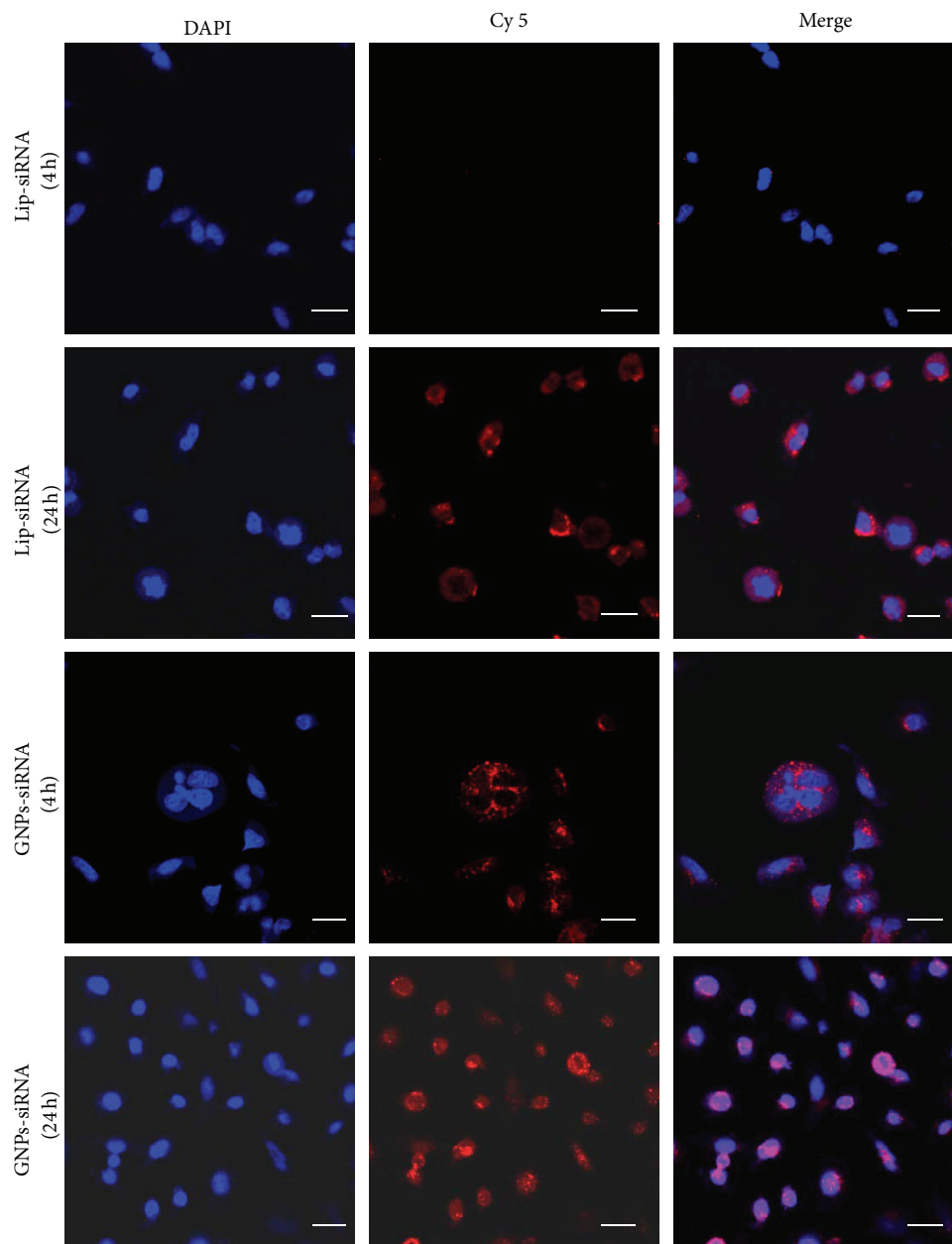


FIGURE 4: Internalization of Lipofectamine 2000-siRNA (Lip-siRNA) and GNPs-siRNA (the weight ratio was 1) by MCF-7/MDR1 cells after 4 h and 24 h incubation. DAPI (blue) stains cell nuclei and Cy 5 (red) indicates siRNA. Scale bars: 20 μm .

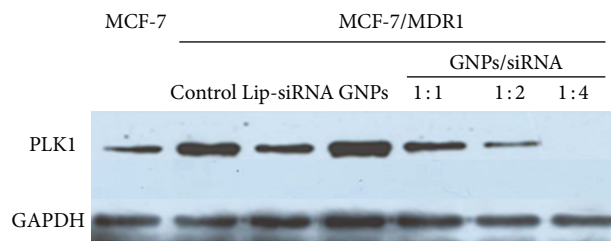


FIGURE 5: Western blot analysis of PLK1 expression in MCF-7/MDR1 and MCF-7 cells. MCF-7/MDR1 and MCF-7 cells were incubated with Lipofectamine 2000-siRNA (Lip-siRNA), GNPs alone, and GNPs-siRNA with different weight ratios for 24 h.

Conflict of Interests

The authors declare that there is no conflict of interests regarding the publication of this paper.

Acknowledgments

This project was financially supported by the National Key Basic Research Program of China (2014CB744504), the Major International (Regional) Joint Research Program of China (81120108013), the National Natural Science Foundation of China (81201175, 81371611, 81471632, 81401469, and U1332117),

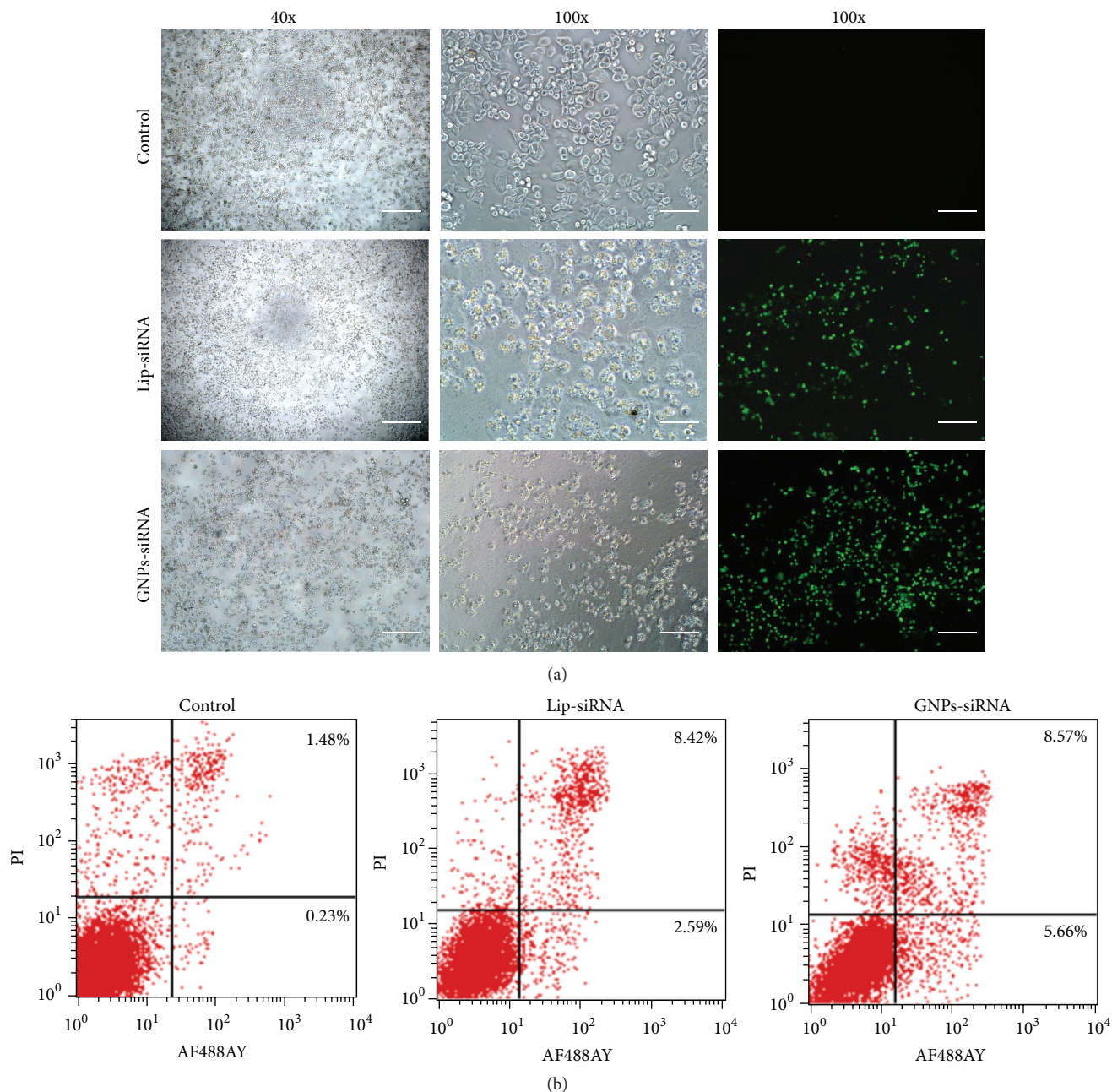


FIGURE 6: Apoptosis analysis of MCF-7/MDR1 cells after treatment by Lipofectamine 2000-siRNA (Lip-siRNA) and GNPs-siRNA. (a) TUNEL assay. Scale bars: 200 μm (40x) and 100 μm (100x). (b) Flow cytometry assay.

and the Natural Science Foundation of Jiangsu Province (BK20130863).

References

- [1] R. Siegel, J. Ma, Z. Zou, and A. Jemal, "Cancer statistics, 2014," *CA: A Cancer Journal for Clinicians*, vol. 64, no. 1, pp. 9–29, 2014.
- [2] L. Fan, K. Strasser-Weippl, J.-J. Li et al., "Breast cancer in China," *The Lancet Oncology*, vol. 15, no. 7, pp. e279–e289, 2014.
- [3] A. Schroeder, D. A. Heller, M. M. Winslow et al., "Treating metastatic cancer with nanotechnology," *Nature Reviews Cancer*, vol. 12, no. 1, pp. 39–50, 2012.
- [4] G. L. David, S. Yegnasubramanian, A. Kumar et al., "MDR1 promoter hypermethylation in MCF-7 human breast cancer cells: changes in chromatin structure induced by treatment with 5-aza-cytidine," *Cancer Biology & Therapy*, vol. 3, no. 6, pp. 540–548, 2004.
- [5] C. F. Higgins, "Multiple molecular mechanisms for multidrug resistance transporters," *Nature*, vol. 446, no. 7137, pp. 749–757, 2007.

- [6] D. B. Longley and P. G. Johnston, "Molecular mechanisms of drug resistance," *The Journal of Pathology*, vol. 205, no. 2, pp. 275–292, 2005.
- [7] S. Labialle, L. Gayet, E. Marthinet, D. Rigal, and L. G. Baggetto, "Transcriptional regulation of the human MDR1 gene at the level of the inverted MED-1 promoter region," *Annals of the New York Academy of Sciences*, vol. 973, pp. 468–471, 2002.
- [8] M. M. Gottesman, T. Fojo, and S. E. Bates, "Multidrug resistance in cancer: role of ATP-dependent transporters," *Nature Reviews Cancer*, vol. 2, no. 1, pp. 48–58, 2002.
- [9] B. Song, X. S. Liu, S. J. Rice et al., "Plk1 phosphorylation of Orc2 and Hbo1 contributes to gemcitabine resistance in pancreatic cancer," *Molecular Cancer Therapeutics*, vol. 12, no. 1, pp. 58–68, 2013.
- [10] K. Strebhardt and A. Ullrich, "Targeting polo-like kinase 1 for cancer therapy," *Nature Reviews Cancer*, vol. 6, no. 4, pp. 321–330, 2006.
- [11] Y. Hikichi, K. Honda, K. Hikami et al., "TAK-960, a novel, orally available, selective inhibitor of polo-like kinase 1, shows broad-spectrum preclinical antitumor activity in multiple dosing regimens," *Molecular Cancer Therapeutics*, vol. 11, no. 3, pp. 700–709, 2012.
- [12] J. R. Jackson, D. R. Patrick, M. M. Dar, and P. S. Huang, "Targeted anti-mitotic therapies: can we improve on tubulin agents?" *Nature Reviews Cancer*, vol. 7, no. 2, pp. 107–117, 2007.
- [13] E. Herrera-Carrillo and B. Berkhout, "Gene therapy strategies to block HIV-1 replication by RNA interference," in *Gene Therapy for HIV and Chronic Infections*, vol. 848 of *Advances in Experimental Medicine and Biology*, pp. 71–95, Springer, New York, NY, USA, 2015.
- [14] C. Lei, Y. Cui, L. Zheng, P. Kah-Hoe Chow, and C.-H. Wang, "Development of a gene/drug dual delivery system for brain tumor therapy: potent inhibition via RNA interference and synergistic effects," *Biomaterials*, vol. 34, no. 30, pp. 7483–7494, 2013.
- [15] J. Han, Q. Wang, Z. Zhang, T. Gong, and X. Sun, "Cationic bovine serum albumin based self-assembled nanoparticles as siRNA delivery vector for treating lung metastatic cancer," *Small*, vol. 10, no. 3, pp. 524–535, 2014.
- [16] L. N. Borgheti-Cardoso, L. V. Depieri, H. Diniz et al., "Self-assembling gelling formulation based on a crystalline-phase liquid as a non-viral vector for siRNA delivery," *European Journal of Pharmaceutical Sciences*, vol. 58, no. 1, pp. 72–82, 2014.
- [17] A. Petrelli, R. Carollo, M. Cargnelutti et al., "By promoting cell differentiation, miR-100 sensitizes basal-like breast cancer stem cells to hormonal therapy," *Oncotarget*, vol. 6, no. 4, pp. 2315–2330, 2015.
- [18] Z. Yang, B. Xiang, D. Dong, Z. Wang, J. Li, and X. Qi, "Dual receptor-specific peptides modified liposomes as VEGF siRNA vector for tumor-targeting therapy," *Current Gene Therapy*, vol. 14, no. 4, pp. 289–299, 2014.
- [19] S. Acharya and R. A. Hill, "High efficacy gold-KDEL peptide-siRNA nanoconstruct-mediated transfection in C2C12 myoblasts and myotubes," *Nanomedicine: Nanotechnology, Biology, and Medicine*, vol. 10, no. 2, pp. 329–337, 2014.
- [20] D. Heinemann, M. Schomaker, S. Kalies et al., "Gold nanoparticle mediated laser transfection for efficient siRNA mediated gene knock down," *PLoS ONE*, vol. 8, no. 3, Article ID e58604, 2013.
- [21] Y. Tian, J. Sun, H. Yan et al., "A rapid and convenient method for detecting a broad spectrum of malignant cells from malignant pleuroperitoneal effusion of patients using a multifunctional NIR heptamethine dye," *Analyst*, vol. 140, no. 3, pp. 750–755, 2015.
- [22] O. S. Muddineti, B. Ghosh, and S. Biswas, "Current trends in using polymer coated gold nanoparticles for cancer therapy," *International Journal of Pharmaceutics*, vol. 484, no. 1–2, pp. 252–267, 2015.
- [23] S. Wang, Z. Teng, P. Huang et al., "Reversibly extracellular pH controlled cellular uptake and photothermal therapy by pegylated mixed-charge gold nanostars," *Small*, vol. 11, no. 15, pp. 1801–1810, 2015.
- [24] L. Nie, S. Wang, X. Wang et al., "In vivo volumetric photoacoustic molecular angiography and therapeutic monitoring with targeted plasmonic nanostars," *Small*, vol. 10, no. 8, pp. 1585–1593, 2014.
- [25] P. Huang, L. Bao, C. Zhang et al., "Folic acid-conjugated silica-modified gold nanorods for X-ray/CT imaging-guided dual-mode radiation and photo-thermal therapy," *Biomaterials*, vol. 32, no. 36, pp. 9796–9809, 2011.
- [26] H. Ke, X. Yue, J. Wang et al., "Gold nanoshelled liquid perfluorocarbon nanocapsules for combined dual modal ultrasound/ct imaging and photothermal therapy of cancer," *Small*, vol. 10, no. 6, pp. 1220–1227, 2014.
- [27] Y. Tian, S. Luo, H. Yan et al., "Gold nanostars functionalized with amine-terminated PEG for X-ray/CT imaging and photothermal therapy," *Journal of Materials Chemistry B*, vol. 3, no. 21, pp. 4330–4337, 2015.
- [28] D. Kim, Y. Y. Jeong, and S. Jon, "A drug-loaded aptamer—gold nanoparticle bioconjugate for combined CT imaging and therapy of prostate cancer," *ACS Nano*, vol. 4, no. 7, pp. 3689–3696, 2010.

Research Article

Remineralizing Efficacy of Fluorohydroxyapatite Gel on Artificial Dentinal Caries Lesion

Qianqian Wang,¹ Shize Liu,² Xuejun Gao,³ Yan Wei,¹ Xuliang Deng,^{1,4}
Haifeng Chen,² and Xuehui Zhang^{1,5}

¹Department of Geriatric Dentistry, Peking University School and Hospital of Stomatology, Beijing 100081, China

²Department of Biomedical Engineering, College of Engineering, Peking University, Beijing 100081, China

³Department of Cariology and Endodontology, Peking University School and Hospital of Stomatology, Beijing 100081, China

⁴National Engineering Laboratory for Digital and Material Technology of Stomatology, Beijing 100081, China

⁵Department of Dental Materials, Peking University School and Hospital of Stomatology, Beijing 100081, China

Correspondence should be addressed to Haifeng Chen; haifeng.chen@pku.edu.cn and Xuehui Zhang; zhangxuehui914@163.com

Received 22 May 2015; Revised 20 August 2015; Accepted 20 August 2015

Academic Editor: Anh-Tuan Le

Copyright © 2015 Qianqian Wang et al. This is an open access article distributed under the Creative Commons Attribution License, which permits unrestricted use, distribution, and reproduction in any medium, provided the original work is properly cited.

The aim was to evaluate the remineralizing efficacy of fluorohydroxyapatite (FHA) gel on artificial dentinal caries lesion in vitro. Artificial carious lesions were made on occlusal cavities of teeth by exposing the dentin surface to a demineralizing solution. Each cavity was capped with a 3 mm thick FHA gel for 4 weeks. After the FHA gel was removed, the surface morphology and structure of the dentin were characterized by scanning electron microscopy (SEM), energy-dispersive X-ray spectroscopy (EDX), X-ray diffraction (XRD), and Fourier transform infrared spectroscopy (FT-IR). The dentin mineral density (DMD) was measured by micro-computed tomography (Micro-CT). A layer of dense and orderly hexagonal crystal structure, with average diameter of 1 μm and thickness of 4~5 μm , could be observed on dentin surface. These crystals exhibited elemental peaks for calcium, phosphorus, carbon, and oxygen and characteristic peaks of hydroxyapatite (HA) and fluorapatite (FA) via XRD and FT-IR. The DMD of dentin surface layer significantly increased after it was capped with FHA gel ($P < 0.05$). In the present study, the FHA gel could rapidly construct apatite on the artificial dentin caries surface and significantly increase the mineral density, which suggests that FHA gel might be a proper IPT material with remineralizing function.

1. Introduction

Minimally invasive dentistry (MID) is the application of “a systematic respect for the original tissue.” This implies that the dental profession recognizes that an artifact is of less biological value than the original healthy tissue [1]. In deep caries dentin discoloration occurs far in advance of the infection by microorganisms, and as much as 2 mm of the softened or discolored dentin is not infected but is reversibly denatured [2, 3]. Residual affected dentin has been suggested to be retained so as to keep its potential of being remineralized, which is otherwise removed in traditional carious excavation procedures. Indirect pulp-capping therapy (IPT) is considered as a minimally invasive treatment, in which caries are excavated and the tooth is restored with a suitable material [1, 3]. In doing so, the caries process

can be halted, and the residual affected dentin can be remineralized, which can be promoted by bioactive and ion-releasing base materials [4]. The key success factor is the application of remineralized materials during indirect pulp-capping therapy (IPT).

Over the years, calcium hydroxide ($\text{Ca}(\text{OH})_2$) has emerged as a gold standard for IPT. The benefits of $\text{Ca}(\text{OH})_2$ include its antimicrobial and anti-inflammatory effects, low thermal conductivity, and an ability to act as a buffer against the direct restorations [5–7]. However, it is still unknown whether this kind of material could remineralize dentin beneath $\text{Ca}(\text{OH})_2$. It merely provides hydroxide and calcium ions upon dissolution, but not the phosphate ion needed during remineralization.

Another IPT material, mineral trioxide aggregate (MTA), has been found to be important in dentistry due to its

biocompatibility and bioactive properties, which has been available since the early 1990s, displaying excellent potential in endodontic applications [8–11]. As the calcium silicate-containing material lacks phosphate, the MTA becomes bioactive and produces apatite only when it comes into contact with phosphate-containing fluids [12]. The procedure is effective *in vitro* in promoting optimal remineralization of the mineral-sparse surface of a carious lesion, but it is not possible to rely on dissolving biomimetic analogs in body fluids in a clinical setting [13]. As a result, these problems are leading scientists to explore new IPT materials which possess remineralizing efficacy in addition.

A new material system, fluorohydroxyapatite (FHA) gel system, has been developed for which prism-like structures on enamel were rapidly constructed on the natural human enamel surface using this gel system which contains $\text{Ca}(\text{NO}_3)_2$, KH_2PO_4 , KF, deionized water, and agarose [14]. This reaction occurs by spontaneous mineral nucleation on the surface of etched enamel under physiological conditions. The newly grown prism-like structure on enamel is identified as fluorapatite. It is hypothesized that the FHA gel may also form apatite structures on residual affected dentin in deep caries and may promote dentin remineralization. Within these parameters, the FHA gel could be applied as a suitable IPT material. The present study aims to evaluate the remineralizing efficacy of FHA gel system on artificial dentinal caries lesions when the gel is used as an IPT material, comparing it with calcium hydroxide and MTA.

2. Materials and Methods

2.1. Preparation of Artificial Caries. Sixty noncarious human third molars were obtained from the Peking University School of Stomatology under an agreement with the patients. The protocol for processing human tissue specimens was reviewed and approved by the University Committee on Use and Care of Human Tissue Specimens. The root was removed from the cement-enamel junction of the tooth, and only the crown was left. A cavity measuring 5 mm in length and width and 6 mm in thickness was made on the occlusal surface of the tooth, and the bottom of the cavity was positioned on the center of the dentin layer. Each side of the specimen was then painted with an acid-resistant nail varnish except for the dentin surface of cavity walls. Artificial carious lesions were induced by exposing the dentin surface to a demineralizing solution consisting of 0.1 M lactic acid which was adjusted to pH 5.0 for 72 hours [15]. Subsequently, the specimens were thoroughly rinsed with deionized water and 54 specimens were divided into three groups of 18 in each; the other 6 specimens were assigned to a control group.

2.2. IPT and Remineralization Experiments. The three test groups were as follows:

- Group FHA: FHA gel (PCT/CN2013/001026),
- Group CH: $\text{Ca}(\text{OH})_2$ (Calxyl, OCO-Präparat GMBH, Dirmstein, Germany),
- Group MTA: MTA (ProRoot MTA, Dentsply Tulsa, Dentsply International, Inc., USA).

FHA gel, which contained 0.40 M $\text{Ca}(\text{NO}_3)_2$, 0.24 M KH_2PO_4 , 0.08 M KF, deionized water, and agarose, was provided by the Department of Biomedical Engineering, College of Engineering, Peking University [14]. Briefly, agarose was added to the $\text{Ca}(\text{NO}_3)_2$ solution and heated with a microwave oven for 5–10 seconds. By adding KH_2PO_4 and KF to the heated solution, the mixed solution would cure and form agarose gel in 30 minutes under physiological conditions.

$\text{Ca}(\text{OH})_2$ and MTA materials were mixed as per the manufacturers' instructions.

Each cavity was capped with 3 mm thick materials, respectively, and subsequently restored with composite resin. They were placed in a 5 mL physiological saline solution at 37°C for 4 weeks. After 1 or 4 weeks, specimens were removed from the solution and prepared for examination. After the restoration and the materials were carefully separated from the cavity using explorer, specimens were washed with deionized water in ultrasonic cleaner for 15 min at 25 KHz (Transonic TP690, Elma, Germany).

2.3. Scanning Electron Microscopy and Elemental Analysis. The surface morphology and structure of the artificial dentin caries were characterized via a scanning electron microscopy (SEM, ZEISS, Supra 55, Germany). The elemental composition of the mineral crystal constructed on a remineralized layer was characterized by energy-dispersive X-ray spectroscopy (EDX, ZEISS, Supra 55, Germany).

2.4. X-Ray Diffraction and Fourier Transform Infrared Spectroscopy. The phase composition and structure of the mineral crystal were evaluated by X-ray diffraction spectroscopy (XRD, Rigaku D/max 2500 VB2+/PC, Japan) at 40 mA and 45 kV as well as by Fourier transform infrared spectroscopy (FT-IR, Nicolet 8700, USA). For Group FHA, XRD samples were the crystal powder scraped from the artificial caries layer. For Groups CH and MTA, XRD samples were the cured materials removed from the artificial caries cavity.

2.5. Micro-CT Scanning. The mineral density and lesion depth of artificial dentin caries were measured by the Inveon micro-computed tomography system (SIEMENS Medical Solutions, USA).

Scanning was performed with a spatial resolution of 9.21 μm at 80 kV and 500 μA and 360° rotation. The slab was rescanned during subsequent weeks with the same acquisition and reconstruction parameters. Following the scanning and image reconstruction, a three-dimensional (3D) image was obtained using COBRA Exxim software and analyzed via Data Analysis System (Inveon Research workplace 4.1). Mineral profiles were determined at precisely the same area (5 × 5 × 0.05 mm) within the 3D image during the experiment and the mineral density was acquired. Parameters of dentin mineral density (DMD) of the lesions and lesion depth were obtained in this study.

Specimens' assignments were analyzed with one-way ANOVA to ensure that there were no differences in the baseline mineral density and lesion depth among the groups. There were 18 specimens in each experimental group, 6 of

which were examined by SEM-EDX and XRD-FTIR at 1 week and another 6 at 4 weeks. The other 6 were examined with micro-CT scanning at 1-week and 4-week interval.

2.6. Statistical Analyses. The data were analyzed by SPSS software 19.0 (SPSS Science, SPSS Inc., Chicago, IL, USA). Statistical differences of mineral density and lesion depth between groups were evaluated by one-way ANOVA at $\alpha = 0.05$.

3. Results

3.1. SEM Images and EDX Analysis. The SEM images and EDX analysis at 1 week are shown in Figures 1 and 2.

The dentinal tubules remained open with a diameter of 3~5 μm in the artificial dentin caries (Figure 1(a)). Dense and orderly hexagonal crystal structure could be observed on the dentin surface of Group FHA and they covered the dentinal tubules and dentin surface (Figure 1(b)). Average diameter of the hexagonal crystal was about 1 μm (Figure 2(a)) and the thickness was about 4~5 μm (Figure 2(b)), which exhibited elemental peaks for calcium, phosphorus, carbon, and oxygen.

In Group CH, the dentinal tubules were partially occluded with crystal, which exhibited elemental peaks for calcium, carbon, oxygen, and barium. In Group MTA, the dentinal tubules were also occluded with cement phase, which exhibited elemental peaks for calcium, magnesium, silicon, carbon, and oxygen.

The SEM images at 4 weeks were similar to those at 1 week (data not shown).

3.2. XRD and FT-IR Spectroscopy. The XRD diffractogram and FT-IR spectra for all test materials are shown in Figure 3. The hexagonal crystal constructed by FHA gel also exhibited characteristic peaks of hydroxyapatite (HA) and fluorapatite (FA) (Figure 3(a1)), of which the spectrograph was nearly the same as that of natural dentin [16].

The crystal of Group CH exhibited characteristic peaks of calcium hydroxide ($\text{Ca}(\text{OH})_2$) and barium sulfate (BaSO_4) (Figure 3(b1)), while that of Group MTA exhibited characteristic peaks of bismuth oxide (Bi_2O_3), tricalcium silicate ($3\text{CaO}\cdot\text{SiO}_2$), dicalcium silicate ($2\text{CaO}\cdot\text{SiO}_2$), calcium carbonate (CaCO_3), and calcium dialuminate ($3\text{CaO}\cdot\text{Al}_2\text{O}_3$) (Figure 3(c1)) [17].

FT-IR spectra showed the bands or functional groups of the powders. The spectra of the hexagonal crystal were similar to those of natural dentin (Figure 3(a2)). A broad peak indicated 3800–2600 cm^{-1} and a small peak between 3536 cm^{-1} and 3545 cm^{-1} was related to the OH^- . A sharp and broad peak between 1100 cm^{-1} and 900 cm^{-1} was related to the PO_4^{3-} group. Stretching and bending modes for PO_4^{3-} were shown at 600 cm^{-1} and 572–560 cm^{-1} . Bands of 1500–1400 cm^{-1} were related to the CO_3^{2-} group [16].

As for $\text{Ca}(\text{OH})_2$, a broad peak indicated 3800–2600 cm^{-1} and a sharp peak between 3700 cm^{-1} and 3600 cm^{-1} was related to the OH^- . Bands of 1500–1400 cm^{-1} were related to the C–O group. A sharp and broad peak between 1210 cm^{-1}

and 1040 cm^{-1} and at 610 cm^{-1} was related to the SO_4^{2-} group (Figure 3(b2)) [18].

As the spectra of MTA showed, the splitting of the band in the 1000–850 cm^{-1} region resulted from the presence of silicate phases. The bands in the 1600–1300 cm^{-1} corresponded to the asymmetric stretching of the CO_3^{2-} group. A broad peak indicated 3800–2600 cm^{-1} and a small peak between 3536 cm^{-1} and 3545 cm^{-1} was related to the OH^- (Figure 3(c2)) [19].

3.3. Micro-CT Scanning. Development of DMD at each lesion level was presented in Figure 4. There were no significant differences in the baseline (0 W) DMD and lesion depth between groups ($P > 0.05$). Figure 4 presented an artificial caries lesion with a depth of approximately 300~400 μm and a surface DMD of 1.73 g/cm^3 .

After the IPT for 1 W, the DMD of dentin surface layer in the group FHA significantly increased to $2.018 \pm 0.041 \text{ g}/\text{cm}^3$ because of the hexagonal crystal ($P < 0.05$, Figures 5(b1) and 5(b2)), and the density was $1.756 \pm 0.044 \text{ g}/\text{cm}^3$ in the control group, $1.775 \pm 0.038 \text{ g}/\text{cm}^3$ in Group CH, and $1.796 \pm 0.008 \text{ g}/\text{cm}^3$ in Group MTA. However, there were no significant changes in the mineral density of the subsurface part of the lesion, nor in the lesion depth (Figure 4(a)).

After the IPT for 4 W, the DMD of dentin surface layer in Group FHA significantly increased to $2.077 \pm 0.012 \text{ g}/\text{cm}^3$ compared to the baseline at 0 W ($P < 0.05$, Figures 5(c1) and 5(c2)), but there was no significant difference with the DMD at 1 W ($P > 0.05$). The DMD of dentin surface layer was $1.764 \pm 0.045 \text{ g}/\text{cm}^3$ in the control group, $1.775 \pm 0.009 \text{ g}/\text{cm}^3$ in Group CH, and $1.805 \pm 0.135 \text{ g}/\text{cm}^3$ in Group MTA. There were still no significant changes in the mineral density of the subsurface part of the lesion, nor in the lesion depth (Figure 4(b)).

Micro-CT images showed that the hexagonal crystal covered nearly all the surface of dentinal caries lesions after being capped with FHA gel for 1 week and 4 weeks (Figures 5(b1) and 5(c1)). The crystal constructed on the surface and the mineral density of the surface layer increased, while the mineral density of the subsurface part of the lesion as well as lesion depth presented similar results as those before the IPT (Figures 5(b2) and 5(c2)).

4. Discussion

The present study was designed to assess the remineralizing efficacy of FHA gel system on artificial dentin caries lesions. Dental apatite is multiphase and can be described as carbonate-substituted or fluor-substituted hydroxyapatite [20]. This gel system contained Ca^{2+} , PO_4^{3-} , OH^- , and all ionic components that were necessary during HA crystal construction. Commercial product $\text{Ca}(\text{OH})_2$ in the present study was comprised of $\text{Ca}(\text{OH})_2$ and BaSO_4 which is used as a developer, and the main components of MTA were calcium silicate. FHA gel system embodied a distinct advantage when compared with $\text{Ca}(\text{OH})_2$ and MTA, which could not provide the phosphate ion needed during remineralization.

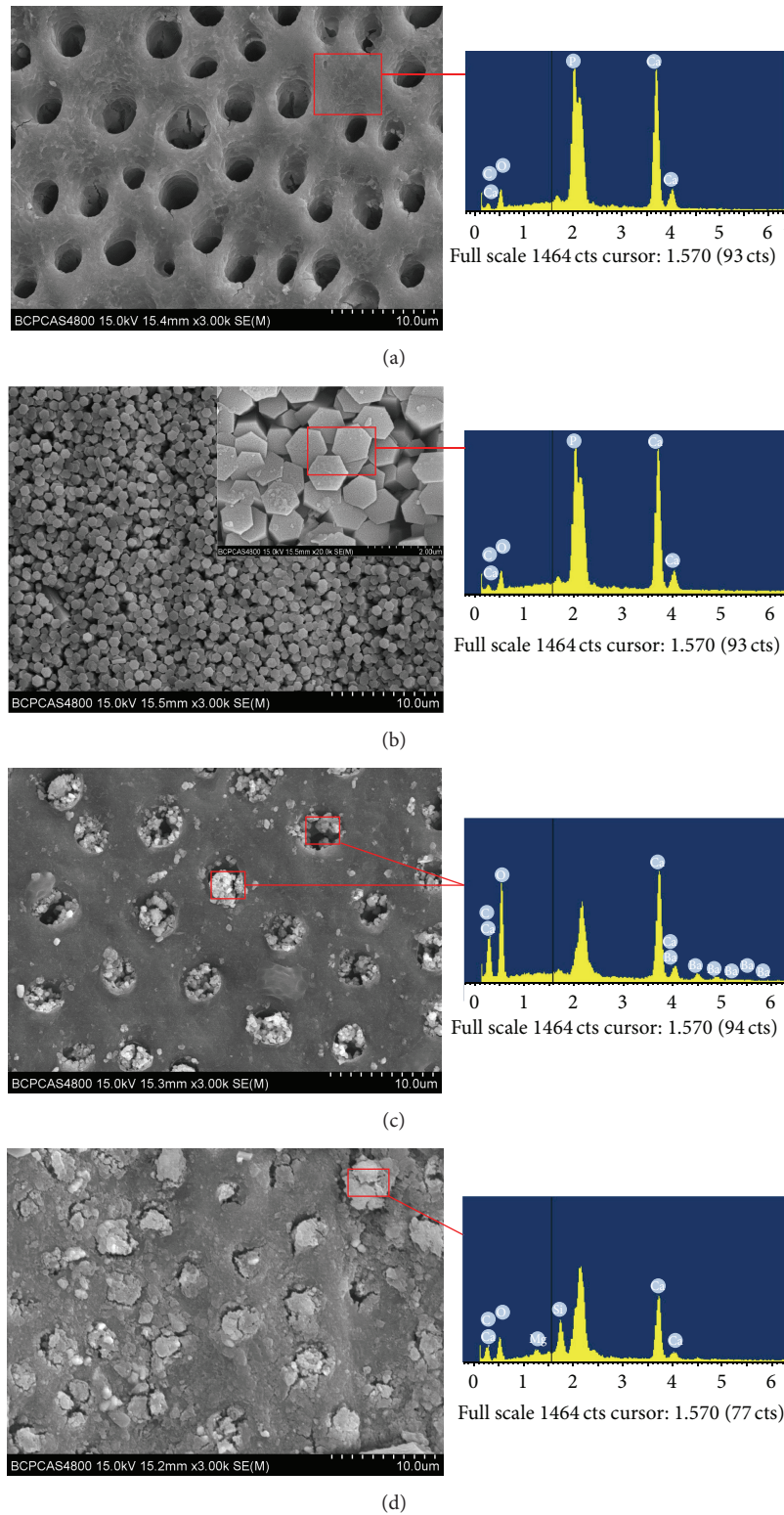


FIGURE 1: SEM images and EDX analysis of artificial caries layer surface. (a) Artificial dentin caries, (b) Group FHA, hexagonal crystal structure on artificial caries layer, exhibited elemental peaks for Ca, P, C, and O, (c) Group CH, artificial caries layer with crystal in dentin tube, exhibited elemental peaks for Ca, C, O, and Ba, and (d) Group MTA, artificial caries layer with crystal in dentin tube, exhibited elemental peaks for Ca, Si, Mg, C, and O.

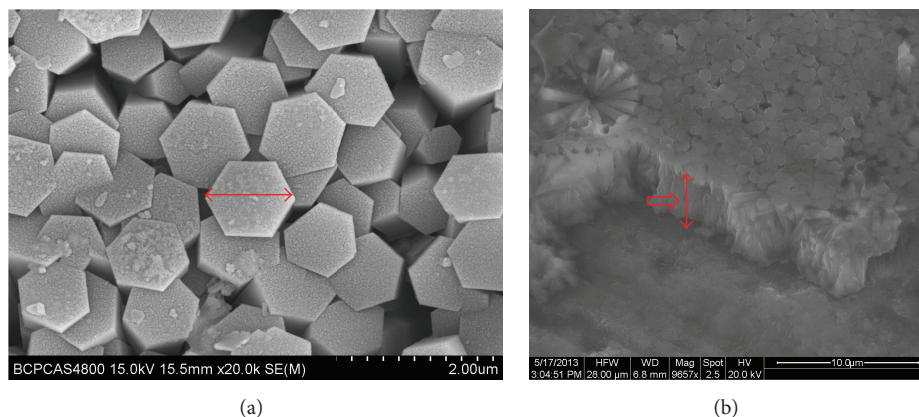


FIGURE 2: SEM image for the hexagonal crystal on the artificial caries surface of Group FHA. (a) The diameter of the hexagonal crystal was about $1\ \mu\text{m}$. (b) The thickness of the hexagonal crystal was about $4\sim 5\ \mu\text{m}$.

Another innovation was the application of agarose in this system. Recently, biomimetic mineralization approaches with an organic matrix to control apatite growth and orientation have been shown to induce enamel or dentin regeneration [21, 22]. Ning et al. obtained disordered deposited hydroxyapatite on dentin surface using agarose gel loaded with calcium phosphate. They also suggested that agarose hydrogel may provide the hydrogel microenvironment to mimic dentin formation and agarose may be considered as a template to control mineralization. We also used agarose in FHA gel system in the present study and obtained preferred orientation hydroxyapatite/fluorapatite crystals on dentin surface, and agarose may play the same role of hydrogel microenvironment and template based on the same mechanism as in previous report. The anionic groups of agarose in its monomeric units may bond to collagen molecules that carry a positive charge and induce HA crystals to nucleate and grow [22].

A unidirectional ion supply is thought to play a critical role in apatite growth and orientation [23]. In FHA gel system, calcium ions and phosphate ions may undergo oriented diffusion in the agarose hydrogel toward the dentin surface, which supplies ionic fluid from one direction as the source of mineralization [24].

A hypothetical model for the process may be summarized as follows. The formation of FA crystals is determined by two processes: the initiation of nucleation and the continued growth of nucleate [14]. It was believed that, in the initial stage, crystal nuclei form spontaneously in supersaturated solutions, and ions attach around the crystal nuclei. Agarose molecules in FHA gel system bond to the collagen molecules with positive charge on the dentin surface and formed the nucleation site. Calcium ions and phosphate ions in FHA gel diffuse to the site where mineralization occurs. Atomic or molecular building blocks will find the energetically favorable sites and integrate into the surface of the immature crystal. Nucleation clusters are generated in random orientation and then spontaneously aggregate into primary nanoparticles to minimize the total surface energy. Because van der Waals attraction along the long axis of the rods is stronger than that at the rod ends, rod-like crystals form a bundle when

continuing their growth. When the surface is covered with crystals, larger crystals would huddle together and maintain a uniform direction. In addition, the gel system provides a hydrogel microenvironment and the agarose may act as a template to induce nucleation and growth [22].

The layer of hexagonal crystal cannot be removed using an ultrasonic cleaner, which suggests that there may be some physical and chemical structures at the junction of crystal and dentin substrate surface. The results showed that the layer covered nearly all dentinal tubules and dentin surface, which may decrease permeation of demineralized dentin and protect the function of the pulp-dentinal complex.

In addition, this system also contained fluoride, which, in a remineralizing system, can be preferentially incorporated in the new mineral “vener.” The absorbed fluoride on partially demineralized crystal surfaces enhances mineral reprecipitation, leading to the formation of a new surface on the existing crystal remnants with lower solubility [25, 26].

The mineral density and lesion depth of artificial dentin caries were measured by the micro-CT system, which is a nondestructive technique [27]. After being capped with FHA gel for 1 W and 4 W, the DMD of dentin surface layer in Group FHA significantly increased, which was probably due to the dense layer of hexagonal crystal in Group FHA.

There were no significant changes in the mineral density of the subsurface part of the lesion, nor in the lesion depth in all three groups. The explanation may be that the apatite was too large to enter the space between collagen fibers. This is also the limitation and problem identified with other remineralizing systems [28]. Li and Chang found that when calcium phosphate nuclei grew to microspheres with a diameter of about $1\ \mu\text{m}$ and interconnected by collagen nanofibers, the apatite could just locate on the collagen fibers of surface layer [28]. Furthermore, the mineral content of surface layer affects the characteristics of subsequent remineralization [29]. Although fluorapatite enhances mineral uptake, it causes hypermineralization of the lesion surface and prevents effective remineralization of deeper parts of the caries lesion [29, 30].

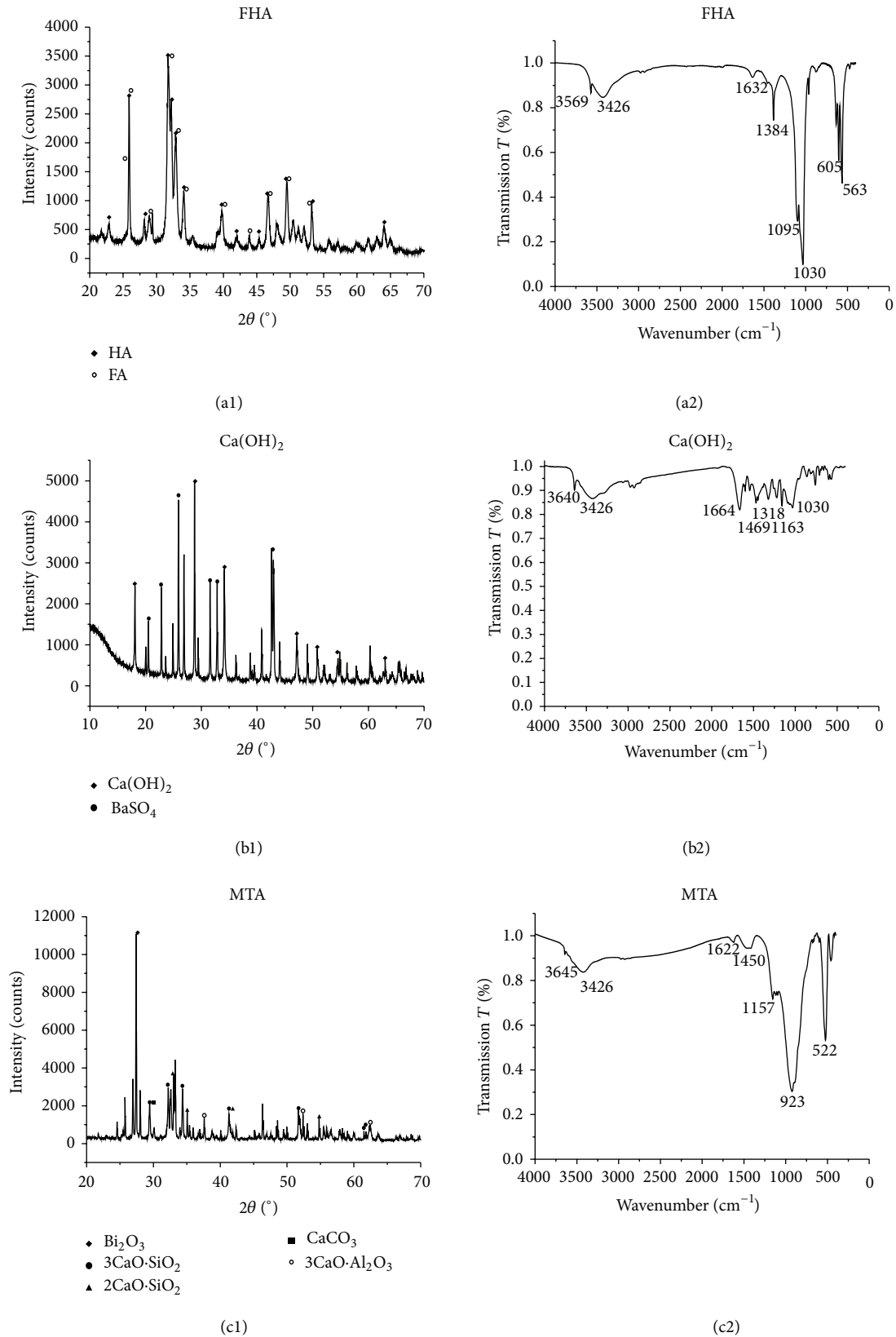


FIGURE 3: XRD spectrograph (a1, b1, and c1) and FT-IR (a2, b2, and c2) spectra of the hexagonal crystal of Group FHA, Ca(OH)₂, and MTA. (a1 and a2) Group FHA; (b1 and b2) Group CH; (c1 and c2) Group MTA.

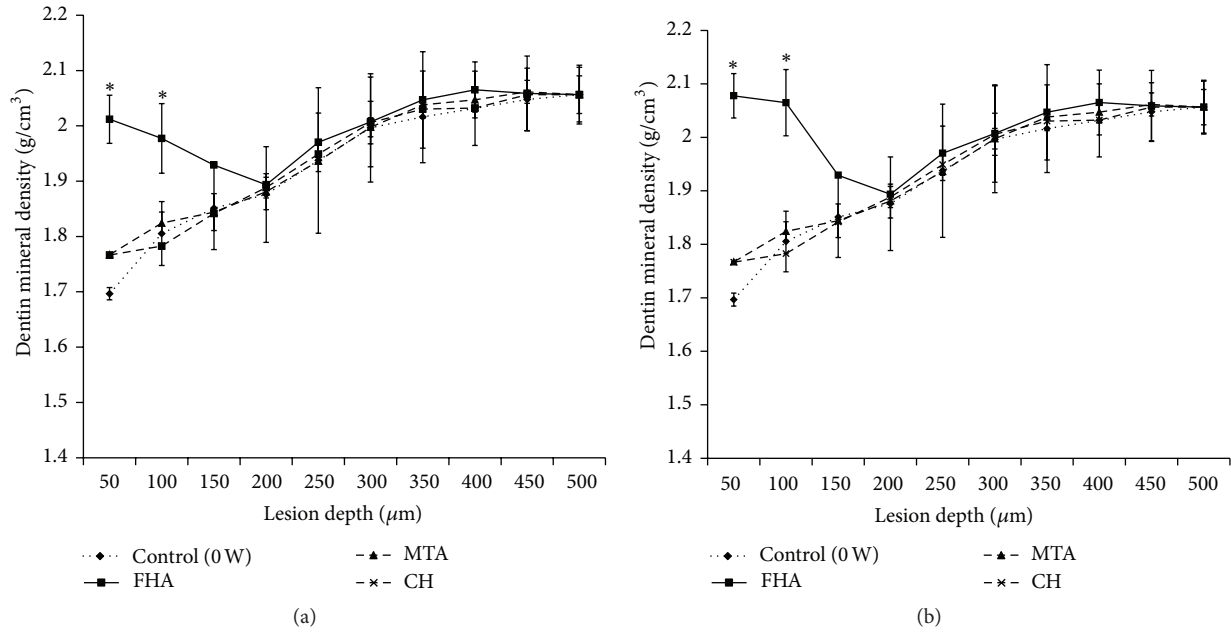


FIGURE 4: Dentin mineral density (DMD) and lesion depth of dentin disks after being treated for 1 week (a) and 4 weeks (b). Values represent the mean ± SD ($n = 6$, * $P < 0.05$).

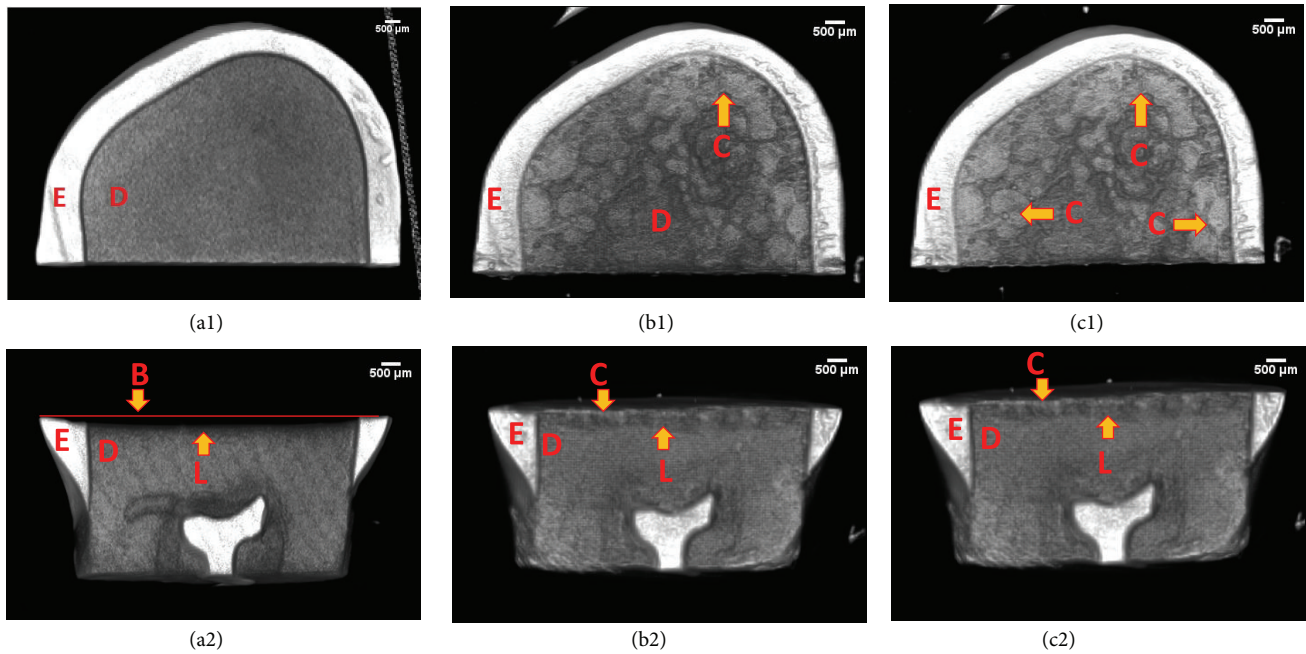


FIGURE 5: Micro-CT images of artificial dentinal caries lesion before (a1 and a2) and after being capped with FHA gel for 1 week (b1 and b2) and 4 weeks (c1 and c2). Hexagonal crystal covered nearly all the surface of the dentin (b1 and c1), and the mineral density of surface layer significantly increased (b2 and c2). E, enamel; D, dentin; C, crystal; L, lesion.

Amorphous calcium phosphate (ACP) is known as an important intermediate phase in the formation of calcium phosphate [24, 31]. Recently, a strategy called “Guided Tissue Remineralization” represents an approach to this problem by

attempting to backfill the demineralized dentin collagen with liquid-like ACP nanoprecursor particles that are stabilized by biomimetic analogs of noncollagenous proteins [12]. This strategy manages to achieve the goal of biomineralization

of caries-like dentin [32, 33]. Taken into account, the incorporation of biomimetic analogs of matrix proteins may be an effective solution in future studies.

5. Conclusion

In the present study, the administration of FHA gel resulted in a well-compacted fluorapatite layer deposited onto the dentin surface and significant increase of the mineral density. These findings suggest that FHA gel might be a proper IPT material with remineralizing function.

Conflict of Interests

The authors declare that there is no conflict of interests regarding the publication of this paper.

Acknowledgments

This project is supported by the National Basic Research Program of China (2012CB933900), the Key International S&T Cooperation Projects (2011DFA32190), the Key Technologies R&D Program of China (2012BAI07B01), and the Science Foundation of Peking University School and Hospital of Stomatology (PKUSS20130103).

References

- [1] D. Ericson, E. Kidd, D. McComb, I. Mjör, and M. J. Noack, "Minimally Invasive Dentistry—concepts and techniques in cariology," *Oral Health & Preventive Dentistry*, vol. 1, no. 1, pp. 59–72, 2003.
- [2] H. Miyauchi, M. Iwaku, and T. Fusayama, "Physiological recalcification of carious dentin," *Bulletin of the Tokyo Medical and Dental University*, vol. 25, no. 3, pp. 169–179, 1978.
- [3] D. Ericson, "What is minimally invasive dentistry?" *Oral Health & Preventive Dentistry*, vol. 2, supplement 1, pp. 287–292, 2004.
- [4] E. Bresciani, W. C. Wagner, M. F. L. Navarro, S. H. Dickens, and M. C. Peters, "In vivo dentin microhardness beneath a calcium-phosphate cement," *Journal of Dental Research*, vol. 89, no. 8, pp. 836–841, 2010.
- [5] C. Estrela and R. Holland, "Calcium hydroxide: study based on scientific evidences," *Journal of Applied Oral Science*, vol. 11, no. 4, pp. 269–282, 2003.
- [6] Q. Shen, J. Sun, J. Wu, C. Liu, and F. Chen, "An in vitro investigation of the mechanical-chemical and biological properties of calcium phosphate/calcium silicate/bismutite cement for dental pulp capping," *Journal of Biomedical Materials Research Part B: Applied Biomaterials*, vol. 94, no. 1, pp. 141–148, 2010.
- [7] C. F. Cox and S. Suzuki, "Re-evaluating pulp protection: calcium hydroxide liners vs. cohesive hybridization," *The Journal of the American Dental Association*, vol. 125, no. 7, pp. 823–831, 1994.
- [8] M. Aeinehchi, B. Eslami, M. Ghanbariha, and A. S. Saffar, "Mineral trioxide aggregate (MTA) and calcium hydroxide as pulp-capping agents in human teeth: a preliminary report," *International Endodontic Journal*, vol. 36, no. 3, pp. 225–231, 2003.
- [9] M. Torabinejad and M. Parirokh, "Mineral trioxide aggregate: a comprehensive literature review—part II: leakage and biocompatibility investigations," *Journal of Endodontics*, vol. 36, no. 2, pp. 190–202, 2010.
- [10] M. Parirokh and M. Torabinejad, "Mineral trioxide aggregate: a comprehensive literature review—Part I: chemical, physical, and antibacterial properties," *Journal of Endodontics*, vol. 36, no. 1, pp. 16–27, 2010.
- [11] M. Parirokh and M. Torabinejad, "Mineral trioxide aggregate: a comprehensive literature review—part III: clinical applications, drawbacks, and mechanism of action," *Journal of Endodontics*, vol. 36, no. 3, pp. 400–413, 2010.
- [12] F. R. Tay, D. H. Pashley, F. A. Rueggeberg, R. J. Loushine, and R. N. Weller, "Calcium phosphate phase transformation produced by the interaction of the portland cement component of white mineral trioxide aggregate with a phosphate-containing fluid," *Journal of Endodontics*, vol. 33, no. 11, pp. 1347–1351, 2007.
- [13] Y.-P. Qi, N. Li, L.-N. Niu et al., "Remineralization of artificial dental caries lesions by biomimetically modified mineral trioxide aggregate," *Acta Biomaterialia*, vol. 8, no. 2, pp. 836–842, 2012.
- [14] S. Liu, Y. Yin, and H. Chen, "PEO-assisted precipitation of human enamel-like fluorapatite films for tooth whitening," *CrystEngComm*, vol. 15, no. 29, pp. 5853–5859, 2013.
- [15] J. M. McIntyre, J. D. B. Featherstone, and J. Fu, "Studies of dental root surface caries. 1: comparison of natural and artificial root caries lesions," *Australian Dental Journal*, vol. 45, no. 1, pp. 24–30, 2000.
- [16] N. Montazeri, R. Jahandideh, and E. Biazar, "Synthesis of fluorapatite-hydroxyapatite nanoparticles and toxicity investigations," *International Journal of Nanomedicine*, vol. 6, pp. 197–201, 2011.
- [17] I. A. Belío-Reyes, L. Bucio, and E. Cruz-Chavez, "Phase composition of ProRoot mineral trioxide aggregate by X-ray powder diffraction," *Journal of Endodontics*, vol. 35, no. 6, pp. 875–878, 2009.
- [18] M. Saitoh, S. Masutani, T. Kojima, M. Saigoh, H. Hirose, and M. Nishiyama, "Thermal properties of dental materials—cavity liner and pulp capping agent," *Dental Materials Journal*, vol. 23, no. 3, pp. 399–405, 2004.
- [19] L. Grech, B. Mallia, and J. Camilleri, "Characterization of set intermediate restorative material, biodentine, bioaggregate and a prototype calcium silicate cement for use as root-end filling materials," *International Endodontic Journal*, vol. 46, no. 7, pp. 632–641, 2013.
- [20] W. Zhao, S. Wang, H. Hong, Z. Chen, M. Fan, and S. Yu, "The crystallographic properties of the mineral phases of enamel and dentin in normal deciduous and permanent teeth," *Zhonghua Kou Qiang Yi Xue Za Zhi*, vol. 37, no. 3, pp. 219–221, 2002.
- [21] M. Iijima and J. Moradian-Oldak, "Control of apatite crystal growth in a fluoride containing amelogenin-rich matrix," *Biomaterials*, vol. 26, no. 13, pp. 1595–1603, 2005.
- [22] T.-Y. Ning, X.-H. Xu, L.-F. Zhu et al., "Biomimetic mineralization of dentin induced by agarose gel loaded with calcium phosphate," *Journal of Biomedical Materials Research Part B: Applied Biomaterials*, vol. 100, no. 1, pp. 138–144, 2012.
- [23] M. Iijima, K. Hayashi, and Y. Moriwaki, "Effects of the Ca^{2+} and PO_4^{3-} ion flow on the lengthwise growth of octacalcium phosphate in a model system of enamel crystal formation with controlled ionic diffusion," *Journal of Crystal Growth*, vol. 234, no. 2-3, pp. 539–544, 2002.

- [24] L. B. Gower, "Biomimetic model systems for investigating the amorphous precursor pathway and its role in biomineralization," *Chemical Reviews*, vol. 108, no. 11, pp. 4551–4627, 2008.
- [25] J. D. B. Featherstone, "Dental caries: a dynamic disease process," *Australian Dental Journal*, vol. 53, no. 3, pp. 286–291, 2008.
- [26] I. Diamanti, H. Koletsi-Kounari, E. Mamai-Homata, and G. Vougiouklakis, "Effect of fluoride and of calcium sodium phosphosilicate toothpastes on pre-softened dentin demineralization and remineralization in vitro," *Journal of Dentistry*, vol. 38, no. 8, pp. 671–677, 2010.
- [27] S. K. Manesh, C. L. Darling, and D. Fried, "Assessment of dentin remineralization with PS-OCT," in *Lasers in Dentistry XV*, vol. 7162 of *Proceedings of SPIE*, Society of Photo-Optical Instrumentation Engineers, February 2009.
- [28] X. Li and J. Chang, "Preparation of bone-like apatite-collagen nanocomposites by a biomimetic process with phosphorylated collagen," *Journal of Biomedical Materials Research—Part A*, vol. 85, no. 2, pp. 293–300, 2008.
- [29] K. Kawasaki, J. Ruben, H. Tsuda, M. C. D. N. J. M. Huysmans, and O. Takagi, "Relationship between mineral distributions in dentine lesions and subsequent remineralization in vitro," *Caries Research*, vol. 34, no. 5, pp. 395–403, 2000.
- [30] K. P. Preston, P. W. Smith, and S. M. Higham, "The influence of varying fluoride concentrations on in vitro remineralisation of artificial dentinal lesions with differing lesion morphologies," *Archives of Oral Biology*, vol. 53, no. 1, pp. 20–26, 2008.
- [31] H. Cölfen, "Single crystals with complex form via amorphous precursors," *Angewandte Chemie International Edition*, vol. 47, no. 13, pp. 2351–2353, 2008.
- [32] Y. Liu, S. Mai, N. Li et al., "Differences between top-down and bottom-up approaches in mineralizing thick, partially demineralized collagen scaffolds," *Acta Biomaterialia*, vol. 7, no. 4, pp. 1742–1751, 2011.
- [33] A. K. Burwell, T. Thula-Mata, L. B. Gower et al., "Functional remineralization of dentin lesions using polymer-induced liquid-precursor process," *PLoS ONE*, vol. 7, Article ID e38852, 2012.

Research Article

The Application of Carbon Nanotubes in Magnetic Fluid Hyperthermia

Grzegorz Raniszewski,¹ Arkadiusz Miaskowski,² and Sławomir Wiak¹

¹Lodz University of Technology, Stefanowskiego Street 18/22, 90-924 Lodz, Poland

²University of Life Sciences in Lublin, Akademicka Street 13, 20-033 Lublin, Poland

Correspondence should be addressed to Grzegorz Raniszewski; grzegorz.raniszewski@p.lodz.pl

Received 22 May 2015; Revised 12 July 2015; Accepted 14 July 2015

Academic Editor: Anh-Tuan Le

Copyright © 2015 Grzegorz Raniszewski et al. This is an open access article distributed under the Creative Commons Attribution License, which permits unrestricted use, distribution, and reproduction in any medium, provided the original work is properly cited.

The aim of this paper is to present the results of the investigation into the applications of carbon nanotubes with ferromagnetic nanoparticles as nanoheaters for targeted thermal ablation of cancer cells. Relevant nanoparticles' characteristics were exploited in terms of their functionality for biomedical applications and their magnetic properties were examined to determine heat generation efficiency induced by the exposure of the particles to an alternating magnetic field. The influence of the electromagnetic field on the human body tissues was assessed, providing quantitative measures of the interaction. The behavior of a liquid containing magnetic particles, during the exposure to the alternating magnetic field, was verified. As for the application for the ferromagnetic carbon nanotubes, the authors investigated temperature distribution in human liver tumor together with Arrhenius tissue damage model and the thermal dose concept.

1. Introduction

The magnetic fluid hyperthermia (MFH) is a new and promising therapeutic technique. It works by increasing the temperature in the area of tumor, which triggers the natural mechanisms of self-destruction of the cells called apoptosis. Classical methods of hyperthermia suffer serious problems related to focusing the temperature rise at tumor area, and thus they cause side effects for the patient. In case of the MFH, it is different because the heating energy is provided directly to the target region. This is done by means of magnetic nanoparticles that are placed in the patient's body. When the nanoparticles are exposed to an alternating magnetic field with properly chosen frequency, the superparamagnetic heat phenomenon is observed.

Authors have assumed that a magnetic fluid with known ferromagnetic carbon nanotubes concentration was delivered directly to a tumor. It can be done when the location and extent of the tumor are known and it is easily accessible for delivery, for example, through an injection. Moreover, it is

assumed that magnetic nanoparticles, together with tumor region, create homogeneous composite and their physical parameters are expressed in the form of effective ones. Moreover, we have not considered the power density due to the eddy currents as they are negligible regarding the heating of the injected magnetic fluid. On the other hand, the authors are conscious that eddy currents are important when talking about inductive heating. The maximum power density values in the body are determined by the size of the body, and so is the distance between the applicator and the skin. But this phenomenon will not be discussed in this study.

2. Synthesis of Ferromagnetic Carbon Nanotubes

There exists an extensive research on magnetic nanoparticles (MNPs) heated in a magnetic field as a tool for destroying cancer [1–6]. Among different kinds of MNPs, carbon nanotubes have gained interest of scientists due to very promising

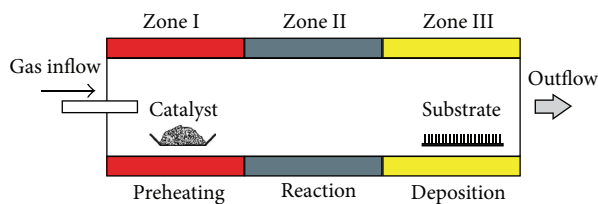


FIGURE 1: The experimental setup.

physical properties. The nanotubes have the advantage over other MNPs. Their quasi-one-dimensional shape renders them more efficient in terms of heat generation due to higher coercivity and saturation of magnetization of the CNTs as compared to spherical particles [7, 8].

The most common methods for carbon nanotubes (CNTs) synthesis are various types of chemical vapor deposition (CVD) and arc discharge methods. In CVD methods, gases containing carbon are usually used as a source of carbon for CNTs formation. In arc discharge methods, carbon comes from graphite anode. In the arc reactors, two types of carbon nanotubes can be collected: single-wall carbon nanotubes (SWNTs) and multiwall carbon nanotubes (MWNTs). MWNTs are usually located inside the cathode deposit. The syntheses of SWNTs need application of catalysts and they are deposited on the reactor walls, especially on the top of the reactor and in the anode area.

In CVD methods, the carbon for formation of carbon nanotubes is delivered in gaseous form. Two most common methods of carbon introduction into the system are application of hydrocarbons such as ethylene and acetylene. Gases with carbon gas decompose in high temperature and form carbon structures such as carbon nanotubes. Another group of CVD systems employ catalysts with carbons in solid or liquid state. Catalysts vaporize and are deposited as carbon nanotubes on substrates.

3. An Experiment

The method used for ferromagnetic carbon nanotubes synthesis was chemical vapor deposition with the tube furnace. As the carbon source ethylene was chosen, ferrocene was used as the catalyst. In the experimental setup, shown in Figure 1, four gases such as argon, helium, hydrogen, and ethylene were used and introduced into the furnace which was divided into three zones. In the first zone, inside the quartz tube, there was placed a catalyst in a ceramic boat. Relatively low temperature of this zone (500 K) allows for slowing evaporation of catalyst containing iron and carbon. The second zone was for regulation of the reaction time (500–1000 K). Too low temperature caused lack of catalyst decomposition. In the third zone, there was a silicon plate, substrate on which the CNTs should be deposited. The temperature of the third zone was about 1000 K. These parameters allowed for formation of carbon nanotubes with iron nanoparticles (Fe-CNTs). The scheme of Fe-CNT's formation is presented in Figure 2.

Carbon nanotubes collected from the substrate (and from the quartz tube walls) are contaminated with soot and

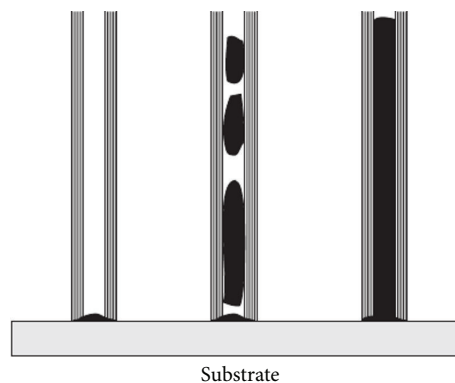


FIGURE 2: Carbon nanotubes filled with iron.

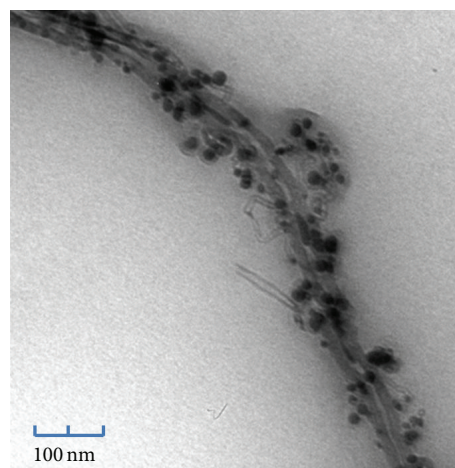


FIGURE 3: TEM of ferromagnetic nanotubes.

amorphous carbon. To purify the final product, an oxidation in high temperature (700 K) was used. Carbon impurities oxidize in low temperatures. Carbon nanotubes due to their thermal properties are resistant to temperatures up to 1000 K [11].

4. Results

Carbon nanotubes produced by this method were characterized by their ability to generate heat caused by the electromagnetic field with known parameters, that is, frequency and magnetic flux density. Moreover, to investigate if the thermal oxidation was an appropriate method of purification, thermogravimetric test was done. The iron contamination in the sample was estimated by EDS analysis. It was found that 5–15 wt% of iron was found in CNTs synthesized at temperatures 1000–1100 K. The iron spontaneously filled carbon nanotubes in different ratios. Some of the iron nanoparticles were attached to the surface outside the nanotubes (Figure 3).

Although fulfillment of the nanotubes has a much larger volume, the majority of molecules placed outside the nanotube have the size of nanometers. It was calculated that average diameter of iron nanoparticles was 10.3 nm. To estimate the diameter of nanotubes, dynamic light scattering (DLS)

has been used. Multiwalled carbon nanotubes synthesized by this method have length around 30–50 μm and diameter of 30–60 nm.

To determine the cytotoxicity ferromagnetic carbon nanotubes and their effects on cell, viability tests on the cell lines were conducted. A variety of carbon nanotubes concentration in the culture cell medium was prepared in the range of 5–500 mg/L. There was no significant influence of CNTs on cell viability. It indicates that they are inert to the cells. After functionalization (ligands conjugation to the carbon nanotubes structure) and attachment to the cells, they will have a selective destructive effect on cancer cells in the electromagnetic field.

The interaction of magnetic nanoparticles with the electromagnetic field depends on the particles' properties, their morphology, and suspending medium (if present), as well as the field parameters. Combining all the above factors, various magnetic loss mechanisms can be distinguished. Knowing the mechanism, the quantity of heat generated by a certain amount of particles can be calculated per one period of oscillating field. The quantity is generally referred to as Specific Magnetic Loss Energy (SMLE). In order to obtain the overall heating capacity of a given particle amount in a specific field, the Specific Loss Power (SLP) is calculated, by multiplying SMLE with the frequency f of the field applied. In different magnetic loss mechanisms, the SLP is estimated using various relations.

Ferromagnetic-doped CNTs in the form of powder produce heat when exposed to an alternating magnetic field. The atomic dipoles' alignment, as a response to the magnetic field, can be represented by a hysteretic dependence of magnetization (M) versus magnetic field strength (H). The heat generation is a result of hysteresis losses due to the reversing of magnetization [12–14].

Ferromagnetic nanoparticles generate heat in cases when an applied magnetic field is stronger than the coercivity that is applied. This is the reason why the low coercivity nanoparticles are preferred. Ferromagnetic carbon nanotubes are able to generate heat with the application of low magnetic fields [15]. In hyperthermia applications, the applied magnetic field ranges from 10 mT to about 25 mT at a frequency of kHz. The high frequency is required to avoid pain. The small field will only partially magnetize the nanoparticles. In kHz frequencies, AC loss effects are also significant. Figure 4 shows the hysteresis loops for the sample obtained from CVD system for temperature 300 K. They are compared to the hysteresis loops for the sample without iron (Figure 5). As a reference sample, Nanocyl NC 7000 has been used. As expected, the carbon nanotubes with ferromagnetic nanoparticles show a significant hysteresis compared to ferromagnetic properties of multiwall carbon nanotubes from the market.

The amount of heat generated by the magnetic nanoparticles is commonly expressed in terms of the SAR, which is understood as the power generated per unit mass of magnetic material in the solution. SAR is given by

$$\text{SAR} = c \cdot \frac{m_{\text{sample}}}{m_{\text{Fe}}} \frac{\Delta T}{\Delta t}, \quad (1)$$

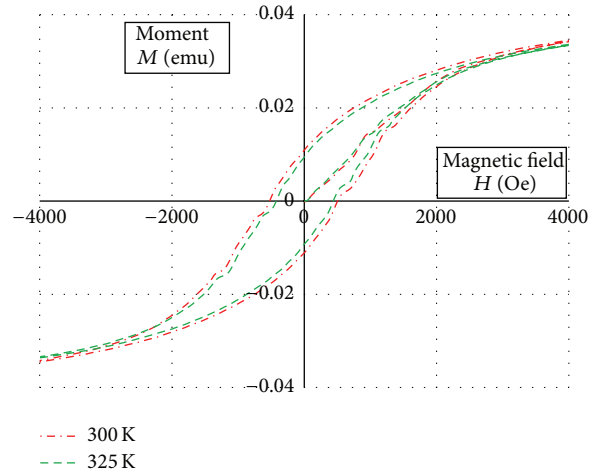


FIGURE 4: Hysteresis loop for carbon nanotubes with ferromagnetic nanoparticles.

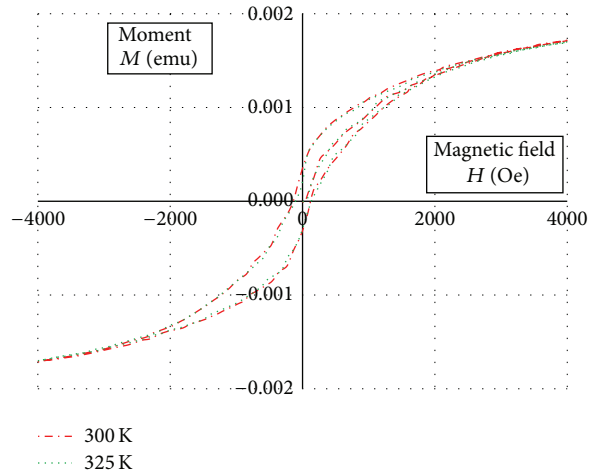


FIGURE 5: Hysteresis loop for carbon nanotubes without ferromagnetic nanoparticles.

where c is the heat capacity of the colloid, m_{sample} is the mass of the sample, m_{Fe} is the mass of iron oxide in the sample, and $\Delta T/\Delta t$ represents the heating rate. The volumetric energy dissipation rates Q_{ext} and SAR are related by

$$Q_{\text{ext}} = \text{SAR} \cdot w_{\text{Fe}} = \text{SAR} \cdot \varphi \cdot \rho_{\text{Fe}}, \quad (2)$$

where w_{Fe} is the mass of iron oxide per unit volume, φ is the volume fraction on iron oxide, and ρ_{Fe} is the density of iron oxide. It is very important to note that (2) is accurate if the heat capacity of the nanoparticles is in thermal equilibrium with its surroundings at the start of the experiments. Otherwise, heat flow to/from the environment can confound the measurements [16].

On the other hand, the SAR parameter for the same magnetic fluid will change when measured in AC magnetic field systems with different frequencies and strengths, as

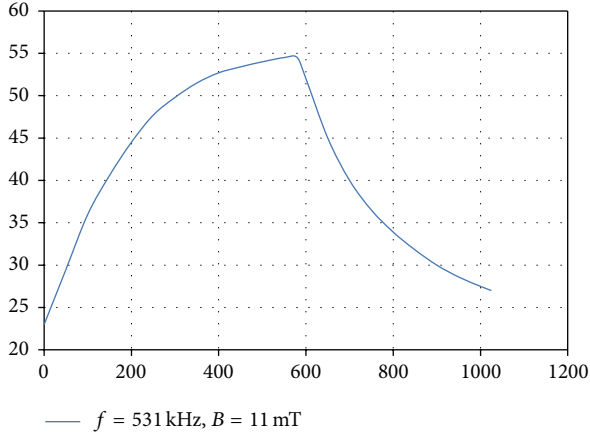


FIGURE 6: The heating profile of 2 mL DMSA stabilized magnetite carbon nanotubes dispersed in water, $B = 11$ mT, $f = 532$ kHz.

can be deduced from the formula for volumetric power dissipation [5]:

$$Q_{\text{ext}} = \mu_0 \pi \chi'' f H_0^2, \quad (3)$$

where μ_0 is the permeability of free space, χ is the out-of-phase (imaginary) component of susceptibility, and H is the applied magnetic field strength.

5. CNT's Dispersion in Aqueous Media

In our case, the magnetic fluid was prepared by ferromagnetic carbon nanotubes dispersion in aqueous media. Due to their insolubility in any sort of solvents resulting from strong Van der Waals forces, extremely high aspect ratio, and flexibility of the particles, the particles tend to form bundles or agglomerates [17–19]. The dispersion is achieved by ultrasonication.

The examined Fe concentrations were from 5 to 75 mg/mL, whereas the average magnetic particle diameter was 10.3 nm. Moreover, ferromagnetic nanotubes were DMSA stabilized and dispersed in distilled water. The heating properties of the ferrofluid were measured using Nanotherics Magnetherm system. The system consists of a function generator and a power amplifier and it is monitored by oscilloscope. During measurements, the sample was placed in a coil enclosure and the temperature was measured with a fiberoptic temperature sensor. The data collected by the sensor are shown in Figure 6 at frequency $f = 530$ kHz.

In order to validate the measured data, the numerical investigation was prepared and the results of both the numerical and the experimental investigations were compared. The numerical model of the Magnetherm system was prepared using Sencad X software (Figure 7). During the experiments, the 9-turn coil leading current $I_{\text{rms}} = 43$ [A] was used. The numerical axisymmetric model of the 40 mm diameter copper's coil can be seen in Figure 8.

To calculate a magnetic flux distribution in the coil, the low frequency solver was applied. In our case, we have used the low frequency magnetoquasistatic algorithm where the electric field \mathbf{E} is calculated in the lossy ($\sigma \neq 0$)

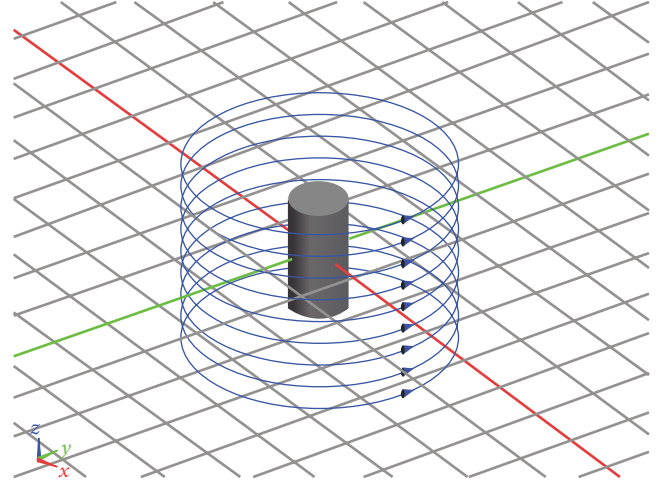


FIGURE 7: The numerical model of 9-turn coil used in the system with the ferrofluid sample.

domain, whereas the magnetic field \mathbf{H} is calculated overall. The magnetic flux distribution in the middle cross-section can be seen in Figure 9. It can be seen that the sample is exposed to a uniform magnetic field and it can be assumed that the sample is uniformly heated.

6. Temperature Distribution in Biological Cell Hyperthermia Cancer Treatment

6.1. *Thermal Problem.* For heat transfer in biological tissues in this study, Pennes' bioheat transfer equation was used [20]:

$$\rho c \frac{\partial T}{\partial t} = \nabla \cdot (\kappa \nabla T) - \rho_b c_b \omega (T - T_b) + Q_{\text{met}} + Q_{\text{ext}}, \quad (4)$$

where ρ is the tissue density, c is tissue specific heat, ρ_b is the density of blood, c_b is blood specific heat, κ is tissue thermal conductivity, ω is blood perfusion rate, T_b is arterial blood temperature, and Q_{met} is metabolic heat source. The cooling associated with the heat exchange with environment was imposed in the form of Robin's boundary condition; that is,

$$\kappa \frac{\partial T}{\partial n} = h (T_{\text{ext}} - T), \quad (5)$$

where h is the heat transfer coefficient and T_{ext} is the external temperature.

In the case of magnetic fluid hyperthermia, the Q_{ext} term is the power density (the energy deposition) due to heating of the magnetic fluid in an AC magnetic field. In this study, the authors have used the SAR value received from experiments to numerically investigate a temperature distribution in the anatomically correct human model. A special attention has been paid on the model of the tumor region with magnetic fluid, where the values for the electrical conductivity σ , the density ρ , the heat capacity c , and the thermal conductivity κ have been calculated as the effective one as follows:

$$\rho = (1 - \varphi) \rho_{\text{tumor}} + \varphi \rho_{\text{MF}}. \quad (6)$$

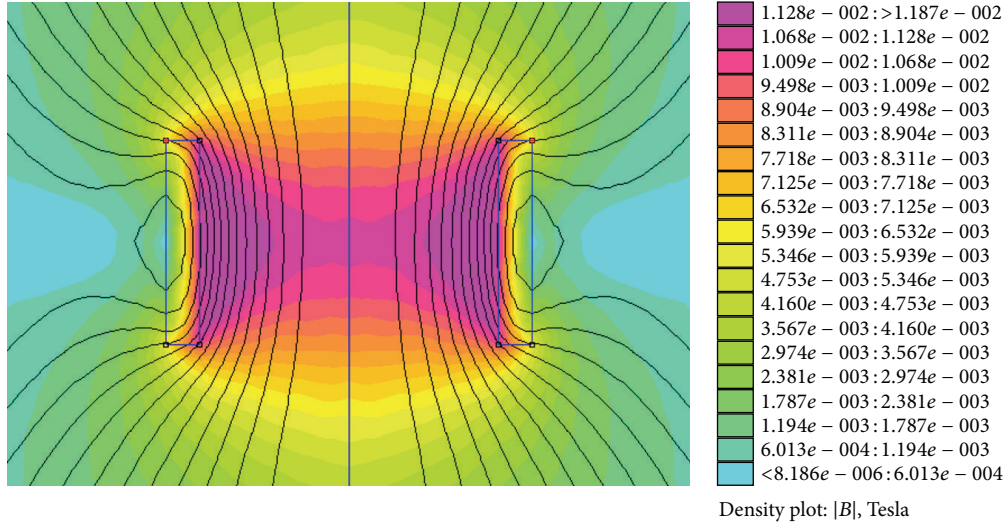


FIGURE 8: The magnetic flux distribution in the 9-turn coil used in the experiments.

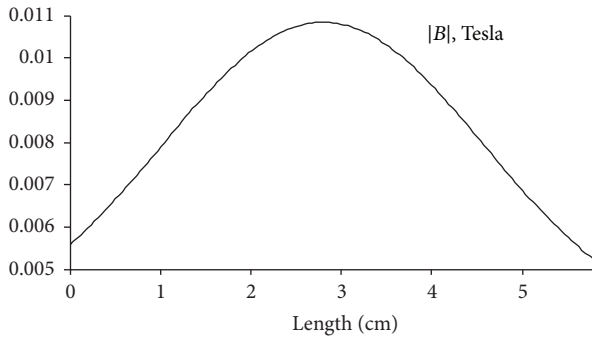


FIGURE 9: Magnetic flux distribution along z-axis

The effective specific heat is as follows:

$$c = (1 - \varphi) c_{\text{tumor}} + \varphi c_{\text{MF}}. \quad (7)$$

The effective thermal conductivity is as follows:

$$\frac{1}{\kappa} = \frac{1 - \varphi}{\kappa_{\text{tumor}}} + \frac{\varphi}{\kappa_{\text{MF}}} \quad (8)$$

and the effective electrical conductivity is as follows:

$$\frac{1}{\sigma} = \frac{1 - \varphi}{\sigma_{\text{tumor}}} + \frac{\varphi}{\sigma_{\text{MF}}}, \quad (9)$$

where subscript MF indicates magnetic fluid. That means that the tumor region was treated as a homogeneous composite. Moreover, a blood heat capacity $c_b = 4.05 \cdot 10^6$ and liver metabolic heat $Q_{\text{met}} = 11.37 \text{ W/m}^3$ were used in the Pennes model.

The temperature distribution in the human tissues is determined by a number of thermophysical factors, such as heat capacity and thermal conductivity, the spatial geometry (anatomy), and heat production due to metabolism. There are high-resolution numerical phantoms based MRI images

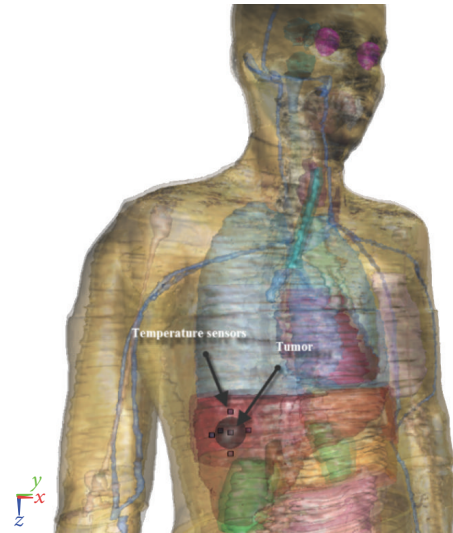


FIGURE 10: The model of Ella with liver tumor and points in which the temperature was measured.

which can be used to predict thermophysical effects. In this work, the authors have used an anatomically correct model from Virtual Population [21]. The model represents a 26-year-old female, with 1.63 m height and 58.7 kg weight (Figure 10). To numerically model a liver tumor, the sphere with radius $r = 15 \text{ mm}$ has been embedded in it. The properties of tissues were taken, obtained from the database of the IT'IS Foundation [22] and the calculations was fixed at a frequency of 530 kHz. The liver tumor electric and thermal properties were taken from the literature [9, 10] (see Table 1). In our case, the SAR = 41.8 W/kg.

6.2. Tissue Damage Model. Apart from the temperature distribution, the Arrhenius model was used to estimate tissue damage as another parameter. In this model, it is assumed

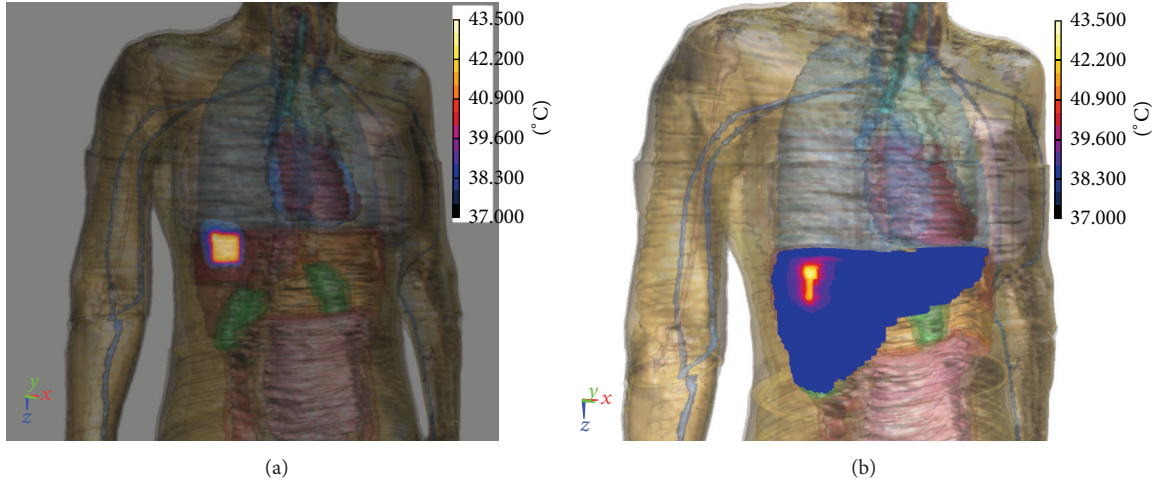


FIGURE 11: Temperature distribution in the liver tumor after 1800 sek. (cross-section (a), surface temperature distribution (b)).

TABLE 1: Electric and thermal properties of healthy liver and the one with tumor [9, 10].

Tissue	ρ (kg·m ⁻³)	C (J·kg ⁻¹ ·K ⁻¹)	κ (W·m ⁻¹ ·K ⁻¹)	σ (S·m ⁻¹)	ω_0 (kg·m ⁻³ ·s ⁻¹)
Healthy liver	1080	3455	0.173	0.51	17.03
Liver tumor	1045	3760	0.52	0.5	2.09

TABLE 2: Kinetic coefficients for the healthy liver and liver tumor [9, 10].

Tissue	A (s ⁻¹)	ΔE (J/mol)
Healthy liver	$7.390 \cdot 10^{39}$	$2.577 \cdot 10^5$
Liver tumor	$3.247 \cdot 10^{43}$	$2.814 \cdot 10^5$

that the biological damage depends on both temperature and time and can be quantified by the function of tissue injury Ω :

$$\Omega(t) = \int_0^t A e^{-\Delta E/RT} dt, \quad (10)$$

where T is the absolute temperature, which is a function of ablation time, R is the gas constant 8.314 J/(mol K)), A is the frequency factor (s⁻¹), and ΔE is the energy activation for the irreversible damage reaction. Kinetic coefficients A and ΔE are presented in Table 2. It should be underlined that $\Omega(t)$ is the damage integral, while $F = 1 - e^{-\Omega(t)}$ and corresponds to a 63% probability of the death of cells if $\Omega(t) = 1$. In other words, at $\Omega(t) < 1$, the tissue is considered as a live one.

6.3. Thermal Dose. Together with the temperature distribution and Arrhenius tissue damage model, the authors have analyzed the thermal factor, which is the thermal dose concept developed by Sapareto and Dewey in 1984 [23]. Cumulative equivalent minutes at 43°C (CEM₄₃) are defined as

$$\text{CEM}_{43} = \int_0^t R^{43-T(t)} dt \quad (11)$$

with $R = 0.5$ for $T > 43$, $R = 0.25$ for $43 \geq T \geq 39$, and $R = 0$ for $T < 39$.

When the CEM₄₃ value exceeds a critical threshold, the tissue is considered to be thermally necrosed. Thresholds for CEM₄₃ have been tabulated in the literature for several types of tissue based upon experimental observation of tissue injury at 43°C [24–28].

The critical thermal dose for liver tissue is CEM₄₃ = 340 minutes [29]. Once the temperature was determined at each time step, the CEM₄₃ was calculated. The tissue was considered to begin necrosis when this factor exceeded 40 minutes [30], although significant degree of damage appears when cumulative equivalent is not less than 240 minutes [31–33].

7. Results

Figure 11 shows the temperature distribution in the liver tumor after 1800 sek. The important observation in Figure 11 is the temporal evaluation of temperature at various points which is unsymmetrical. The effect of anatomy (the liver shape) can be seen in Figure 11 where it is shown that the maximum temperature is reached at the different locations, which may have an implication for expected treatment planning.

The cumulative equivalent minutes for this case are shown in Figure 12.

It can be observed that maximum temperature $T = 43.5^\circ\text{C}$ in the middle of the tumor was reached after about 300 sek. (Figure 13). In Figure 14, there are temperature profiles in the thermosensors symmetrically surrounding the tumor. In our numerical experiments, it was assumed that magnetic nanoparticles were dispersed homogeneously, but the temperatures on the tumor boundary did not have the same profiles. One should notice that the liver is surrounded

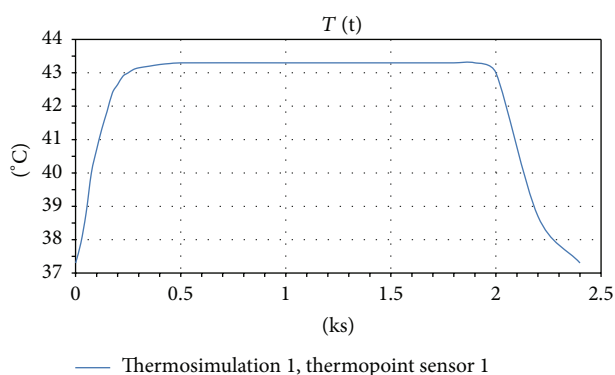
FIGURE 12: CEM_{43} .

FIGURE 13: Temperature versus time for different thermal sensors, sensor placed in the middle of the tumor.

by different tissues and due to different perfusion rates the tumor boundaries will be cooled with various rates.

8. Conclusions

There are many methods of carbon nanotubes synthesis. The main methods employ high temperature (e.g., arc discharge method) and low temperature (e.g., chemical vapor deposition). Although both methods need purification of the results of synthesis, CVD method is preferred in this study. In our research, we used a ferrocene as a catalyst and to fill carbon nanotubes by iron. These carbon nanotubes work then as ferrofluids but in contrast to ferrofluids CNTs may be easily biofunctionalized and then can be introduced into the human body. Cancer cells overexpress folic acid (FA) as well as epidermal growth factor (EGF) receptors. Carbon nanotubes with FA and EGF show preference for binding to a cancer cell which is an advantage in relation to ferromagnetic fluids. Application of carbon nanotubes with ferromagnetic properties can be used in a radiofrequency thermal ablation. RF ablation therapy brings the lowest risk compared to the other techniques (e.g., surgery, chemotherapy) of tumor therapy. This method offers faster and more targeted treatment for liver cancer with fewer side effects. The absorption coefficient of radio waves by the human body is relatively low. Metals in the carbon nanotube absorb this energy much

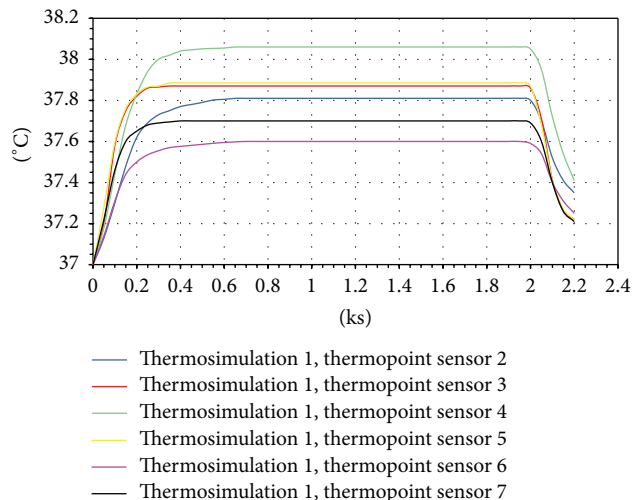


FIGURE 14: Temperature versus time for different thermal sensors, sensors placed on the tumor boundary.

more efficiently than a tissue. In this paper, prediction of spatial temperature distribution in the anatomically correct human model has been presented. Based on experimental and numerical investigation, the power dissipation from ferromagnetic carbon nanotubes has been investigated. The authors have shown that the carbon nanotubes have the potential for the hyperthermia treatment.

From the numerical investigation presented above, one can conclude that, in terms of maximum temperature rise, the expected treatment outcome depends on the tissue distribution around the tumor.

Conflict of Interests

The authors declare that there is no conflict of interests regarding the publication of this paper.

Acknowledgment

The research work is related to R&D Grant and Nr PBS2/A5/31/2013.

References

- [1] J. Carrey, B. Mehdaoui, and M. Respaud, "Simple models for dynamic hysteresis loop calculations of magnetic single-domain nanoparticles: application to magnetic hyperthermia optimization," *Journal of Applied Physics*, vol. 109, Article ID 083921, 2011.
- [2] G. Vallejo-Fernandez, O. Whear, A. G. Roca et al., "Mechanisms of hyperthermia in magnetic nanoparticles," *Journal of Physics D: Applied Physics*, vol. 46, no. 31, Article ID 312001, 2013.
- [3] H. Nemala, J. S. Thakur, V. M. Naik, P. P. Vaishnav, G. Lawes, and R. Naik, "Investigation of magnetic properties of Fe_3O_4 nanoparticles using temperature dependent magnetic hyperthermia in ferrofluids," *Journal of Applied Physics*, vol. 116, no. 3, Article ID 034309, 2014.

- [4] P. Di Barba, F. Dughiero, and E. Sieni, "Magnetic field synthesis in the design of inductors for magnetic fluid hyperthermia," *IEEE Transactions on Magnetics*, vol. 46, no. 8, pp. 2931–2934, 2010.
- [5] R. E. Rosensweig, "Heating magnetic fluid with alternating magnetic field," *Journal of Magnetism and Magnetic Materials*, vol. 252, no. 1–3, pp. 370–374, 2002.
- [6] A. Miaskowski, B. Sawicki, and A. Krawczyk, "The use of magnetic nanoparticles in low frequency inductive hyperthermia," *COMPEL—The International Journal for Computation and Mathematics in Electrical and Electronic Engineering*, vol. 31, no. 3, pp. 1096–1104, 2012.
- [7] G. Zhou, W. Duan, and B. Gu, "First-principles study on morphology and mechanical properties of single-walled carbon nanotube," *Chemical Physics Letters*, vol. 333, no. 5, pp. 344–349, 2001.
- [8] E. S. Glazer and S. A. Curley, "Non-invasive radiofrequency ablation of malignancies mediated by quantum dots, gold nanoparticles and carbon nanotubes," *Therapeutic Delivery*, vol. 2, no. 10, pp. 1325–1330, 2011.
- [9] B. Zhang, M. A. J. Moser, E. M. Zhang, Y. Luo, H. Zhang, and W. Zhang, "Study of the relationship between the target tissue necrosis volume and the target tissue size in liver tumours using two-compartment finite element RFA modelling," *International Journal of Hyperthermia*, vol. 30, no. 8, pp. 593–602, 2014.
- [10] G. Zorbas and T. Samaras, "Simulation of radiofrequency ablation in real human anatomy," *International Journal of Hyperthermia*, vol. 30, no. 8, pp. 570–578, 2014.
- [11] L. Szymanski, *Electrothermal Synthesis of Carbon Nanotubes under Atmospheric Pressure*, Zeszyty Naukowe Nr 1162, Lodz University of Technology Press: Scientific Bulletin of the Lodz University of Technology, Lodz, Poland, 2013, (Polish).
- [12] K. Lipert, M. Ritschel, A. Leonhardt, Y. Krupskaya, B. Büchner, and R. Klingeler, "Magnetic properties of carbon nanotubes with and without catalyst," *Journal of Physics: Conference Series*, vol. 200, no. 7, Article ID 072061, 2010.
- [13] U. Weissker, S. Hampel, A. Leonhardt, and B. Büchner, "Carbon nanotubes filled with ferromagnetic materials," *Materials*, vol. 3, no. 8, pp. 4387–4427, 2010.
- [14] R. Burgess, *Understanding Nanomedicine: An Introductory Textbook*, Pan Stanford Pte, Singapore, 2012.
- [15] T. Atsumi, B. Jeyadevan, Y. Sato, and K. Tohji, "Heating efficiency of magnetite particles exposed to AC magnetic field," *Journal of Magnetism and Magnetic Materials*, vol. 310, no. 2, pp. 2841–2843, 2007.
- [16] B. Kozissnik, A. C. Bohorquez, J. Dobson, and C. Rinaldi, "Magnetic fluid hyperthermia: advances, challenges, and opportunity," *International Journal of Hyperthermia*, vol. 29, no. 8, pp. 706–714, 2013.
- [17] J. Hilding, E. A. Grulke, Z. G. Zhang, and F. Lockwood, "Dispersion of carbon nanotubes in liquids," *Journal of Dispersion Science and Technology*, vol. 24, no. 1, pp. 1–41, 2003.
- [18] A. Jorio and G. D. M. Dresselhaus, *Carbon Nanotubes. Advanced Topics in the Synthesis, Structure, Properties and Applications*, Springer, Berlin, Germany, 2008.
- [19] Q. Cheng, S. Debnath, E. Gregan, and H. J. Byrne, "Ultrasound-Assisted swnts dispersion: effects of sonication parameters and solvent properties," *Journal of Physical Chemistry C*, vol. 114, no. 19, pp. 8821–8827, 2010.
- [20] H. H. Pennes, "Analysis of tissue and arterial blood temperatures in the resting human forearm," *Journal of Applied Physiology*, vol. 85, no. 1, pp. 5–34, 1998.
- [21] 2015, <http://www.itis.ethz.ch/itis-for-health/virtual-population/overview/>.
- [22] P. A. Hasgall, F. Di Gennaro, C. Baumgartner et al., "IT'IS Database for thermal and electromagnetic parameters of biological tissues," Version 2.5, 2014, <http://www.itis.ethz.ch/database>.
- [23] S. A. Sapareto and W. C. Dewey, "Thermal dose determination in cancer therapy," *International Journal of Radiation Oncology, Biology, Physics*, vol. 10, no. 6, pp. 787–800, 1984.
- [24] I. A. Chang and U. D. Nguyen, "Thermal modeling of lesion growth with radiofrequency ablation devices," *BioMedical Engineering Online*, vol. 3, article 27, 2004.
- [25] S. A. Baldwin, A. Pelman, and J. L. Bert, "A heat transfer model of thermal balloon endometrial ablation," *Annals of Biomedical Engineering*, vol. 29, no. 11, pp. 1009–1018, 2001.
- [26] H. H. Pennes, "Analysis of tissue and arterial blood temperature in the resting human forearm," *Journal of Applied Physiology*, vol. 1, pp. 93–122, 1948.
- [27] M. J. Borelli, L. L. Thompson, C. A. Cain, and C. A. Dewey, "Time-temperature analysis of cell killing of BHK cells heated at temperatures in the range of 43.5°C to 57°C," *International Journal of Radiation Oncology, Biology, Physics*, vol. 19, pp. 389–399, 1990.
- [28] P. S. Yarmolenko, E. J. Moon, C. Landon et al., "Thresholds for thermal damage to normal tissues: an update," *International Journal of Hyperthermia*, vol. 27, no. 4, pp. 320–343, 2011.
- [29] S. J. Graham, L. Chen, M. Leitch et al., "Quantifying tissue damage due to focused ultrasound heating observed by MRI," *Magnetic Resonance in Medicine*, vol. 41, no. 2, pp. 321–328, 1999.
- [30] M. R. Hemmila, D. S. Foley, A. V. Casetti, O. S. Soldes, R. B. Hirschl, and R. H. Bartlett, "Perfusion induced hyperthermia for oncologic therapy with cardiac and cerebral protection," *ASAIO Journal*, vol. 48, no. 4, pp. 350–354, 2002.
- [31] O. Seror, M. Lepetit-Coiffé, B. Bail et al., "Real time monitoring of radiofrequency ablation based on MR thermometry and thermal dose in the pig liver in vivo," *European Radiology*, vol. 18, no. 2, pp. 408–416, 2008.
- [32] M. Lepetit-Coiffé, B. Quesson, O. Seror et al., "Real-time monitoring of radiofrequency ablation of rabbit liver by respiratory-gated quantitative temperature MRI," *Journal of Magnetic Resonance Imaging*, vol. 24, no. 1, pp. 152–159, 2006.
- [33] J. Haveman, O. A. G. Smals, and H. M. Rodermond, "Effects of hyperthermia on the rat bladder: a pre-clinical study on thermometry and functional damage after treatment," *International Journal of Hyperthermia*, vol. 19, no. 1, pp. 45–57, 2003.